UNIVERSITY OF PAVIA

DOCTORAL SCHOOL IN ELECTRONICS, COMPUTER SCIENCE
AND ELECTRICAL ENGINEERING

CYCLE XXIX
A.Y. 2013-2016

A Non-Invasive Radar Technique Based on Artificial Neural Network for Breast Cancer Detection

Doctoral Thesis of
Claudio Lenzi

Tutor: Full Professor Salvatore Caorsi

Table of Contents

1. Introduction

In the context of the broad field of applications related to non-invasive time-domain electromagnetic (EM) techniques for the detection of buried dielectric anomalies and based on the use of artificial neural networks (ANNs), the research activity described in the present Ph.D. thesis is primarily focused on the theme of breast cancer detection.

According to recent statistical reports provided by the American Cancer Society [1], the breast cancer is the most common typology of cancer among women. In this context, in order to improve the outcomes of the treatments and reduce the mortality rate, an accurate diagnosis of the tumor presence during its early stage of development represents one of the most important and challenging tasks [2].

At present, the standard technique used for the diagnosis of breast cancer is the X-ray mammogram. However, besides the health risks and difficulties that derive from the exposure to X-rays and the uncomfortable breast compressions, such a technique suffers from low and not stable values of sensitivity [3]. In order to improve the performance, the X-ray mammogram has been proposed in a combined way together with other diagnostic techniques, such as the magnetic resonance imaging (MRI), the ultrasound (US), and the simple clinical examination. However, clinical studies have found and highlighted that, despite the combined use of these diagnostic techniques can improve the value of sensitivity or specificity, the overall accuracy, that at the same time depends from both the values of sensitivity and specificity, varies inside the limited range of 66.6–75.6 % [4, 5].

Because of the above cited problems and limitations, the need of having a non-invasive technique for detecting early-stage breast cancers with high and reliable values of accuracy has encouraged several groups of research to investigate and develop new diagnostic techniques. In this context, an interesting alternative, that in the last decades received more and more interest from the scientific community, is represented by the microwave diagnostic techniques. These techniques are focused

to exploit the substantial contrast that exist between the electromagnetic properties of the healthy and malignant breast tissues at microwave frequencies. Moreover, several advantages can derive from the use of such a range of frequencies, besides the already mentioned non-ionizing nature. Others advantages derive from the fact that the required instrumentation is not expensive and, thanks to the high sensitivity of the microwave sensors, low power signals can be used. Finally, these approaches are non-invasive, do not involve painful tests, and do not require uncomfortable breast compressions.

Nowadays, several novel approaches and techniques are continually developed and proposed by different groups of research around the world. Between the main reasons that motivate such a search, a challenging task is related to reduce the long times and the high computational burden required by the complex algorithms of electromagnetic signals processing, but the more important aspect is to reach higher and more reliable values of specificity, sensitivity, and overall accuracy.

In this context, in this Ph.D. thesis, a new breast cancer radar detection technique—based on the ANN processing of suitable information extracted from the radar signals—is presented and assessed. The endpoint of the proposed approach is not the breast imaging, but to detect the presence, or absence, of a tumor independent of its depth and width. Moreover, since the use of ANNs allows the possibility of re-formulate the inverse scattering problem considering only the unknowns of interest, several advantages, such as low computational burden and short times of computation, are provided.

In the next sections, the present PhD thesis is composed as follows.

Chapter 2 presents both the main benign and malignant breast diseases—namely the calcifications, the fibroadenomas, the cyst, and the breast carcinoma—and the main and standard used diagnostic techniques—namely the breast biopsy, the X-ray mammogram, the MRI, and the US. At the end of this chapter, the standard statistical diagnostic parameters—consisting of the sensitivity, the specificity, the positive predictive value, the negative predictive value, and the overall accuracy—are in detail described, and the performance of the above diagnostic techniques are discussed in the cases where they are used both alone or in a combined way.

Chapter 3 is aimed to present a review of the microwave diagnostic techniques proposed in literature. In particular, this chapter in details describes the passive microwave imaging techniques and the active microwave imaging techniques consisting of the microwave tomography (MT) and the ultra-wide band (UWB) radar imaging.

In Chapter 4, the proposed ANN-based breast cancer radar detection technique is presented, designed, and assessed. In particular, the proposed technique is tested using both two-dimensional (2D) and three-dimensional (3D) realistic breast models derived from the UWCEM database [6]. Moreover, since the importance of suppressing the predominant reflections due to the presence of the skin [7, 8, 9, 10]—the so-called skin-artifact component—the proposed ANN-based breast cancer radar detection technique was tested using both an ideal cleaning technique and the realistic model-based skin-artifact removal technique presented in Appendix B.

A brief section devoted to the conclusions summarizes the principal key points of the present Ph.D. thesis and the results obtained putting into evidence the capabilities but also the limitations of the studied approach for the diagnosis of breast cancers.

For the sake of completeness in the following a very short description of the Appendixes is also given.

Appendix A presents and describes the main architectural elements and the operations that are need during the design of an artificial neural network. In particular, it describes the artificial neuron, the activation function, the principal ANN architectures, and both the training and test operations.

In Appendix B, a new model-based skin-artifact removal technique is presented and assessed. This technique is especially proposed for UWB radar methods that work on the radar signals backscattered from the breast. The purpose is to find practical implementation method in order to suppress the strong skin reflections with good effectiveness, without introduce significant radar signal distortions, and without assuming a-priori information on the actual geometric and dielectric structures of the breast.

Finally, remaining in the field of applications related to non-invasive time-domain electromagnetic detection techniques based on the use of artificial neural networks, Appendix C presents an assessment and optimization study of a new probing technique designed to detect and locate an EM source situated in an indoor environment.

2. The Female Breast Diseases and the Main Actual Diagnostic Techniques

2.1. Introduction

The breast is a female symmetrical organ located on the front surface of the chest. Typically, such a body is mainly composed of fibro-glandular tissue and adipose tissue (fat). The fibro-glandular tissue consists of 15-20 independent lobes where, at each of these corresponds a galactophore, namely a lactiferous duct, which drains the breast and opens at the nipple. The lobes are immersed in the adipose tissue and separated from each other by means of the connective fibrous tissues. All these components on the whole constitute the "mammary gland" that is externally covered by the skin and supported by the pectoral muscle.

The shape and the size of the breast can considerably vary in relation to age, race and individual characteristics. From the puberty, due to an expansion of the glandular component, the breast increases in volume. The size and shape of that body, is very variable and this is mainly due to the amount and disposition of the adipose tissue. The development of the glandular tissue occurs mainly as a result of stimulation of the female hormones, which can vary depending on the stage of the menstrual cycle and the age of the woman. Generally, the glandular component is present in larger amounts, compared to adipose tissue, in women of young age. Conversely, in post-menopause and with aging, the fatty tissue component tends to increase. This is the reason for which the mammography performed on young women, and more generally on women with dense breasts, is more difficult to interpret.

In the following of the chapter, first the main benign and malignant breast diseases are presented. Then, a second section will be focused on describing the main and most used diagnostic techniques, namely the X-ray mammogram, the magnetic resonance imaging (MRI), and the ultrasound (US).

At last, the performance of these technique will be discussed in the cases where they are used both alone and in a combining way.

2.2. The Main Benign and Malignant Breast Pathologies

2.2.1. Calcifications

The calcifications [11] consist of mineral deposits within the breast tissues. Usually they are not malignant and their presence, being highly correlated with aging, should not cause worries.

Calcifications can be diagnosed by the physician through breast palpation, or generally by means of a diagnostic technique. However, using as example the X-ray mammogram, ambiguity may arise because both the calcifications and the tumors appear in a very similar way as white spots, and this may increase doubts about the real nature of the disease.

Mainly there are two different typologies of calcifications, namely the macro-calcifications and the micro-calcifications. The macro-calcifications are mineral deposits rather wide. They are usually associated with internal changes caused by aging, old injuries or inflammation. Usually, these deposits are related to not cancerous conditions and are present in about half of women older than 50 years, and in about one tenth among women under the 50 [12]. An example of macro-calcifications are the fibroadenomas, and because the substantial differences compared to the tumors, it is easier to make a correct diagnosis. The micro-calcifications [12] are small specks of calcium that usually appear in groups. Since, using the X-ray mammogram, they appear with not well-defined margins and opacities similar on those of the tumors, their presence can conduct to incorrect diagnoses. In these cases, as it will be more clear in the following sections, to perform a biopsy is strongly recommended.

2.2.2. Fibroadenomas

The fibroadenoma [11] is a benign tumor that develops in the tissues of the mammary glands. This is the most frequent nodular, solid, and benign breast pathology that can occur with aging. Compared to the surrounding tissues, it appears as a circumscribed and mobile nodule that may have dimensions ranging from less than 1 cm to over 10 cm. In the latter case, it is named giant fibroadenoma. As mentioned in the previous section, the fibroadenomas are a type of calcification which belongs to the category of macro-calcifications.

Its diagnosis can be simply made by the physician through breast palpation, and can be confirmed by means of a common not-invasive and not-destructing diagnostic test.

2.2.3. Cysts

The cysts [11] can be simply bags of fluid, in which case are known as Simple Cysts, or partially solid, known as Complex Cysts. The first are benign, namely of not cancerous nature. Usually they have a soft texture, a well-defined shape, and a highly variable size, namely from a diameter of few millimeters up to 4-5 cm. As will be more clear in the following sections, even if the simple cysts are bags containing fluid, they have well-defined margins and can be correctly detected through an X-ray mammogram. In contrast, since the complex cysts also contain solid parts, in a mammographic image they are no longer characterized by well-defined edges and regular opacity. In this case, to avoid failure in false positive or false negative results, a biopsy is strongly recommended.

2.2.4. Carcinoma

There are two most common forms of carcinoma [13]: invasive and not-invasive. The invasive carcinomas are those on which the dissemination of cancer cells tend to extend outside the origin place towards the surrounding and adjacent healthy tissues. The not-invasive carcinomas are those in which the cancerous cells remain inside of the membranes and of the lobes of the lactiferous ducts [14].

According to [14], the most frequently typologies of breast carcinomas are the following reported:

- invasive ductal carcinoma: it is the most common type of breast cancer, representing about the 70-80% of the detected breast cancer cases, and forms in the cells of the lactiferous ducts;
- invasive lobular carcinoma: it represents about the 10% of breast cancer diagnosis, and develops in the cells of the breast lobes;
- ductal carcinoma in situ: it is a type of cancer that occurs inside the cells of the lactiferous ducts, but it does not extend to other parts of the breast tissues;
- lobular carcinoma in situ: usually it does not represent a type of cancer, even if there are high possibilities that it develops in cancer. It consists of alterations in the cells that constitute the lobes of the breast.

2.3. The Main Actual Diagnostic Technique

2.3.1. Breast Biopsy

Once a suspicious area has been found inside the breast tissues, the only way to say with certainty whether it is a malignant cancer or not, is to implement a biopsy [12]. The discovery of the existence of such an area may has been made by using any physical examination, such as the X-ray mammography or other diagnostic tests that will be below described. During the biopsy [15] a small sample of cells or suspect body tissues are removed. Then, the extracted sample is sent to a pathology laboratory where it is processed and analyzed with a microscope.

In modern medicine, the biopsy plays a primary role for the treatment of many diseases. Besides providing the diagnosis, it can provide prognostic information on the predictable course of the disease and guide the clinician, and in particular the surgeon, in the choice of the therapy to be applied to the patient.

There are several types of biopsy and it is duty of a doctor advising the patient of the most appropriate method. However, the economic cost of these interventions is generally high. Therefore, it would be desirable trying to use a not invasive technique, in order to select the cases that mostly require the biopsy and to minimize the number of test with negative result.

2.3.2. X-ray Mammogram

The X-ray mammogram [12], based on the use of ionizing X-ray radiations, aims to detect and assess any change in the internal breast tissues. It is used as a diagnostic tool in order to identify and classify tumors, cysts, and calcifications. Because these anomalies can appear in a very similar way within a mammographic image, namely as white points or masses, it is very important, for a correct identification, a careful viewing by the radiologist and, if necessary, a biopsy is required. Looking at an X-ray mammogram, the most common sign of a breast disease is a nodular opacity which can be round, oval, lobulated, or irregular. The margins of the opacity define its benign or malignant nature. Usually, opacities with regular margins identify benign anomalies such as calcifications and cysts, whereas, those with irregular margins are malignant. Indeed, the most representative signs of breast tumors are opaque formations with irregular or frayed edges. As example, the cases of both a benign and malignant breast pathology are represented in Figure 2.1. In particular Figure 2.1(a) shows the X-ray mammogram measured on a breast containing a benign mass, and Figure 2.1(b) shows the case where a malignant tumor is present.

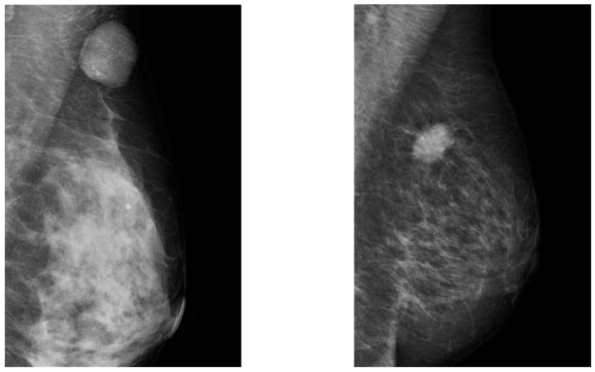

Figure 2.1. The X-ray mammogram. (a) Example of a digital mammogram image measured on a breast containing a benign pathology, it is worth noting the regularity of the margins. (b) A digital mammogram image measured on a cancerous breast, the tumor presents irregular margins.

Nowadays, the X-ray mammogram is the most effective diagnostic method, and two different types of test are mainly used: the screening mammography (SM) and the diagnostic mammography (DM). The SM is an X-ray test usually performed in the case when the patient doesn't present critical symptoms. The objective is to detect a possible cancer during its early stage of development, namely when it is too small to be palpated by the doctor or the patient herself. The SM consists of two different 2D projections of both the breasts that are taken from two different angles. Since the goal is to detect and assess any significant change in the breast internal tissues, it is important that the exam should be consistently repeated by the patient with regular interval times. In the case on which the patient presents symptoms or the SM highlights symptomatic changes, it is better to perform a DM. This is an X-ray test for which, in addition to the images obtained with the screening mammography, multiple scans are made with the aim to carefully study the area of concern. Moreover, during a DM certain images are enlarged, or the display type is changed, trying to facilitate the assessment of the small areas of interest and to offer the possibility of a closer look. Finally, the diagnostic response suggests us if a biopsy exam is necessary in order to define the nature of the abnormal area, namely to know whether it is cancer or not. As said before, even if the mammography is the currently most effective method to detect tumors, frequently it is not able to accurately differentiate benign and malignant lesions. Therefore, the only definitive way to confirm the nature of a suspicious lesion, is to perform a biopsy.

During the X-ray mammogram, in order to prevent movement and create a thinnest tissue layer, the breast is compressed between two plates consisting of a plastic plate on the top and the X-ray plate on the bottom that are both attached to the machine. The compression allows to reduce the radiation exposure, the blur, and sharpen the image. Despite this operation can be uncomfortable and even painful for some women, it is necessary to obtain a good image.

During the examination, the dose of radiation on which the patient is subjected is less than 1 mSv [16]. Where, the sievert (Sv) is the unit of measure of the equivalent radiation dose in the International System, and it is a measure of both the effects and damages caused by the radiation on the organism. The equivalent dose has the same size of the absorbed dose, or energy for mass unity.

The entire procedure requires about 20 minutes. Depending on the type of used machine, there are two ways to store the images. With the *Screen-film units* the images are produced on a large sheet of film, whereas with the *Full-field digital mammography units* the data are captured in a digital format and the results are displayed on a computer screen. For the most of features it is possible to obtain the same level of accuracy by using both the formats. However, the digital mammography presents the important advantage that the original image can be enlarged and viewed in many different ways on the screen, and this can strongly help the work of the clinician operator. In any case, whether it be of images on film or digital, the important thing is that the screening must be read by competent people able to interpret the results. Usually this task is entrusted to the figure of the radiologist who is a doctor specialized on the diagnosis of internal diseases with the aid of images produced by means of X-rays, sound waves, magnetic fields or other imaging methods.

2.3.3. Magnetic Resonance Imaging

The magnetic resonance imaging (MRI) [17], also known as magnetic resonance tomography (MRT), is based on the physical phenomenon of nuclear magnetic resonance according which the nuclei of the examined elements, under the application of a magnetic field, absorb and emit electromagnetic radiation. Differently from the X-ray mammogram, the MRI is generally considered not harmful for the patient because the latter is not subjected to ionizing radiation. The information given by the MRI allow us to make discrimination between different tissues on the base of their biochemical composition. Moreover, even if this doesn't mean having the three-dimensionality, it is able to providing different body sections on three different planes, namely the axial, the coronal, and the sagittal.

The principle of operation is based on the fact that the patient is subjected to a strong static magnetic field. The intensity of the magnetic field can vary from tenths of Tesla (T), for small machines dedicated to the study of the joints, to 3 T for the machines currently used for diagnostic purposes. Some actual machines achieve magnetic fields of 7 T, while devices that operate to 8 and 9 T are under experimental trials [17].

As with mammography, even the MRI exam makes use of a special machine specially designed for the detection of breast tissues. This last is able to provide higher quality images than the equipment that is used for the MRI of other body parts. Nevertheless, not all the hospitals, or the imaging centers, have a dedicated tool for the MRI of the breast.

A commercial scanner is mainly formed by elements that create static magnetic fields, or fields varying in time and space, and coordinated by a complex electronic control system. The primary elements are the main magnet, the radiofrequency coils, the gradient coils, and other auxiliary coils. In particular, the main magnet has the function of creating a static, homogeneous, and of high intensity magnetic field with the aim to permit the polarization of the nuclei. It is the largest and most expensive component of the entire system. The radiofrequency coils generate the rotating magnetic field at the Larmor frequency. The gradient coils generate the magnetic fields which vary linearly in space and that are indispensable to the images generation. At last, the other auxiliary coils serve to compensate for any irregularity or for modifying the geometry of the main fields.

During the actual MRIs, the patient is lying prone on a platform with two cavities for the breasts and must remain still for the entire test duration, where the required time is about 30-45 minutes [12]. Usually, a contrast material named gadolinium is injected into the patient prior to the examination in order to help a clearest visualization of the internal breast tissues. The presence of prosthesis, vascular clips, pacemakers and other medical-surgical devices can, in many cases, prevent the execution or the correct reading of the test.

Normally, the obtained images have dimensions varying from 256 × 256 pixels to 1024 × 1024 pixels, with a depth of 16 bits/pixel. This involves an intrinsic spatial resolution rather low, where details of 1 mm are practically at the limit of visibility.

Nevertheless, the importance of the MRI is in the fact that it is able to discriminate between internal tissue that if studied with the X-rays they should have the same transparency. In fact, a fundamental characteristic of the MRI is the ability on varying the image contrast by simply modifying the sequence of machine excitation. As example, it is possible to highlight or suppress the signal due to the blood, or to obtain functional character information rather than simply morphological.

Summarizing, the main disadvantages of using the MRI are: high costs, long time required for image acquisition and the fact that the proper equipment is not available in all facilities.

Nevertheless, because the MRI doesn't involve the use of ionizing radiation, it is more indicated when there isn't particular need to have a very high spatial resolution. Furthermore, since the bones are white viewed by the X-rays, the MRI is more useful in the case of lesions located close to bony structures.

2.3.4. Ultrasound

The Ultrasound (US) [18] is another medical diagnostic method that doesn't use ionizing radiation. It is based on the physical principle of measuring the echoes that are reflected when ultra-sound waves are transmitted through the biological tissues. The US is an operator-dependent procedure, because it needs of special qualities of dexterity and observation, culture of the image, and clinical experience.

An ultrasound scanner mainly consists of three parts: a probe, an electronic system and a display system. The probe is used in order to radiate and measure the signals. The used signals are selected inside the ultrasound band of frequencies, and they are chosen taking into account that higher frequencies are able to providing a higher images resolution, but lower capacity of penetrating deep inside the biological tissues. The ultrasound waves are generated by using a piezo-ceramic, or piezo-electric, crystal that is inserted into the probe and maintained in direct contact with the patient's skin. Usually, a special gel is interposed between the probe and the skin with the aim to helping the ultrasound in penetrating the examined anatomical object. The electronic system is used in order to drive the transducer, generate the transmit pulse, receive the return echoes, and process the received signals. Finally, the display system is used to display the measured data via on-screen images.

The signals processing is focused on detecting the acoustic impedances of the different media. By varying the radiating aperture of the antenna, it is possible to change the depth up to which the beam can be considered as parallel, so that the incident wave can be considered as plane wave. In this way the acoustic impedance, that normally is a complex quantity, is real.

The acoustic impedance, denoted by Z, is given by the ratio between the sound pressure and the vibration speed of the particles at one point. It is a characteristic property of the propagation medium. In the case of a plane wave the impedance is purely resistive and computable by means of the following Equation 2.1.

$$Z = \rho v \tag{2.1}$$

Where "ρ" is the medium density, and "v" is the speed of propagation of the wave inside the medium. The measuring unit of the acoustic impedance is the rayl.

The acoustic propagation in a medium depends on the impedance of the latter, namely the resistance offered by the material to the passage of the sound. This translates into a progressive attenuation of the beam due to the loss of energy. Furthermore, when an acoustic wave encounters an interface between two different media of different acoustic impedance, a part of the wave is transmitted, and part is reflected on the interface. The notion of acoustic impedance allows us to study qualitatively and quantitatively the phenomenon, and estimate the amount of acoustic energy transmitted and reflected. The reflected signal percentage contains information on the difference of impedance between the two medium, and it can be estimated through the Equation 2.2.

$$R = \frac{\left(Z_1 - Z_2\right)^2}{\left(Z_1 + Z_2\right)^2} \tag{2.2}$$

Where, R is the reflected signal percentage, Z_1 and Z_2 are respectively the acoustic impedances of the first and the second medium.

The time taken by the wave during both the forward and return path, and the depth from which the echo arrives are computed by the electronic system. The found point is related to an interface between two different media. By looking Equation 2.2, since the bones are characterized by an acoustic impedance much greater than the human tissues, it is evident that an US exam can't detect human tissues that located behind the bones. Moreover, both the air and gas zones, that are characterized by smaller values of acoustic impedance, are classified as shadow zones.

In conclusion, the advantages in favor of an US exam may be: the fact that it doesn't use ionizing radiation, low times of computation and test execution, low costs, and ultimately the usefulness that results in the fact of being able to be used to perform ultrasound-guided biopsies. In fact, the US may also be useful in helping a doctor to guide the needle during a biopsy. The main disadvantage is that it is a highly operator-dependent technique.

2.4. Performance of the Diagnostic Techniques

2.4.1. Standard Statistical Diagnostic Parameters

Usually, in the medical field, the performance of the diagnostic techniques is evaluated by using some statistical diagnostic parameters. The most common and popular error indexes, representing the standard used statistical parameters, are the sensitivity, the specificity, and the overall accuracy. Generalizing, these terms represent a statistical measure of the performance of a binary classification test. Other parameters, that not always are declared in medical fields but that are important for describing the performance of a binary test, are the positive predictive value (PPV) and the negative predictive value (NPV). In the following of the present section, all the above statistical parameters are in detail described.

The sensitivity, also known as true positive rate, is a parameter related to the ability of the diagnostic technique in correctly detecting the actual positive exams. As reported in Equation 2.3, it is defined as the proportion of sick patients for whom the test correctly detects the disease, namely the number of true-positive results, with respect to the total number of sick patients, namely the entire amount of both the true-positive and false-negative results. In other words, it is the probability that, given an actually sick patient, the test produces a positive outcome.

$$sensitivity = \frac{TP}{TP + FN} \tag{2.3}$$

Where the terms on the right represent: the true-positive (TP) results, namely the number of actually sick patients that are correctly diagnosed as sick; the false-negative (FN) results, namely the number of actually sick patients that are incorrectly diagnosed as healthy.

Sometimes, in the medical field, some reports refer, instead of the sensitivity, to the false negative rate. Where this last represents a parameter of accuracy for the patient side and, as reported in Equation 2.4, it is closely related to the sensitivity representing its complementary value.

$$false\,negative\,rate = \left(1 - sensitivity\right) = \frac{FN}{TP + FN} \tag{2.4}$$

As higher as possible is the sensitivity value, and as more as possible the diagnostic technique can be considered reliable in correctly detecting patients that are really sick. However, this parameter cannot be used alone; in fact, by considering a diagnostic exam that for some reasons produces only positive results, this test

theoretically presents a sensitivity of 100%, when this high value is derived only by the fact that the test does not produce negative outcomes. For this reason, the sensitivity must be always considered together with the specificity.

The specificity, also named as true negative rate, is a parameter related to the ability of the diagnostic exam in correctly identifying the negative test results. As defined in Equation 2.5, it is defined as the proportion of healthy patients for whom the test has not detected the disease, namely the number of true-negative results, respect to the total number of healthy patients, namely the entire amount of both the true-negative and false-positive results. In conclusion, it is the probability that, in presence of an actually healthy patient, or evenly a not-sick patient, the exam produces a negative outcome.

$$specificity = \frac{TN}{TN + FP} \tag{2.5}$$

Where the right terms are: the true-negative (TN) results, namely the number of actually healthy patients that are correctly diagnosed as healthy; the false-positive (FP) results, namely the number of actually healthy patients that are incorrectly diagnosed as sick.

Even in this case, if we consider a test that for some reasons provides only negative results, due only to the fact that there are not positive cases, it should present a specificity value of 100%. Therefore, if lonely considered, also this parameter is meaningless and it must be always evaluated together with the sensitivity.

Also for the specificity, some reports refer to the false negative rate. As reported in Equation 2.6, this term represents a parameter of accuracy for the patient side that is closely related to the specificity.

$$false\ positive\ rate = \left(1 - specificity\right) = \frac{FP}{TN + FP} \tag{2.6}$$

Another error index whose meaning is different from that of the sensitivity, but which can easily be confused with it, is the positive predictive value (PPV). As described by Equation 2.7, the PPV is defined as the ratio between the number of true-positive results and the total number of both the true-positive and false-positive results. The main difference with respect to the sensitivity is due to the fact that: while the latter represents an accuracy parameter for the patient, namely the number of true-positive results with respect to the total number of actually sick patients, the PPV is an accuracy parameter for the instrument itself that performs the test, namely the number of true-positive results with respect to the total number of patients that are diagnosed as sick from the test.

$$PPV = \frac{TP}{TP + FP} \tag{2.7}$$

Differently, as reported in Equation 2.8, the negative predictive value (NPV) is defined as the ratio between the number of true-negative results and the total number of cases diagnosed by the exam as negative, namely both the true-negative and false-negative results. The main difference with respect to the specificity is due to the fact that: while the specificity represents a parameter of accuracy for the user, namely the number of true-negative results compared to the total number of actual healthy patients, the NPV is a parameter of accuracy for the tool that performs the test, corresponding to number of true-negative diagnoses than the total number of patients that are correctly or wrongly diagnosed as healthy by the test.

$$NPV = \frac{TN}{TN + FN} \tag{2.8}$$

At last, in addition to the parameters above discussed, generally also the overall accuracy, or simply accuracy, of the diagnostic technique is computed. As defined in Equation 2.9, this parameter is defined as the ratio between the total number of cases that are correctly detected and classified by the diagnostic exam, namely the number of both the true-positive and true-negative results, and the total number of analyzed cases.

$$accuracy = \frac{TP + TN}{TP + TN + FP + FN} \tag{2.9}$$

2.4.2. Clinical Studies and Values of the Standard Statistical Diagnostic Parameters

At present, the X-ray mammogram is the standard diagnostic technique for breast cancer detection. One of the major reasons is related to its high resolution, reaching order values of the fractions of millimeter [19]. However, this technique suffers of various problems and limitations. First, since it exposes the patient to ionizing radiations, it is well known that it subjects the women to serious health risks and can increase the chances of cancer development [20]. In addition, due to the uncomfortable breast compression, it can be painful for the patient.

Another important problem regarding the X-ray mammogram is related to the wide variability of the number of detection failures, namely the false negative detections.

In fact, as reported in [3], the X-ray mammogram shows sensitivity values that vary in the range of 66% and 96%. This wide variability can be attributed to several factors [3]: such as the technical quality of the acquisition instrumentation, the latitude and the display contrast of the image, the skills and the experience of the radiologist that interprets the images, the breast compression, the size and the density of analyzed breasts, and the type of cancer that is present. Differently the values of specificity are more reliable, varying in the range from 88% to 99% [21].

An alternative technique for breast cancer detection is the MRI. It offers higher values of sensitivity, reaching the 94% [5, 22]. On the other hand, the MRI is an expensive exam and not all the hospitals have the suitable instrumentation. Moreover, it suffers of low values of specificity, varying between the 26% and 37% [5, 22], and this can lead to over diagnosis. These results make that the MRI is not currently used for detecting breast cancer, with except for the cases of high risk [23, 24]. Moreover, in [22] was found that some lesions, not detected with X-ray mammogram, were instead diagnosed by the MRI. These anomalies had a diameter size varying between 3 and 12 mm. For these reasons, in [22] it is concluded that the MRI can be used in the case of radiographically dense breasts, or that received silicone implants or extractions of nodules.

Also the performance of the US techniques was studied in literature. In [4] was found that it offers a false negative rate of 17%, corresponding to a sensitivity of 83%. Another study was made in [25] by considering the situations of palpable masses inside of radiographically dense breasts. In this cases, using as example an X-ray mammogram, both the benign and malignant masses can be partially or completely obscured, and thus not visible. Several examples of such a situation have been examined with the US technique achieving a false negative rate of value 25% [25]. Other studies have been done by taking under consideration both breasts with palpable and breasts with not-palpable lesions. The results have reported false negative results rather high, varying in the range between 0.3% and 47% [25, 26, 27, 28, 29], where the higher values are due to cases of not-palpable tumors. At, last, it has been experienced that the US presents an important skill in determining the form of internal mass, achieving an accuracy of 96% in the diagnosis of cysts [30].

In order to improve performance, various modalities of four different diagnostic techniques, consisting of the X-ray mammogram, the MRI, the US, and the clinical examination, were assessed in [4, 5]. During these studies, 258 female patients have been involved, namely 177 patient having a malignant tumor, and 81 healthy patients. The obtained results are illustrated in Table 2.1.

Looking at the table, it is evident that in the case where the X-ray mammogram, the MRI, and the clinical examination are together used, a sensitivity of 99.4% can be

reached. On the other hand, using this combination, the corresponding value of specificity is very low, and equal to 7%. The opposite case is when the clinical examination is alone applied, achieving values of sensitivity and specificity respectively equal to 50.3% and 92%.

Concluding, looking at the table, it appears immediately evident that, using different combination modalities of different diagnostic techniques, the single values of both the sensitivity and specificity can be varied and improved. However, the values of the overall accuracy, which accounts for the values of the sensitivity and specificity together, vary in a range between the 63.6%, corresponding to the case where the clinical examination is alone applied, and 75.6%, in the case where the X-ray mammogram and the clinical examination are together used.

Table 2.1. Performance obtained using various combination modalities of different diagnostic techniques.

Diagnostic Techniques	**Performance Statistical Parameters**			
	Sensitivity (%)	***Specificity (%)***	***PPV (%)***	***Accuracy (%)***
X-ray mammogram, clinical examination, MRI	99.4	7.0	70.1	70.5
MRI	94.4	26.0	73.6	72.9
X-ray mammogram, clinical examination, US	93.2	22.0	72.4	70.9
X-ray mammogram, US	91.5	23.0	72.3	70.2
US	83.0	34.0	73.5	67.8
X-ray mammogram, clinical examination	77.4	72.0	58.6	75.6
X-ray mammogram	67.8	75.0	85.7	70.2
Clinical examination	50.3	92.0	94.0	63.6

3. The Microwave Diagnostic Techniques

3.1. Introduction

The interaction between the electromagnetic (EM) waves and the matter, such as the healthy or malignant human tissues, depends on the dielectric properties of the material itself, and these properties are directly related with the amount of the water content. Because the healthy breast is mainly formed by adipose and fibro-glandular tissues, it can be classified as an organ of low water content. Differently the tumors, due to the greater vascularization of both the internal and surrounding areas, contain a higher amount of blood and they can be classified as tissues of high water content. This leads to an increment of both the values of conductivity and relative dielectric permittivity, in contrast than those of the surrounding normal healthy tissues.

Several studies and experiments have shown a remarkable diversity in the dielectric properties at microwave frequencies between the normal healthy breast tissues and the malignant tissues [31, 32, 33]. In recent decades, the existing contrast between the electromagnetic properties of malignant and healthy breast tissues has driven the development of microwave imaging techniques. Nevertheless, the dielectric properties of the healthy breast tissues can be highly different from patient to patient. In fact, the contrast between these properties and those related to tumors can vary in a range between 10% and 400% [34].

Nowadays, the microwave diagnostic techniques represent a promising alternative method for the detection of breast cancers. Among these, different modalities have been studied and proposed in literature, where they can be subdivided into two main topologies: consisting of the passive [35, 36] and the active approaches [31, 37, 38, 39, 40, 41, 42]. Using the passive systems, the energy radiated from the scenario is directly detected without using any external excitation, then the variations on the material properties inside the investigation domain are mapped through suitable elaboration of the collected signals. Differently, with the active approaches, the

domain of investigation is illuminated by using signals at microwave frequencies, then the backscattered signals are recorded and processed in order to obtain a "map" of the dielectric variations inside such a domain. Among the active techniques, the most in alternatives are those based on microwave tomography (MT), those based on ultra-wide band (UWB) radar imaging, and hybrid modalities.

Some hybrid modalities [43], are based on both the radar methodology, that is initially used to identify the spatial location of dielectric variations, and the microwave tomography, that is used to determine, through the formation of images, the shape and the nature of the materials within the scenario of interest. Differently, others hybrid techniques [44] exploit the physical phenomena on which, when a pulsed microwave signal is used in order to illuminate the domain of investigation, the absorbed microwave energy causes the radiation of acoustic waves. These last are detected by using an ultrasound transducer and the collected signals are processed with the aim to identify the presence and location of tumors.

In the following sections, this chapter will describe in more detail the passive systems, and the active systems based on both the microwave tomography and UWB radar imaging.

3.2. Passive Microwave Imaging Techniques

3.2.1. Method and Measured Physical Parameters

The passive microwave imaging techniques are also known with the name of microwave radiometry systems. According with the law of Planck, they are based on the measurement of EM fields that are spontaneously radiated from the bodies in function of their temperature. Since a heat increment is often related to the presence of tumors, the temperature can be used as a parameter to detect the existence of malignant lesions. In fact, because the cancer cells present a higher metabolism and a considerable blood perfusion, this fact may cause a temperature increment, in a range of 1 to 3 Celsius degrees, with respect to the surrounding tissues [45].

Bodies at elevated temperatures emit radiation at all frequencies with a peak in the infrared region. In the microwave region the radiation is minor, however in biological tissues the infrared radiation suffers of a reduced depth of transmission with respect to microwave frequencies, respectively of the order of millimeters compared to that of centimeters. It is for this reason that, since the 1970, the microwave radiometry has been proposed as a diagnostic technique for the detection of tumors [45].

3.2.2. Acquisition Systems

The emitted thermal noise power is connected to the spatial distribution of temperatures of the internal breast tissues. The measure of such a power is obtained by using a receiving system, named radiometer, which measures the emitted radiation [5, 46]. This instrument can be placed directly in contact with the breast or closer to it. However, in many cases it is preferable to place the sensor in contact in order to both improve the sensitivity and reduce the uncoupling caused by the layer of air that is present between the antenna and the breast.

One of the main problems, regarding the microwave radiometry, is related to the low sensitivity of the sensor, that it should be able to detect the small powers of the signals radiated by the tumor cells. A possible solution could be to use a cooling system with the aim of reducing the temperature of the microwave sensor [47], or implementing an ad hoc designed receiving system. For example, in the recent study [48], an active antenna, that is directly integrated with low-noise amplifiers (LNAs), has have been specifically tested to be used in the microwave radiometry.

Another problem is related to estimating the spatial distribution of the temperature of the internal breast tissues. In fact, for example, a cold target located close to the skin can produce the same radiated signal of another hot target that is located deep inside the breast. This problem can be solved by using a microwave radiometer able to measuring signals at different frequencies as proposed in [49] where also the size of the heat sources have been estimated.

Due to the nature of the signals that are measured with the microwave radiometry systems, different measurement errors can be attributed both to external EM interferents, such as wireless devices, and to internal EM interferents, caused by the radiometer itself. On one hand, the effects of the external interferents can be reduced through suitable filtering or shielding devices, on the other hand, the systematic errors related to the radiometer can be easily eliminated by carefully calibrating the measurement system.

3.2.3. Performance of Microwave Radiometry

In the literature, different studies have been made with the aim to assess the performance of the microwave radiometry systems. In [50], a clinical study was performed on the breasts of 129 patients. For each case, different measurements were performed in 20 different positions around the breast and, for each of these, the sensor was held stationary for 15 seconds before moving to the next position. The results have highlighted that, using the microwave radiometry, tumors can be detected with a sensitivity of 90% and a specificity of 59%.

In [51], another clinical trial was performed on 5 different patients having a malignant breast cancer. In order to compare different results, the measurements were made by using two different radiometers operating in two different bands of frequency. The first was designed to operate in the range of frequencies from 1.5 to 2 GHz, and the second in the range between 2.75 and 3.25 GHz. The characteristics of the two radiometers used in this experiment suggest us that: the first, because it works at lower frequencies, should be more adept on finding deeper lesions; while the second, working at higher frequencies, should be better able on detecting smaller tumors. However, the results showed that: in the case of four patients, having tumors positioned at depths lower than 0.3 cm, both the radiometers have correctly detected the tumor presence; instead, in the remaining patient, having a lesion at a depth greater than 0.3 cm, none of the two instruments has correctly detected the tumor presence.

The passive microwave techniques present some important advantages. First, during the diagnostic exam neither the patient nor the medical technicians are exposed to any electromagnetic radiation. Moreover, these methods can be used to detect tumors even inside the male breasts, which could not be done with the X-ray mammogram.

The main drawbacks linked are related to the fact that, anomalies located too deep inside the breast tissue are difficult to detect. In fact, the thermal radiation that comes from the malignant tissues is attenuated by the passage through the different layers of each healthy tissue, furthermore it is reflected and refracted at the various interfaces between the different tissues. So that, a crucial limit for the microwave radiometry is the extremely low power level of the thermal noise signal emitted by materials with losses, equal to about 10–15 Watt [52]. These results suggest us that the microwave radiometry systems could not be indicated to be used in the case of tumors located deep inside the breast tissues, or over a certain threshold of depth. At last, there is the risk of confusing the colder areas located close the outer surface, with the hot zones situated deeper inside the breast tissues.

3.3. Active Microwave Imaging Techniques

3.3.1. UWB Radar Imaging

As it is guessed from the name, the UWB radar imaging techniques use very short microwave signals—the so-called UWB microwave pulses—in order to illuminate the scenario contained inside the domain of investigation. Then the image is re-constructed through suitable software processing of the measures of the received radar signals.

These last are also known with the name of backscattered radar signals, because they are consequence of the electromagnetic scattering produced by the objects that are inside the domain of investigation.

3.3.1.1. Acquisition Systems

In a UWB radar imaging system, two different configurations of transmitting and receiving antennas, consisting of the multi-static [53] and the mono-static [42] radar approaches, can be used during both the operations of illumination and measurement. The multi-static radar configuration consists of using an antenna array of N elements. Each element, one at a time, radiates the incident pulse and the backscattered signals are recorded at the same time by all the—(N) or (N-1)—elements. In contrast, in the mono-static configuration, one at a time each single element of the antenna array radiates the UWB pulse and then measures the backscattered radar signal. In other words, it is equivalent to use only one single antenna, for both the operations of illumination and measurement, repeating the process for a fixed number of different space locations.

The measures of the backscattered fields may be obtained either through experimental way, by making measurements with actual prototypes of antenna systems, both through numerical way, using suitable software programs that simulate the electromagnetic wave propagation.

The first studies of experimental systems for UWB radar imaging, conducted on human tests, were developed at the University of Bristol, UK [39, 40, 54]. In particular, different prototypes of antenna arrays, characterized by a different number of elements—16 elements in [39], 31 in [54], and 60 in [40]—distributed over a hemispherical surface, were proposed. The patient is supposed to be laying on the prone position, the antenna array is positioned in contact with the breast, and the measures are collected using a multi-static radar system configuration. The experimental system operates in the frequency range of 4–8 GHz [40]. Others applications to human cases have been studied using the prototype system for UWB radar imaging developed at the University of Calgary, Canada [41]. In this experimental system, the patient is assumed to be laying on the prone position with the breast that extends inside a tank containing a coupling liquid and the sensor system. This last consists of both an UWB antenna and a laser. Both these two elements are attached to an arm used in order to move the sensor, and the measures are obtained according to the mono-static radar system configuration. The UWB antenna operates over the range frequencies between 0.5 GHz and 15 GHz. The measures of the backscattered signals are suitable processed in order to produce 3D images, whereas the laser data are used to better define the volume of interest with the aim of suppressing the strong components reflected from the skin.

Even though studies with actual experimental systems are present, in the literature related to the UWB radar imaging techniques, it is easier to find proposals that are preliminarily assessed and tested using radar data measurements obtained through numerical simulation.

In this contest, the finite-difference time-domain (FDTD) method is one of the most common numerical modeling technique used to simulate the propagation of electromagnetic waves in biological tissues [55]. In order to acquire the measures of backscattered radar signals that properly refer to realistic situations, it is necessary to have numerical breast phantoms that accurately describe the geometries and the dielectric properties of both the malignant and healthy tissues. To this end, realistic 3D models of the healthy breast tissues were developed and made available at the numerical breast phantom repository of the University of Wisconsin cross-disciplinary electromagnetic laboratory (UWCEM) [6]. In this database, the anatomical structures and the tissues distribution of 9 different actual breasts were stored. The data have been obtained starting from 9 actual three-dimensional MRI images where, using the appropriate dielectric properties, each MRI voxel has been mapped in the corresponding voxel inside the FDTD model. The voxel's dimension is $(0.5 \times 0.5 \times 0.5)$ mm^3. The numerical breast phantoms are classified on the base of their radiographic density into four main classes: *mostly fatty* (2 models), *scattered fibro-glandular* (3 models), *heterogeneously dense* (3 models), and *very dense* (1 model). An example of a model which belongs to the scattered fibro-glandular class is reported in Figure 3.1. As showed in figure, each numerical model distinguishes eight different typologies of healthy breast tissue: the skin, three types of adipose tissue, a transitional tissue, and three different typologies of fibro-glandular tissue. All these tissues can be dielectrically characterized using both the Cole-Cole or the Debye model.

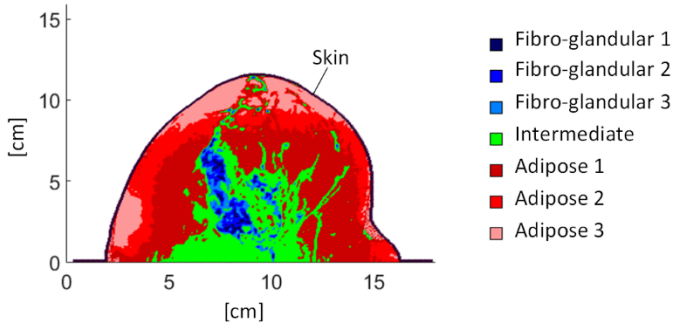

Figure 3.1. Sagittal section of a 3D realistic breast phantom provided Sagittal section of a 3D realistic breast phantom made available at the UWCEM database.

Since the UWCEM models are aimed to describe only the healthy breast tissues, a cancerous breast can be modeled by inserting a dielectric anomaly characterized by suitable values of the dielectric parameters. On the basis of experimental measures from cancer surgeries, the parameters for a Cole-Cole description of breast tumors were developed in [33]. The Debye parameters can be obtained from the Cole-Cole ones by minimizing the cost function proposed by [32].

3.3.1.2. Beamforming Algorithms

In the UWB radar imaging technique, the collected backscattered radar signals are processed using a time-domain image-formation algorithm—the so-called beamforming algorithm—in order to achieve a quantitative imaging of the breast that allows to determine the presence and location of the most significant dielectric scatterers. In this contest, several beamforming algorithms were proposed in literature, where they are differentiated in two different main categories: the data-dependent (DD) beamforming and the data-independent (DI) beamforming.

Between the most cited examples of DD algorithms there are the multi-static adaptive microwave imaging (MAMI) [56], the multi-input multi-output (MIMO) [57], and the time-reversal multiple signal classification (TR-MUSIC) [58, 59]. These techniques can reach high values of resolution in the case where the array steering vector—namely the set of phase delays of the wave when arrives to the different elements constituting the antenna array—is well known for the signal of interest. However, when dealing with realistic cases, it is difficult to accurately determine this component [7].

In order to overcome these drawbacks, some promising DI beamforming algorithms, that are free from the constraint of knowing the above information, were proposed in literature. Examples of the most studied and discussed DI algorithms are: the delay-and-sum (DAS) [31, 42, 55], the improved-delay-and-sum (IDAS) [60], and the delay-multiply-and-sum (DMAS) [61]. Usually these algorithms, in order to compensate the dependence of both the signal attenuations and dispersions from the propagation path inside dispersive tissues, use an assumed and homogeneous dielectric breast model. This model is used in order to approximating the times of arrivals of the signals with the aim of focusing the overall responses at specific locations. According to [55], the resulting accuracies are high in the case where homogeneous breast models are used, but they worsen where the heterogeneity of the internal tissues increases. In the following, the main DI beamforming algorithms are described in more detail.

3.3.1.2.1. Delay-and-Sum

The traditional DAS beamforming algorithm [31, 42, 55] is based on the use of the mono-static radar system configuration described in Section 3.3.1.1. According to such configuration, for each different radar position, the breast is illuminated with an UWB microwave pulse and the backscattered radar signal is measured by means of the same T_x/R_x antenna. The DAS algorithm implies that the backscattered radar signals, measured at different time instants, are added together creating the so-called synthetic focal points. In this way, if a tumor exists in a particular focal point, the contributions due to its presence are added up in a coherent way. In contrast, the contributions backscattered from the confused masses—consisting of changes in the type of the healthy tissues—are added up incoherently and, therefore, suppressed. Using the DAS approach, the energy is measured and stored at each synthetic focal point and, by varying the position of such fires within the breast tissues, a spatial profile is created, where to each focal point corresponds one pixel of the image.

Using N different radar antenna positions, it is possible to collect N different radar measures. Under this hypothesis, the energy associated with the focal point $\mathbf{r}$—which corresponds to the Cartesian coordinates $\mathbf{r} = (x, y, z)$—can be described according to Equation 3.1.

$$\begin{cases} E(\mathbf{r}) = \int_0^T \left[\sum_{n=1}^{N} w_n S_n\left(t - t_n(\mathbf{r})\right) \right]^2 dt \\ t_n(\mathbf{r}) = \dfrac{2\, d_n(\mathbf{r})}{v\, \Delta T} = \dfrac{2\, |\mathbf{r} - \mathbf{r}_n|}{v\, \Delta T} \end{cases} \tag{3.1}$$

Where: $E(\mathbf{r})$ is the energy associated with the focal point, T is the time window, S_n is the n^{th} backscattered radar signal, $t_n(\mathbf{r})$ is the n^{th} discrete time delay, $d_n(\mathbf{r})$ is the distance between the focal point ($\mathbf{r}$) and the n^{th} radar antenna position ($\mathbf{r}_n$), v is the average speed of propagation inside the breast tissues, ΔT is the interval of sampling, and w_n is a weight component introduced to compensate for the radial spread effect due to the cylindrical wave propagation of the incident UWB pulse. In [42] the weight component w_n was estimated as $(1/\, d_n(\mathbf{r}))$.

An example of multi-static configuration of the delay-and-sum algorithm (M-DAS) was developed by [62]. It is easy to understand that, using a multi-static system consisting of N elements it is possible to record N^2 different signals, where the higher number of recorded channels should provide more information on the target. However, in [62] only (N(N-1)/2) channels have been considered. In fact, because the reciprocity, not all the measured traces produce useful information for imaging the breast profile. Using the M-DAS, the energy associated to the pixels can be described as reported in Equation 3.2.

$$E(\mathbf{r}) = \int_0^T \left[\sum_{n=1}^{N(N-1)/2} w_n S_n \left(t - t_n(\mathbf{r}) \right) \right]^2 dt \tag{3.2}$$

Where: $E(\mathbf{r})$ is the energy, T the time window, S_n the n^{th} measured radar signal, $t_n(\mathbf{r})$ the n^{th} discrete time delay, $d_n(\mathbf{r})$ the n^{th} distance, and w_n the n^{th} weight component.

3.3.1.2.2. Improved-Delay-and-Sum

The IDAS beamforming algorithm [60] was developed to work on the radar signals measured using a multi-static radar system configuration. As mentioned in Section 3.3.1.1, using such configuration, one at time each element of the antenna array radiates the UWB pulse, and the backscattered signals are recorded by all the antennas at the same time. Substantially, the IDAS algorithm is an improvement of the traditional DAS in which an additional weighting factor—the so-called quality factor (QF)—has been introduced.

The QF is computed for each single focal point that is located inside the breast, and it represents a measure of the coherence between all the traces of the backscattered radar signals. First, for each focal point, the energy measured at different channels is summed and displayed together with the number of channels used. Then, the obtained curves of energy are normalized to the standard deviation of energy (σ_e) using the multiplication factor $[1 / (1 + \sigma_e)]$. At last, for each focal point, a polynomial of the second order ($y = ax^2 + bx + c$) is fitted to the normalized curve of energy. The obtained values of a are assumed to be the quality factor values.

Using the IDAS algorithm, in the case where an antenna array of N elements is used, the energy associated with the focal point $\mathbf{r}$—with Cartesian coordinates $\mathbf{r} = (x, y, z)$—is described using the following Equation 3.3.

$$\begin{cases} E(\mathbf{r}) = \mathrm{QF}(\mathbf{r}) \cdot \int_0^T \left[\sum_{n=1}^{N(N-1)/2} w_n S_n\left(t - t_n(\mathbf{r})\right) \right]^2 dt \\ t_n(\mathbf{r}) = \dfrac{2\, d_n(\mathbf{r})}{v\,\Delta T} = \dfrac{2\left|\mathbf{r} - \mathbf{r}_n\right|}{v\,\Delta T} \end{cases} \tag{3.3}$$

Where: $E(\mathbf{r})$ is the energy, $\mathrm{QF}(\mathbf{r})$ is the quality factor associated with the focal point $\mathbf{r}$, T is the time window, S_n is the n^{th} measured radar signal, w_n is the n^{th} weight component, $t_n(\mathbf{r})$ is the n^{th} discrete time delay, $d_n(\mathbf{r})$ is the n^{th} distance, v is the average speed of propagation inside the breast tissues, and ΔT is the interval of sampling.

3.3.1.2.3. Delay-Multiply-and-Sum

The DMAS beamforming algorithm [61] represents another variant of the traditional DAS algorithm, and it can be applied using both a mono-static or a multi-static radar system configuration. In the DMAS algorithm the recorded signals are time shifted according to the computed discrete time delays. Then, the shifted signals are in pairs multiplied before to be summed and squared in order to obtain the energy of the focal points. In conclusion, the DMAS algorithm is very similar to the DAS, but with the addition of the pairing multiplication procedure. Equation 3.4 describes the energy that is computed at the focal point with Cartesian coordinates $\mathbf{r} = (x, y, z)$.

$$E(\mathbf{r}) = \int_0^T \left[\sum_{n=1}^{(N-1)} \sum_{j=(n+1)}^{N} S_n\left(t - t_n(\mathbf{r})\right) S_j\left(t - t_j(\mathbf{r})\right) \right]^2 dt \tag{3.4}$$

Where: $E(\mathbf{r})$ is the energy, N is the number of the recorded channels, T is the time window, S_n is the n^{th} measured radar signal, $t_n(\mathbf{r})$ is the n^{th} discrete time delay, $d_n(\mathbf{r})$ is the n^{th} distance, v is the average speed of propagation inside the breast tissues, and ΔT is the interval of sampling.

3.3.1.2.4. Performance of Beamforming Algorithms

In order to assess the performance of the beamforming algorithms described in the previous paragraphs, namely the DAS, the M-DAS, the IDAS, and the DMAS, numerical simulations were performed in [55] using 3D realistic breast models taken

from the UWCEM database. In particular, in order to consider different distributions of internal tissues, three different 3D representations of the healthy breast were considered.

The first representation consists of a *homogeneous breast model* composed by only the skin and three typologies of adipose tissues. The second is modeled as *normal breast model* characterized by the presence of the skin, the adipose tissues, and only one typology of fibro-glandular tissue. At last, the third phantom consists of a *heterogeneous breast model* composed by the skin, three typologies of adipose tissues, and three typologies of fibro-glandular tissues.

Since the models taken from the UWCEM database aim to describe the dielectric properties of only the healthy breast tissues, in order to test the performance of the beamforming algorithms in detecting the presence of malignant lesions, different dielectric anomalies were inserted inside the breast models. In particular, tumors of three different dimensions—with global diameter values respectively equal to 5 mm, 10 mm, and 15 mm—were positioned in two different locations inside the considered healthy breast models.

All the healthy and malignant breast tissues were dielectrically characterized using the single pole Debye equation. The measures of the backscattered radar signals were obtained through numerical simulation using a software based on the finite-difference time-domain (FDTD) method. The used UWB signal consists of a differentiated Gaussian pulse of time duration 120 ps, and central frequency of 7.5 GHz.

In order to quantify the performance of the various beamforming algorithms, a suitable parameter—defined as the Signal to Mean Ratio (SMR)—was used. The SMR describes the ratio between the energy of the measured tumor response and the average energy due to all the responses of the healthy tissues contained inside the breast. Since the data of the backscattered radar signals are collected through numerical simulations, the denominator term can be simulated considering the breast model in absence of the anomaly. Instead, the contribution of the anomaly was obtained by performing the subtraction between the case of breast geometry with anomaly and the case of breast geometry without anomaly. In this contest, for each of the three models, for each of the six tumor's cases, and for each beamforming algorithm, the average SMR values have been computed.

Using the homogeneous breast model, the beamforming algorithms DMAS, IDAS, M-DAS, and DAS have provided average values of SMR respectively equal to 16.97 dB, 15.09 dB, 13.19 dB, and 10.12 dB. In this ideal case, the traditional DAS appears to be the weaker algorithm, whereas the DMAS seems to be the better one. However, in the case where the normal breast model is used, the performance of all the

beamforming algorithms are considerably reduced, showing for the DMAS, IDAS, M-DAS, and DAS, average values of SMR respectively equal to 13.39 dB, 8.84 dB, 10.22 dB, and 7.47 dB. These results show that the performance decrease with the introduction of the fibro-glandular region. In fact, in this situation the breast can no longer be considered as uniform, and the existing contrast with the propagation model assumed by the algorithms decreases the accuracy. At last, using the heterogeneous breast model, the average SMR values related to the DMAS, IDAS, M-DAS, and DAS, were respectively equal to -3.22 dB, -10.93 dB, 0.51 dB, and 3.14 dB. It worth noting that, where the SMR value is negative, it means that the average energy related to the healthy breast tissues is greater than the response due to the anomaly.

In conclusion, the results reported in [55] suggest that, between the algorithms studied, the DAS is the most robust beamforming algorithm. In fact, in the case where a more complex scenario is used in order to best characterize the realistic breast tissues, the traditional monostatic DAS is the algorithm that provides the best results.

3.3.2. Microwave Tomography

The microwave tomography (MT) techniques are focused at obtaining the actual distribution, namely the image, of the dielectric properties of the internal breast tissues. The aim is build the maps that describe the spatial distribution of the dielectric properties, consisting of the permittivity and the conductivity. Differently from the UWB radar imaging techniques, that are focused at providing a qualitative estimation of the breast with the aim to determine the presence and location of the main dielectric scatterers, the MT techniques are focused at providing a quantitative image of the breast in order to describe information regarding the nature, the shape, and the distribution of all the internal tissues.

The MT techniques are aimed at providing more informative images than the radar techniques, where the main advantage is related to the fact that a representation of this type can better identify a tumor compared to an image of the only main scatterers [63].

3.3.2.1. Acquisition Systems

In order to provide these highly informative images, the MT systems need to extract the as high as possible amount of information from the electromagnetic measurements of the breast, and it is for this reason that they mainly use antenna array measurement systems based on multi-static configurations [63].

The measures of the backscattered signals can be obtained in two alternative ways: through numerical simulations, using suitable software programs that simulate the electromagnetic wave propagation inside the biological tissues and suitable realistic breast phantoms, such as those provided by the UWCEM database previously described in Section 3.3.1.1; or through realistic experimental measurement systems. However, differently from the UWB radar imaging, in the bibliographical scenario relating the MT techniques it is easier to find studies on experimental systems applied in actual clinical trials or in laboratory experimental tests.

One of the first prototype system for MT, designed for in-vivo human tests, were developed by a research group at Dartmouth College, USA [64]. The patient is supposed to be laying on the prone position, with her breast that extends into a tank containing a matching fluid, consisting of a mixture of saline and glycerine. A circular antenna array, consisting of 16 T_x/R_x dipoles, is located inside the bath free to move at seven different distances between the chest and the nipple. The measures are collected using microwaves signals at different frequencies inside the range of 0.3–1.0 GHz. The obtained measurements are software processed in order to obtain a set of 2D images of the breast dielectric properties. A first in-vivo study has been conducted on 23 patients that not presented symptoms before the examination [65]. Another study was conducted on 150 patients, considering both cases of women presenting positive or negative mammograms [66], where, for tumors greater than 1 cm, significant results have been obtained. Moreover, an extension to 3D images, using measurements at higher frequencies up to 1.3 GHz, was reported in [34]. The overall results obtained with these MT systems show a significant coherence with the patient histories, and appreciable differences between the conductivity values of malignant and healthy tissues.

Moreover, a different MT system, that produces 2D images, was developed at the University of Keele, UK [67, 68, 69]. It uses a circular array of 24 T_x/R_x waveguides opened at the extremities and filled of ceramic material. The array is located into a bath of matching liquid and it operates in the frequency range of 1.0–2.3 GHz.

In the University of Manitoba, Canada [70, 71], a 2D MT system was designed using a circular array of Vivaldi antennas operating in the frequency band between 3 GHz and 6 GHz. This system has been tested without using any matching liquid.

Another 2D MT system, working in the frequency band between 0.5 GHz and 4.5 GHz, has been developed at the Chalmers University of Technology, Sweden [72]. This system uses a circular array of 20 monopoles located inside a metallic bath filled of coupling liquid.

At last, a 3D MT imaging system was developed by the Electromagnetic Engineering Research Team of Daejeon, Korea [63]. This system includes a hardware interface

for patients, that operates in the frequencies range of 0.5–3 GHz, and a 3D software for the image reconstruction. The hardware interface consists of a circular array antenna system composed by 16 T_x/R_x monopoles and placed in a tank filled with a coupling liquid.

3.3.2.2. Inverse Scattering Problem

Starting from the measures of the backscattered radar signals, the end point of the MT techniques is image the spatial distribution of the dielectric properties of all the internal breast tissues. In general, the reconstruction algorithm requires the solution of a problem of electromagnetic inverse scattering, consisting of a system of non-linear integral equations to be solved on a three-dimensional domain. Generally, to solve this problem is not trivial, because it is ill-posed and does not admit unique solution. Moreover, its solution can involve heavy computational burden and long computation times, where these two parameters strongly depend on the searched resolution accuracy, the frequencies of the microwave signals, the signal information that are extracted and processed, and the problem approximations that are applied.

The solution of the inverse scattering problem for microwave tomography has been widely studied in literature and different methods and approaches were proposed [73]. Between these, on one hand there are methods that make use of approximations in order to linearize the problem (the so-called methods of *linear microwave tomography*), whereas on the other hand there are methods that try to directly solve the non-linear problem (the so-called methods of *non-linear microwave tomography*).

Between the linear microwave tomography techniques, the use of the Born approximation [74] has been widely investigated. It consists of approximating the total field inside the target as the incident field, neglecting the effects of the internal scattering and diffractions. Since the total internal field is the sum of the incident field and the internal backscattered field, it is easy to understand that, the approximation is valid if the scattered field is much smaller than the incident field, where this is true if the target is a weak scatterer. For these reasons, the limitations on both the dielectric contrast and the maximum sizes of the object, in which the Born approximation can be assumed as valid, were studied in different works [75, 76]. Even if, the approaches based on approximations of linearization were successfully applied in order to image low-contrast objects, they suffer of limitations in the field of biomedical imaging, where the regions of interest are generally large and highly heterogeneous [73].

In contrast, the non-linear microwave tomography techniques are developed by re-formulating the problem as a minimization problem, in which a suitable cost function is minimized through an iterative process. Nowadays, the non-linear tomographic methods represent the approaches that were most studied, trying to optimize the cost functions, and to minimize both the number of unknowns and the computation times.

In order to transform the inverse problem in a minimization problem, first a reference volume, containing the breast and the T_x/R_x antennas, is chosen and used as reference domain. On the basis of the numerical solution of Maxwell's equations, using for example an FDTD method, the entire volume is spatially discretized into a number of variables characterized by the unknown dielectric properties. Using the same configuration of antennas, the correspondent direct problem is included, and its solution is performed in order to obtain an initial guess of the dielectric profile within the breast. Then, by using the data related to the actual breast and those obtained through simulation of the assumed breast, it is built a cost function based on the difference between these two sets of data. The obtained cost function is then minimized by means of iterative methods, by modifying the electrical properties of the various cells in which the domain was discretized. Assuming that, at the end of the optimization, the global minimum is reached, in this situation the simulated data are nearly equal, or even identical, to the actual reference data. The dielectric profile that corresponds to the obtained minimum situation, it is the searched result. Therefore, the image reconstruction process consists of a multidimensional ill-posed optimization problem, in which the number of the unknowns, of the order of thousands, mainly depends on: the physical size of the computational domain, the required spatial resolution, the dielectric properties of the geometry, and the frequencies used.

In literature, the proposed non-linear tomographic methods are classified in two different main categories: namely those based on *gradient-based local algorithms* and those based on *global algorithms*.

The methods based on gradient-based local algorithms, are aimed to search the solution only in a space closed around an initial distribution, where the cost function is iteratively linearized using its gradient. These approaches are also known with the name of Newton methods, where the most popular is the Gauss-Newton method [77, 78, 79]. Others algorithms are the conjugate gradient least squares (CGLS) algorithm [80] and the Landweber algorithm [81]. Moreover, an algorithm that was lately studied is the distorted born iterative method (DBIM) [82]. Since the size of the problem domain is moderate, the main advantage of the local techniques is that they offer lower computational burden. However, because the research of the solution is addressed by the direction of the gradient, the main disadvantage consists of the possibility to remain trapped in points of local minimum.

In contrast, to avoid of falling into local minimums, the methods based on global algorithm are aimed to search the solution inside the entire multidimensional space of solutions. The first methods proposed in literature were based on global optimization techniques such as the genetic algorithms (GA) [83, 84], differential evolution (DE) [85], and particle-swarm optimization (PSO) [86, 87] algorithms. These intelligent algorithms are aimed to mimic the behavior that is seen in nature in order to guide the research towards the optimal solution. However, these techniques can lead to a substantial increment of both the computational burden and the elaboration time. In order to simplify the problem and reduce the computational complexity, several methods were proposed in literature [88, 89, 90]. Moreover, a new intelligent search algorithm, consisting of the artificial bee colony (ABC) [91], has been recently studied for the solution of optimization problems. In order to compare the performance of the algorithms ABC, GA, DE, and PSO, numerical simulations were made in [92]. The reported results show that the ABC algorithm can provide a higher accuracy than the others. The improvements are related to the ability of reconstructing of the exact position of dielectric anomalies included within the breast geometry, and of computing the actual value of the dielectric properties.

4. Radar Detection Technique Based on Artificial Neural Network

4.1. Introduction

As mentioned in the previous sections, nowadays the standard technique for breast cancer diagnosis is the X-ray mammogram. However, besides the well known problems and limitations related to the painful breast compression and the exposure to X-rays, this technique suffers from low, and highly fluctuating, values of sensitivity, where these last can vary inside the range of 66% and 96% [3]. To improve the performance, different diagnostic techniques—consisting of the X-ray mammogram, MRI, US, and clinical examination—were clinically assessed using several combination modalities [4, 5]. The reported results shown that, even if the combined use of these techniques can singly improve the value of sensitivity or specificity, the overall accuracy, that involves in conjunction both the sensitivity and specificity values, is limited to the range 63.6–75.6 % [4, 5].

In the last decades, the need of having a non-invasive technique able of detecting early-stage breast cancer with high values of accuracy has encouraged and motivated the research of new diagnostic techniques. In this context, the contrast that exists between the dielectric properties of the malignant and healthy breast tissues at the microwave frequencies has driven the development of the microwave imaging techniques [31, 32, 33]. As discussed in Chapter 2, several methods were proposed and studied in literature where, among these, the active methods consisting of the microwave tomography (MT) techniques and UWB radar imaging techniques represent the two most interesting approaches.

The several advantages that can derive from the use of such a range of frequencies are enough to motivate the vast field of research that was developed in recent decades. One of the main reasons is related to the non-ionizing nature of the

frequencies used. A second advantage is due to the fact that the required instrumentation is not expensive. Moreover, thanks to the high sensitivity of the sensors that are available, signals of low power can be used. Finally, these approaches do not involve painful tests, because it is not required any compression or others uncomfortable placements of the breast.

Nevertheless, nowadays, several innovative approaches are continuously developed and proposed by several groups of research. Between the main points that motivate such a search, an important aspect is related on decreasing both the high computational burden and the long times required for processing the data contained in the backscattered radar signals. Another point is to obtain higher values of image's resolution, but what is more important is to reach more reliable and higher values of specificity, sensitivity, and overall accuracy of the global diagnostic technique.

In this context, in this Ph.D. thesis a new UWB radar detection technique, designed for the diagnosis of breast cancer, is presented and assessed. The proposed approach is based on the processing, through the use of artificial neural networks (ANNs), of suitable data extracted from the backscattered radar signals measured around the breast, and at different distances from the chest. The endpoint is not the breast imaging, but to detect the presence, or absence, of a tumor independent of its depth and width. Since the use of ANNs allows the opportunity of re-formulate the problem considering only the unknowns of interest, several advantages—such as short times of computation and low computational burden—are provided.

The proposed technique is tested and validated using both two-dimensional (2D) and three-dimensional (3D) realistic breast models derived from the UWCEM database [6], previously described in Section 3.3.1.1. Moreover, since the importance of suppressing the predominant component due to the presence of the skin [7, 8, 9, 10]—the so-called skin-artifact component—the ANN-based technique was assessed using both an ideal cleaning technique and a realistic model-based one (described in Appendix B).

In this chapter, first a detailed description of the method as a whole is presented. Then, a second section will present the results obtained—using realistic 2D breast models and an ideal skin-artifact removal technique—in both the cases of tumors located inside and outside the fibro-glandular tissues. In these first assessment analyses, the use of two different UWB pulses will be assessed. Because the goodness of the results obtained especially for tumors positioned outside the fibro-glandular tissues, a third section will be focused on this situation, where a broader scenario—consisting of a more generic and realistic set of testing data—will be considered. In this section, the performance will be assessed applying the realistic model-based cleaning technique described in Appendix B, moreover, some test will

be performed using a realistic 3D breast model. At last, a final section will present the improvements that are achieved in the case where the here proposed diagnostic criterion is applied.

4.2. The Method

4.2.1. Breast Geometries and Simulation System

The patient is assumed to be laying on the prone position. Using a mono-static radar system configuration, the measures of the backscattered signals are simulated in different space locations situated at different distances from the chest and along a circumference around axially the breast.

According to the described situation, in order to validate the performance of the proposed approach, a set of 2D realistic healthy and malignant breast geometries were considered. All the geometries were built starting from the 3D realistic breast models made available at the UWCEM database [6]. As mentioned in Section 3.3.1.1, in this database nine realistic breast phantoms, derived from actual 3D MRI images, are freely provides. Each models dielectrically characterizes eight different tissue typologies of the healthy breast: the skin, three different typologies of adipose tissue, a transitional tissue, and three types of fibro-glandular tissue.

In this context, starting from the UWCEM models, several 2D breast geometries were built taking into account different cross-sections. Each healthy tissue has been characterized using the Debye model and, in order to describe varied and several breasts, that are characterized by different densities, the values of the dielectric parameters—consisting of the static relative permittivity ε_s, the relative permittivity at infinite frequency ε_∞, the conductivity σ, and the relaxation time τ—were chosen in a random way within the range of admissible the values furnished by [6].

The healthy breast geometries were built choosing, in random manner, the UWCEM model, the cross-section, and the Debye parameters—ε_s, ε_∞, σ, and τ—used to dielectrically describe the internal healthy tissues. The cancerous geometries were obtained starting from new healthy geometries, built in the same random procedure, in which a dielectric anomaly—representing the tumor—was inserted. In order to describe a broader, significant, and generic scenario of cancerous geometries, different dielectric anomalies, characterized by different diameter dimensions, were positioned at different depth inside the healthy breast tissues.

The diameter was randomly chosen inside the range of 0.2-1.0 cm, whereas the depth was chosen, always in a random mode, between 0.5-cm depth from the outer skin

surface and the center of the reference system. Where the reference system corresponds to the center of the circumferences on which the mono-static radar system collects the measures of the backscattered signals.

As mentioned in Section 3.3.1.1, the Debye parameters for the tumor dielectric characterization was obtained from the Cole-Cole representation developed in [33] and minimizing the cost function proposed by [32]. In particular, the tumor has been characterized with an ε_s of 61.6, ε_∞ of 14.5, σ of 0.7 S/m, and a τ of 13 ps.

The measures of the backscattered radar signals were collected, for each different radar position, through numerical simulation using the finite-difference time-domain (FDTD)-based software GprMax [93]. As already proposed in literature by several authors [8, 10, 41, 42, 94], the used illuminating UWB signal is a differentiated Gaussian pulse (DGP). Compared to the simple Gaussian pulse, it was studied that the chosen waveform is able to produce a higher power of the backscattered signal, and for this reason it is more suitable to be used for the detection of deep targets that are sparsely distributed [95]. At last, the proposed approach has been assessed using two different DGP pulses: a DGP pulse of central frequency 6 GHz and time duration 0.3 ns; and a DGP of central frequency 2 GHz and duration 1 ns. The used UWB pulses are represented in Figure 4.1.

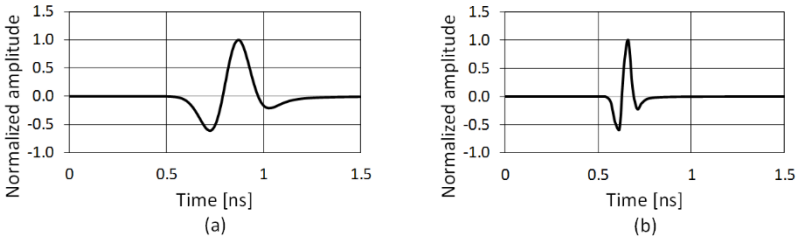

Figure 4.1. The illuminating UWB pulses: (a) DGP of central frequency 2 GHz and time duration 1 ns; (b) DGP of central frequency 6 GHz and 0.3-ns duration.

4.2.2. Radar Signals Pre-Processing

In order to apply the proposed signal processing technique that, being based on the use of artificial neural networks, needs to be trained on data as representative as possible of the presence of tumors in the breast, suitable data must be extracted from the measured traces of the backscattered radar signals. However, serious complications occur because the backscattered radar signals do not contain only the echoes reflected from the healthy and malignant internal breast tissues, but also those

generated from the presence of the skin, the so-called skin-artifact component. Since this last has a predominant nature with respect to the others, its presence represents a challenging problem and makes difficult the choice of suitable data to be extracted for best characterize the tumor's presence.

As examples for better explain the problem, Figures 4.2 and Figure 4.3 show the radar signals obtained before and after the application of a skin-artifact removal technique. In particular, Figure 4.2 show the case where the DGP at 2 GHz is used, and Figure 4.3 refers to the case of the DGP at 6 GHz. Moreover, Figures 4.2(a) and 4.3(a) show the total radar signals measured on the realistic cancerous geometry, and Figures 4.2(b) and 4.3(b) respectively report the same radar signals after the application of the skin-artifact removal technique.

The backscattered signals were measured on a 2D realistic cancerous breast geometry in which a dielectric anomaly, of 6-mm diameter, has been positioned at a depth of 1.5 cm from the outer surface of the skin. The applied skin-artifact removal technique consists of an ideal cleaning technique, where the ideally cleaned radar signal was obtained by subtracting, from the total one, the signal measured on a two-layered geometry—having the same shape and dimensions of the realistic cancerous breast geometry—characterized by the presence of only the skin and adipose tissue.

Comparing Figure 4.2(a) with Figure 4.2(b), and Figure 4.3(a) with Figure 4.3(b), it appears evident that the skin-artifact component is of different orders of magnitude higher than the other signal components. Moreover, since it overlaps the reflections due to the internal breast tissues, it masks also the contribution that contains the tumor signature. These considerations highlight that the application of a cleaning technique is strictly required in order to extract significant information from the backscattered radar signals.

At last, since the external shape of the realistic breast geometries is not strictly circular, the distance between the radar antenna and the outer skin surface is not constant. This involves that the arrival times and the amplitudes of the measured signals change at varying of the mono-static radar position. For these reasons, in order to reduce these space-temporal errors, an equalization on both the amplitudes and arrival times has been applied. Using a cross-correlation technique, the time of arrival of the backscattered radar signal is computed for each radar position, then for each of these, the resulting own value is used as zero reference time of the recorded signal. Moreover, the signal amplitudes are multiplied by a coefficient that takes into account of the temporal shift.

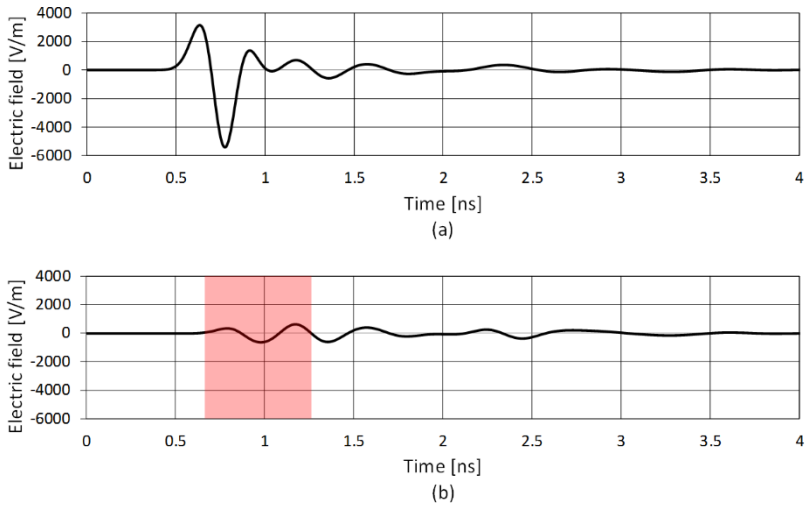

Figure 4.2. The backscattered radar traces obtained before and after the application of the ideal skin-artifact removal technique, and where the DGP of central frequency 2 GHz is used. (a) Total backscattered radar signals measured on the cancerous geometry. (b) Ideally cleaned radar signal, where the signal contribution of the tumor is marked in red.

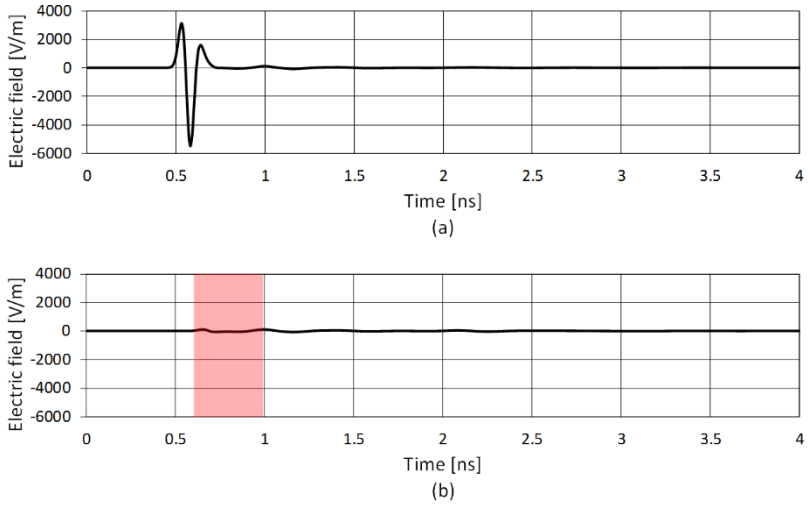

Figure 4.3. The backscattered radar traces obtained before and after the application of the ideal skin-artifact removal technique, and where the DGP of central frequency 2 GHz is used. (a) Total backscattered radar signals measured on the cancerous geometry. (b) Ideally cleaned radar signal, where the signal contribution of the tumor is marked in red.

4.2.3. ANN Radar Data Processing

Once obtained the cleaned-equalized radar signals described in the previous section, the idea is to exploit, as significant data in order to train and test the artificial neural network, the information contained in the amplitudes (A_1, … A_i, … A_N) and the times of arrival (t_1, … t_i, … t_N) of N suitable local maxima and minima.

The used ANN architecture consists of a multi-layer feed-forward fully-connected network. As described in Appendix A, this type of ANN is formed by an input layer, one or more hidden layers, and one output layer, where each layer is formed by a fixed number of nodes that represent the artificial neurons, Moreover, each node of each layer is connected to every one of the adjacent layers.

The number of nodes used for characterizing both the input and the hidden layers will be discussed in the following sections. Instead, it is worth noting that, for the purposes of the diagnostic method, only ANN architectures—having as the output layer only a single node—were designed. This choice has been made in order to provide an output of type Yes/No, depending on the presence (Yes) or absence (No) of the breast tumor.

4.2.4. ANN Processing of Single Backscattered Radar Signals

The first mandatory objective of the proposed approach is to develop an accurate algorithm able to detect a cancer by working on the single radar trace. To this end, a fundamental step is to choose and extrapolate, from the trace of the backscattered radar signal, the data that best characterize the presence of the tumor. In order to better focus the problem, many radar signals—measured on several 2D healthy breast geometries in which a dielectric anomaly was inserted at different depths inside the breast tissues—were simulated and analyzed. The observed results can be summarized analyzing the waveforms reported in Figure 4.4 and Figure 4.5.

Figure 4.4 shows the results obtained in the case where the DGP with central frequency 2 GHz is used. In particular, Figure 4.4(a) shows the cleaned radar signal measured on a 2D realistic healthy breast geometry, namely in absence of any dielectric anomalies. Figure 4.4(b) shows the radar signal measured on the same healthy geometry in which a dielectric anomaly—of diameter 6 mm—was inserted at a depth of 1.5 cm from the outer surface of the skin. It worth noting that such an anomaly is located outside from the fibro-glandular tissues area. At last, Figure 4.4(c) refers to the case where the same dielectric anomaly was inserted at a depth of 1 cm inside the fibro-glandular tissues, corresponding to 3-cm depth from the outer skin surface.

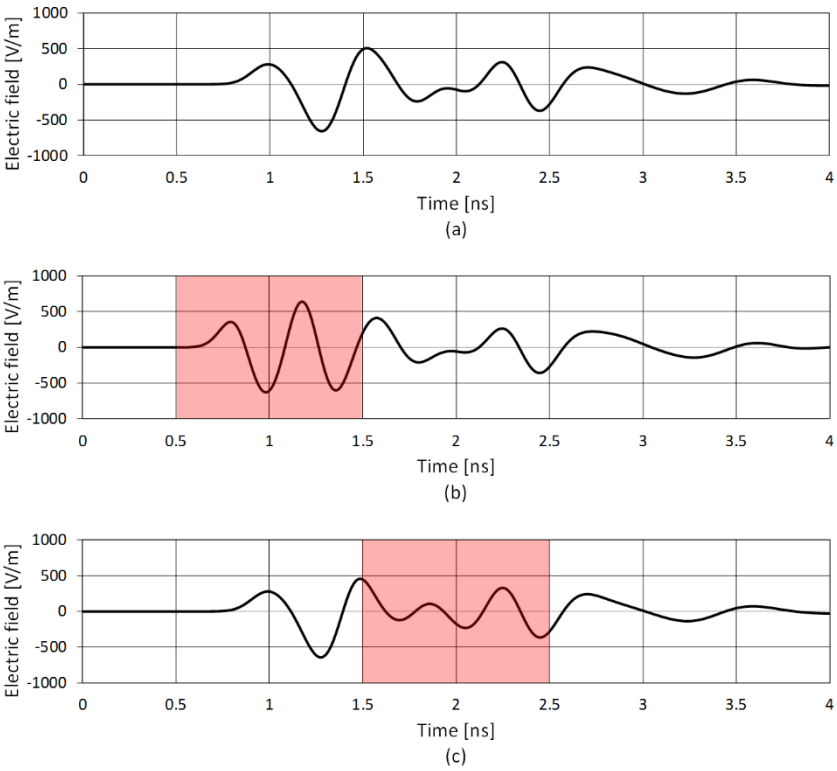

Figure 4.4. Ideally cleaned-equalized radar signals measured on a 2D healthy geometry where: a dielectric anomaly is inserted under different conditions; the DGP at 2 GHz is used. (a) Healthy breast geometry in absence of the anomaly. (b) Tumor (6-mm diameter) positioned at 1-cm depth from the skin surface, and outside the fibro-glandular tissues. (c) Same tumor positioned at a depth of 1 cm inside the fibro-glandular tissues, and 3 cm from the outer skin surface. The tumor contribution is red highlighted.

Comparing Figure 4.4(a) with Figure 4.4(b), it is evident that, if the tumor is located outside the fibro-glandular tissues, only the first part of the cleaned radar signal is strongly influenced by its presence. In fact, the major differences are highlighted in the time interval of 0.5–1.5 ns. Differently, if the tumor is positioned inside the fibro-glandular tissues, the first part of the cleaned radar signal is not influenced significantly. In fact, comparing Figure 4.4(a) with Figure 4.4(c), the greater differences are contained inside the time interval between 1.5 ns and 2.5 ns.

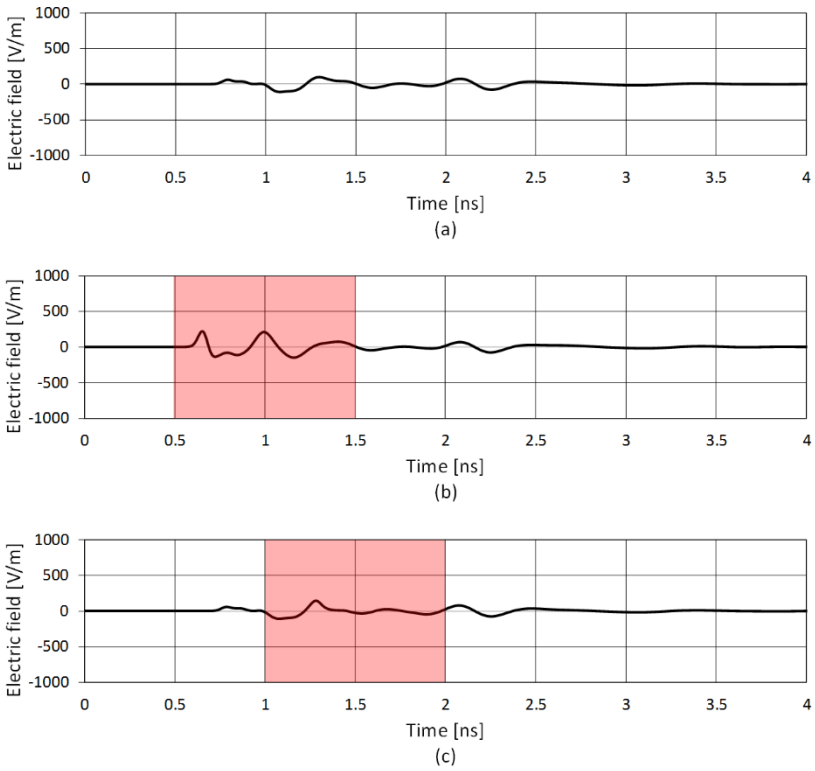

Figure 4.5. Ideally cleaned-equalized radar signals measured on a 2D healthy geometry where: a dielectric anomaly is inserted under different conditions; the DGP at 2 GHz is used. (a) Healthy breast geometry in absence of the anomaly. (b) Tumor (6-mm diameter) positioned at 1-cm depth from the skin surface, and outside the fibro-glandular tissues. (c) Same tumor positioned at a depth of 1 cm inside the fibro-glandular tissues, and 3 cm from the outer skin surface. The tumor contribution is red highlighted.

Differently, Figure 4.5 shows the results obtained in the case where the DGP at 6 GHz is used. The healthy and cancerous breast geometries used for the simulations are the same that were used in the previous case. In particular, Figure 4.5(a) shows the cleaned radar signal measured on the 2D realistic healthy breast geometry. Figure 4.5(b) shows the radar signal measured on a cancerous geometry in which a dielectric anomaly—of diameter 6 mm—has been inserted at a depth of 1.5 cm from the outer skin surface, and out from the fibro-glandular tissues. Figure 4.5(c) shows the case of the dielectric anomaly positioned 1-cm depth inside the fibro-glandular tissues.

Also in this case, if the tumor is located outside the fibro-glandular tissues, only the first part of the signal is influenced by its presence. In fact, comparing Figure 4.5(a) with Figure 4.5(b), the differences are highlighted in the time interval between 0.5 ns and 1.5 ns. Moreover, looking at Figures 4.5(a) and 4.5(c), if the tumor is positioned inside the fibro-glandular tissues, the first part of the signal does not change significantly, and the major differences are contained in the time interval between 1 ns and 2 ns.

The above analyses and considerations suggest that the research of tumors that are located outside and inside the fibro-glandular tissues can be conducted in a separately way. Following this criterion, a process able to detect breast tumors located outside the fibro-glandular tissues is separately applied using only the first part of the cleaned radar signal, whereas another process is applied in order to detect the presence of tumors located inside the fibro-glandular tissues by using the second part of the same signal. In this context, a schematic flow-chart of the detection algorithm that is proposed for processing the single radar trace is reported Figure 4.6. According to Figure 4.6, two sets of data—I_1 and I_2—are extracted, from the cleaned-equalized radar signals, and then provided to two different and properly specialized ANNs. The designed ANNs will be described in the following sections.

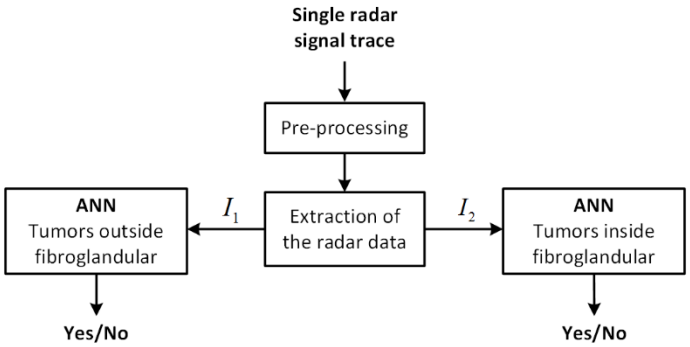

Figure 4.6. Schematic flow chart of the detection algorithm applied to each single radar trace.

4.2.5. Diagnostic Criterion

As described in the previous Section 4.2.4, the first key step is to extract significant and suitable information from any single radar trace. However, in order to improve the accuracy, the proposed method also includes the application of a diagnostic criterion that is based on a collective analysis of all the results obtained for each

single radar trace. As described in the flow-chart reported in Figure 4.6, the proposed algorithm provides only an answer of type Yes/No for each single mono-static radar position, where each answer may fall in a false-positive or a false-negative result.

In order to minimize the statistical number of wrong diagnoses and to provide a reliable diagnostic response, the proposed diagnostic criterion consists of giving credibility to a Yes answer only when such output is obtained consecutively for a given arc of positions, or for a given percentage of detections inside it. In this way, by applying the diagnostic criterion, single and isolated detections do not produce positive diagnoses, avoiding of falling into false positive results. The same procedure is applied for the negative diagnoses. On the basis of this idea, it is possible not only to improve both the specificity and sensitivity values of the diagnostic method as a whole, but also to better localize the angular zone of the tumor's location.

4.3. Results

4.3.1. Tumors Located Outside the Fibro-Glandular Tissues

This section presents the ANN architecture that was designed for the detection of tumors located outside the fibro-glandular tissues. As mentioned in in the previous sections, in these situations, it is reasonable to assume that the information on the tumor presence—the so-called tumor signature—is contained in the first part of the cleaned-equalized radar signals. According to this assumption, it was chosen to exploit the information that is contained in the first two local maxima/minima of the cleaned-equalized radar signals, where a graphical representation is reported in Figure 4.7. In particular, Figure 4.7(a) shows a cleaned-equalized radar signal—measured on a 2D cancerous geometry using the DGP with central frequency 2 GHz—in which the first two maxima/minima are highlighted in red, whereas Figure 4.7(b) shows the case where the DGP at 6 GHz is used.

During this first analyses, in order to preliminarily assess the abilities of the proposed ANN-based detection approach, the cleaned radar signals were obtained applying an ideal cleaning technique. As mentioned in the previous sections, it consists of subtracting, from the total signal, the radar signal measured on a two-layered geometry of shape and dimension equal to those of the realistic geometry, but formed by only the skin and adipose tissues. It worth noting that, the two tissues of the cleaning model are characterized by the same Debye parameter values of the respective realistic geometry.

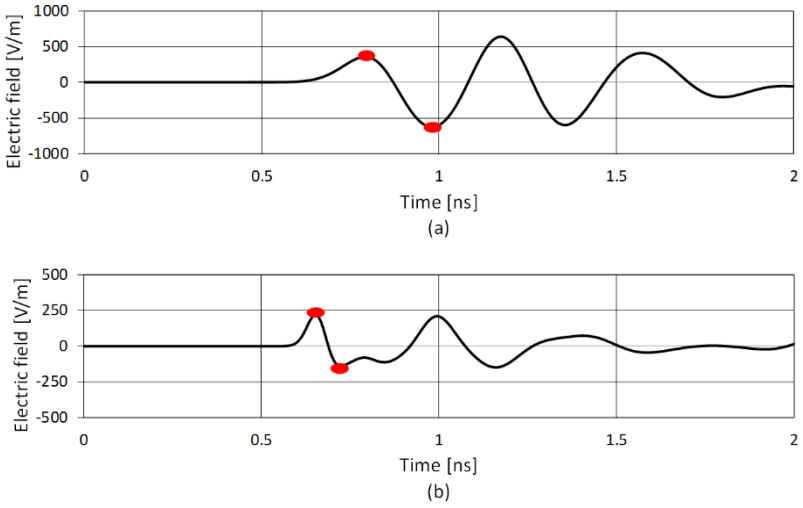

Figure 4.7. Ideally cleaned-equalized radar signals measured on a 2D realistic heterogeneous breast geometry. (a) 2-GHz DGP at. (b) 6-GHz DGP.

The used ANN architecture is of type 4-8-1. It presents one hidden layer of eight nodes and an input layer of four nodes. Such a network, receives four input data consisting of the arrival times and the amplitudes of the firsts two maxima/minima measured on the ideally cleaned radar signals. As mentioned in Section 4.2.3, it provides one output of type Yes/No, depending on the presence, or absence, of the tumor.

According to the number of degrees of freedom of such an ANN architecture, the network was trained using 100 training data, consisting of 50 measured on cancerous geometries (T) and 50 measured on healthy geometries (NT). In conclusion, two different networks were trained: the first was formed using the radar signals measured with the DGP at 2 GHz (hereafter named ANN-4-8-1-DGP-2-GHz), whereas the second was trained using the DGP at 6 GHz (hereafter named ANN-4-8-1-DGP-6-GHz). For the only purposes of training the ANN, the dielectric anomaly was positioned by respecting one constraint: the anomaly must be the first internal discontinuity that the radar signal encounters within the breast geometry. As example, one of the used 2D cancerous breast geometries is reported in Figure 4.8.

The results obtained during the training phase gave a tumor detection accuracy of 100% for both the two ANNs. This result implies that, for both the two incident pulses, the designed ANN architecture was able to adjust both the bias and weights of its internal nodes, namely it has found the best connections between the input-out pairs that were furnished during the learning process.

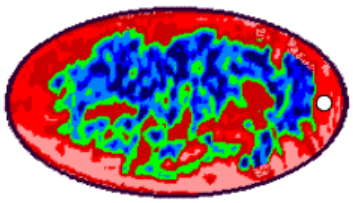

Figure 4.8. Example of a cancerous geometry. A dielectric anomaly of 4-mm diameter is positioned outside the fibro-glandular tissues at 0.5-cm depth from the outer skin surface. Blue colors indicate the three typologies of fibro-glandular tissues; green color represents the intermediate tissue; red colors indicate the three adipose tissues.

In order to assess the generalization capabilities using a significant scenario, two sets of new 100 testing data were generated and simulated, namely 50 T and 50 NT. The first set has been obtained using the DGP at 2 GHz, and the other with the 6-GHz DGP. The new test data were generated by always respecting the constraint on the position of the tumor.

Table 4.1 shows the results—in terms of the confusion matrix—that were obtained for the network ANN-4-8-1-DGP-2-GHz, whereas the results obtained for ANN-4-8-1-DGP-6-GHz are shown in Table 4.2.

Looking at Table 4.1, it is evident that, in the case where the DGP at 2 GHz is used, the designed ANN has detected the presence of the dielectric anomaly with a sensitivity of 92%, a specificity of 90%, and an overall accuracy of 91%. On the other hand, looking at Table 4.2, in the case where the DGP at 6 GHz is used the anomaly is detected with a sensitivity of 88%, a specificity of 78%, and an overall accuracy of 83%.

Table 4.1. Confusion matrix, ANN-4-8-1-DGP-2-GHz, 100 testing examples, constraints on the T location, and ideal cleaning technique. The overall accuracy is 91%.

Type	**Test Number**	**ANN output**		**ANN performance (%)**	
		Yes	*No*	*Sensitivity*	*Specificity*
T	50	46	4	92	/
NT	50	5	45	/	90

Table 4.2. Confusion matrix, ANN-4-8-1-DGP-6-GHz, 100 testing examples, constraints on the T location, and ideal cleaning technique. The overall accuracy is 83%.

Type	Test Number	ANN output		ANN performance (%)	
		Yes	*No*	*Sensitivity*	*Specificity*
T	50	44	6	88	/
NT	50	11	39	/	78

4.3.2. Tumors Positioned Inside the Fibro-Glandular Tissues

This section is focused on the problem of detecting tumors that are located deep inside the fibro-glandular tissues. Following the concepts explained in the previous sections, in order to best characterize the tumor's presence, suitable information is searched inside the second part of the cleaned-equalized radar signals. In order to train and test new ANNs, new healthy and cancerous 2D realistic breast geometries were built by positioning the dielectric anomaly inside the fibro-glandular tissues. As example, one of the used cancerous geometries is shown in Figure 4.9.

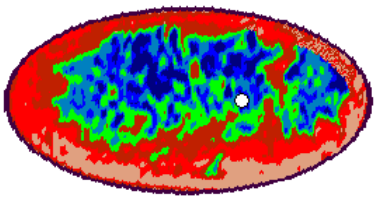

Figure 4.9. A cancerous geometry in which a dielectric anomaly of diameter 4 mm is located inside the fibro-glandular tissues at a depth of 3.5 cm from the skin surface. The blue colors indicate the three typologies of fibro-glandular tissues, the green parts represent the intermediate tissue, and the red colors indicate the three typologies of adipose tissue.

At this point, different ANN architectures that work on different sets of input data were trained and tested. All the networks were designed in order to provide a binary output of type Yes/No. In particular, an ANN architecture of type 6-12-1 was designed for working on the amplitudes and arrival times of the 3°, 4° and 5°

maximum/minimum of the ideally cleaned-equalized radar signals. Moreover, another architecture of type 4-8-1 was designed for working respectively on the amplitudes and arrival times of the 3°-4° maximum/minimum, and on the same data measured for the 4°-5° maximum/minimum. All the networks were trained and tested using both the two different UWB incident pulses.

According with the number of degrees of freedom, each network was trained using a fixed number of training data. In particular, the architecture of type 4-8-1 was trained using 100 training examples, namely 50 T and 50 NT. Differently, the 6-12-1 architecture has been trained using a set of 200 input-output pairs, namely 100 T geometries and 100 NT geometries. The results obtained during the training processes are reported in Table 4.3 and Table 4.4. In particular, Table 4.3 reports the results obtained in the case where the DGP at 2 GHz is used, and Table 4.4 shows the results obtained using the 6-GHz DGP. The results show that all the networks have been able to find the connections between the input-out pairs that were furnished during the learning process in a satisfactory way.

Table 4.3. Performance on training data - 2 GHz

ANN architecture	**ANN performance (%)**		
	Accuracy	*Sensitivity*	*Specificity*
4-8-1 (3°-4° peak)	98	96	100
4-8-1 (4°-5° peak)	98	96	100
6-12-1 (3°-4°-5° peak)	100	100	100

Table 4.4. Performance on training data - 6 GHz

ANN architecture	**ANN performance (%)**		
	Accuracy	*Sensitivity*	*Specificity*
4-8-1 (3°-4° peak)	98	96	100
4-8-1 (4°-5° peak)	96	98	94
6-12-1 (3°-4°-5° peak)	98	98	98

In order to test the networks with a significant scenario of testing data, new radar signals were simulated using new healthy and malignant breast geometries. The ANNs of type 4-8-1 were validated using 100 new testing data, 50 T and 50 NT, whereas the ANNs of type 6-12-1 were tested using 200 new geometries, 100 T and

200 NT. Table 4.5 and Table 4.6 show the results that were obtained by respectively using the 2-GHz DGP and the 6-GHz DGP.

Looking at Tables 4.5 and 4.6, it is evident that the only more acceptable results were obtained by using the DGP at 2 GHz and the ANN 4-8-1 that works on the 3°-4° maximum/minimum measured on the ideally cleaned-equalized radar signals. Using this ANN, the tumor presence has been detected with a sensitivity of 69%, a specificity of 67%, and an overall accuracy of 68%.

Table 4.5. Performance on testing data - 2 GHz

ANN architecture	**ANN performance (%)**		
	Accuracy	*Sensitivity*	*Specificity*
4-8-1 (3°-4° peak)	68	69	67
4-8-1 (4°-5° peak)	47	58	36
6-12-1 (3°-4°-5° peak)	55	54	56

Table 4.6. Performance on testing data - 6 GHz

ANN architecture	**ANN performance (%)**		
	Accuracy	*Sensitivity*	*Specificity*
4-8-1 (3°-4° peak)	51	56	46
4-8-1 (4°-5° peak)	50	52	48
6-12-1 (3°-4°-5° peak)	48	48	47

4.4. Robustness Assessment Study of ANN-4-8-1-DGP-2-GHz

In the previous Section 4.3.1, it has been shown that the best results are obtained using the network ANN-4-8-1-DGP-2-GHz. This ANN is specialized for the detection of tumors—of diameters between 0.2 cm and 1.0 cm—that are located at different random depths outside the fibro-glandular tissues. It receives, as input data, the amplitudes and arrival times of the first two maxima/minima measured on the ideally cleaned-equalized radar signals in the case where the 2-GHz DGP is used.

Since the previous analyses were performed considering a limited scenario of test data in the case where an ideally cleaning technique is applied, in this section, a robustness assessment study of such a network is presented.

First, a broader and more generic set of test data—consisting of new healthy and cancerous 2D breast models—is considered. In the new cancerous geometries, the tumor is positioned without the constraint used in Section 4.3.1, moreover it is introduced also the case where the anomaly is located in contact with the outer surface of the fibro-glandular tissues. Using this new scenario, an analysis of the sensitivity values, when varying both the depth and dimensions of the tumor, is provided. As the second step, the performance is assessed in the case where the skin-artifact component is suppressed by using a realistic model-based skin-artifact removal technique. Finally, the designed network ANN-4-8-1-DGP-2-GHz is tested by using the data measured on a realistic 3D breast model taken from the UWCEM database in the case where an ideal skin-artifact removal technique is applied.

4.4.1. Generic Testing Data Without Constraints on the Tumor Position

In order to validate the ANN using a more general data set, 2000 new realistic 2D breast geometries, 1000 T and 1000 NT, were generated with the anomaly positioned outside the fibro-glandular tissues but without any constraint. As example, Figure 4.10 shows one of the new cancerous geometries that were generated and tested.

In order to initially assess the changes introduced on the performance, the cleaned-equalized radar signals were obtained by applying the ideal skin-artifact removal technique described in Section 4.2.2. The obtained results are presented in terms of the confusion matrix in Table 4.7. The table shows that the tumor presence has been detected with a sensitivity of 81%, a specificity of 79%, and an overall accuracy of 80%.

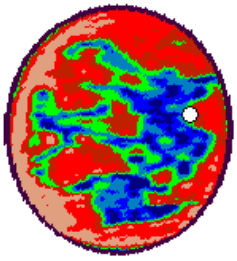

Figure 4.10. Example of the cancerous models used for the general test with 2000 new breast geometries. A tumor of 4-mm diameter is positioned at 1-cm depth from the skin surface.

Table 4.7. Confusion matrix, ANN-4-8-1-DGP-2-GHz, 2000 testing examples, no constraints on the T location, and ideal cleaning technique. The overall accuracy is 80%.

Type	Test Number	ANN output		ANN performance (%)	
		Yes	*No*	*Sensitivity*	*Specificity*
T	1000	810	190	81	/
NT	1000	214	786	/	79

A histogram that summarizes the statistical sensitivity values, obtained for the 1000 cancerous breast models used for Table 4.7, is reported in Figure 4.11. This graph reports different values of sensitivity by subdividing them into different single classes in accordance with distinct ranges of both the depths and dimensions of the tumor. The depth is measured from the outer skin surface.

The figure shows that, in the case where the depth varies in the range of 0.5 cm and 1.5 cm, the sensitivity is 71% for tumors of diameter between 2 mm and 4 mm, 94% for tumor diameters between 4 mm and 6 mm, 88% for diameters between 6 mm and 8 mm, and 79% for diameters between 8 mm–10 mm. Differently, for depths greater than 1.5 cm, the sensitivity is 77% for tumors of diameter between 2 mm and 4 mm, 71% for tumor diameters between 4 mm–6 mm, 74% for diameters between 6 mm–8 mm, and 9% for diameters between 8 mm–10 mm.

It worth noting that, if the analysis is limited to only the tumors with a depth that ranges between 1,5 cm and 2.5 cm, the value of sensitivity reaches the 70%. Moreover, if the cases of tumor with a depth greater than 2.5 cm are excluded from the 1000 cancerous models used for Table 4.7, the global sensitivity value increases to 83%.

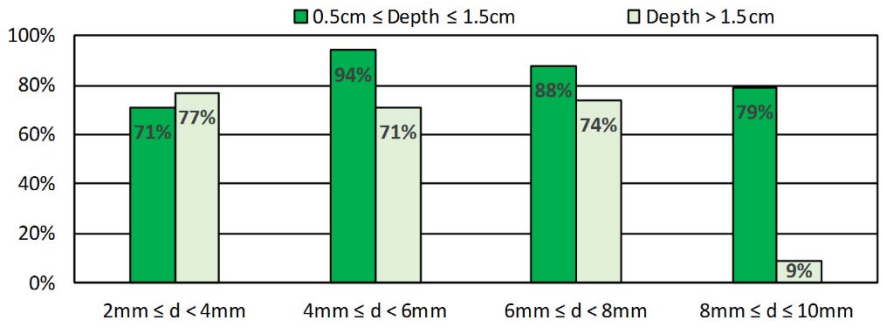

Figure 4.11. The sensitivity for different classes of the depth and dimension of the tumor. The 1000 cancerous geometries used for Table 4.7 were here considered.

4.4.2. Application of a Model-Based Skin-artifact Removal Technique

As mentioned in the previous sections, up to now the cleaned radar signals were obtained using an ideal skin-artifact removal technique that was applied in order to preliminarily assess the abilities of the proposed ANN-based detection approach. The analysis of the network when it is applied to an ideal scenario is important in order to provide a baseline evaluation of the algorithm's capacitances. Nevertheless, a review of the literature on the topic of the skin suppression techniques [7, 8, 9, 10], suggests that to accurately suppress the strong skin contributions is a challenging task. In fact, in a realistic scenario, the cleaning algorithm may suppress the skin response, but significant residual effects—such as signal distortions and noise introduction—may be present after the application of the cleaning technique. Moreover, the suppression algorithm may alter the tumor signature and degrade the performance of the detecting approach.

This section presents an analysis of the performance of the proposed approach in the case when the cleaned radar signals are obtained by applying a realistic model-based skin-artifact removal algorithm. This last is accurately described in Appendix B. The applied cleaning technique involves the use of a reference cleaning model in order to measure the backscattered signal that is used as the cleaning signal. Then, the measured cleaning signal is subtracted from the total real one in order to obtain the cleaned signal. The reference model is characterized by a two-layers cylinder consisting of the skin and the adipose tissue. The important parameters that compose the reference cleaning model are: the values of the Debye parameters for the dielectric characterization of both the two biological tissues, the skin thickness, the model dimensions, and the distance between the skin interface and the radar antenna.

In the study reported in Appendix B it was found that the distortions, that are introduced during the cleaning process, are minimized in the case where a reference cleaning model—with a radius of 11 cm—is used by placing it at the same actual distance between the skin and the radar antenna. Moreover, the best results are obtained under the a-priori assumption of knowing the real values for characterizing the skin thickness and the static dielectric permittivity (ε_s) of both the skin and adipose tissue. In contrast, the other dielectric Debye parameters (ε_∞, σ, and τ) remain fixed at average standard values, where these last have been obtained by averaging the range of values provided in the literature [6].

Respecting the above constraints, the reference cleaning models were configured and applied to all the 2000 realistic breast models used and described in Section 4.4.1. Once obtained all the new cleaned signals, the amplitudes and arrival times of the first two maxima/minima were extracted and tested on the network ANN-4-8-1-DGP-2-GHz.

The obtained results are reported in Table 4.8 in terms of the confusion matrix. This table shows that the network detected the tumor with a sensitivity of 78%, a specificity of 74%, and an overall accuracy of 76%.

However, the Appendix B shows that satisfactory results are achieved also using more generic reference cleaning models, where these last are characterized by average standard values for all the Debye dielectric parameters (ε_s, ε_∞, σ, and τ) that describe the two biological tissues. Even in this case, the standard values are obtained by averaging the range of values provided in literature [6]. Moreover, in Appendix B it is also shown that better results are obtained in the case where the network is trained with training data that are measured on radar signals cleaned by using the generic reference cleaning models. For this reason, a new network—named ANN-4-8-1-DGP-2-GHz-Generic-Model-Based—was trained by using the generic reference cleaning models composed by only dielectric standard values. The new network was tested using the same 2000 realistic breast models previously described and used, and by applying the generic model-based cleaning technique.

Table 4.9 shows the obtained results in terms of the confusion matrix. The tumor's presence was detected with a sensitivity of 74%, a specificity of 73%, and an overall accuracy of 74%.

Table 4.8. Confusion matrix, ANN-4-8-1-DGP-2-GHz, 2000 testing examples, no constraints on the T location, and model-based cleaning technique. The overall accuracy is 76%.

Type	**Test Number**	**ANN output**		**ANN performance (%)**	
		Yes	*No*	*Sensitivity*	*Specificity*
T	1000	784	216	78	/
NT	1000	257	743	/	74

Table 4.9. Confusion matrix, ANN-4-8-1-DGP-2-GHz-Generic-Model-Based, 2000 testing examples, no constraints on the T location, and generic model-based cleaning technique. The overall accuracy is 74%.

Type	**Test Number**	**ANN output**		**ANN performance (%)**	
		Yes	*No*	*Sensitivity*	*Specificity*
T	1000	742	258	74	/
NT	1000	267	733	/	73

This last result is very interesting and highly significant, because it means that satisfactory values of accuracy are reached also in the case where a skin suppression algorithm is applied without any a-priori knowledge on both the dielectric and geometric properties of the skin and the adipose tissue, namely what happens in realistic and practical situations. It worth noting that, the only parameter that has been assumed to be known is the skin thickness.

4.4.3. Test with a 3D Realistic Cancerous Breast Model

This section presents the results obtained by testing the network ANN-4-8-1-DGP-2-GHz with data measured on a realistic 3D breast model taken from the UWCEM database. As described in Section 3.3.1.1, this database provides nine realistic breast phantoms, subdividing them into four main classes: *mostly fatty*, *scattered fibro-glandular*, *heterogeneously dense*, and *very dense*. In the present test, the chosen 3D breast model belongs to the scattered fibro-glandular class, where it is distinguished by ID 010204. The values of the Debye parameters, that were used to dielectrically characterize the breast healthy tissues, are reported in Table 4.10 [6]. According with the previous analyses, the tumor has been dielectrically characterized with ε_s of 61.6, ε_∞ of 14.5, σ of 0.7 S/m, and τ of 13 ps.

Table 4.10. Values of the Debye parameters used for dielectric characterization of healthy breast tissues.

Breast Healthy Tissue	**Debye dielectric parameter**			
	ε_s	**ε_∞**	**σ (S/m)**	**τ (ps)**
Fibroglandular-1	54.690	14.200	0.824	13.00
Fibroglandular-2	49.360	13.810	0.738	13.00
Fibroglandular-3	37.390	12.990	0.397	13.00
Intermediate	22.461	8.4890	0.239	13.00
Adipose-1	7.532	3.987	0.080	13.00
Adipose-2	4.708	3.116	0.050	13.00
Adipose-3	3.952	2.848	0.005	13.00
Skin	39.760	15.930	0.831	13.00

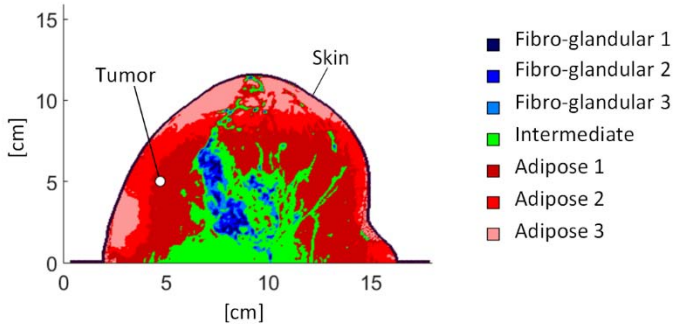

Figure 4.12. Sagittal section of the used 3D model. A tumor of 4-mm diameter is positioned at a depth 1.5 cm from the skin and at a distance 5 cm from the chest.

Different tumor situations were modeled by positioning the dielectric anomaly at three different distances from the chest—namely 2 cm, 5 cm, and 8 cm—and at a depth of 1.5 cm from the outer surface of the skin. For each tumor positions, anomalies of different diameters were considered, namely 2 mm, 4 mm, 6 mm, 8 mm, and 10 mm. A sagittal section of one the used 3D realistic cancerous breast models is reported in Figure 4.12. In such a model, a tumor of 4-mm diameter is positioned at 1.5-cm depth from the skin and at a distance of 5 cm from the chest.

In order to suppress the skin reflections, the ideal technique described in Section 4.2.2 was applied. Then, starting from the ideally cleaned-equalized radar signal, the amplitudes and arrival times of the first two maxima/minima were extracted and tested on the network previously trained and tested using 2D geometries, the so-called ANN-4-8-1-DGP-2-GHz.

The obtained results indicate that the designed network correctly detects tumors positioned at a depth of 1.5 cm from the outer skin surface and characterized by a diameter as small as 2 mm.

4.5. Diagnostic Criterion Assessment

In this section, the improvements that derive by the application of the diagnostic criterion, described in Section 4.2.5, are presented by reporting some numerical results. Because the endpoint of this analysis is to preliminarily assess the improvements that are introduced, the performance is evaluated in the case where

the algorithm is applied to an ideal scenario, namely using the radar signals cleaned by means of the ideal skin-artifact removal technique described in Section 4.2.2.

The diagnostic criterion has been tested in the case of tumors located outside the fibro-glandular tissues when the DGP at 2 GHz is used. Starting from the 2000 models described in Section 4.4.1, 10 two-dimensional realistic breast models—consisting of 5 T and 5 NT—were chosen. For each of these, 72 different radar signals were collected in 72 different angular positions around the breast geometry.

Using all the simulated radar traces, the network ANN-4-8-1-DGP-2-GHz was tested with the amplitudes and arrival times of the first two maxima/minima extracted from the ideally cleaned-equalized radar signals. Finally, the diagnostic criterion has been applied to the outcomes provided by the network and highly satisfactory results were obtained.

In the case of the NT breast geometries, even if the network has wrongly detected the anomaly as malignant in isolated angular positions, by applying the diagnostic criterion the definitive outcomes of the diagnostic technique have been only true-negative results. Moreover, in the cases of the T breast geometries, the network has produced few wrong answers in some isolated angular positions, but also consecutives corrected detections inside a cone of about 30° centered on the actual position of the tumor.

It worth noting that, the true-positive answers were detected under angles of approximately 30° of consecutive malignant detections (Yes), and the true-negative answers were detected under higher angles of consecutive non-malignant detections (No). For this reasons, it was found acceptable giving credibility only to arcs of at least 30° of consecutive malignant detections, or at least containing a percentage of them greater than a fixed threshold. For the analyzed cases, it has been found that such a percentage was always at least 70% for angles of 30°. As examples, Figure 4.13 shows three of the 10 geometries used to assess the diagnostic criterion.

Figure 4.13(a) shows an NT geometry where the outcomes of the ANN are reported for all the angular positions. The red points represent the isolated false-positive detections. The correct diagnosis is performed by giving credibility only to the large arcs of negative detections, that are represented as black points.

Figure 4.13(b) shows the results obtained on a cancerous geometry, where the malignant detections are highlighted as red points. Besides few isolated wrong detections, the figure shows that the tumor is detected as malignant under an angle of 30° of consecutive red points.

Finally, Figure 4.13(c) shows the case of another T geometry for which, inside the arc of corrected malignant detections, there is a single and isolated "No" answer, consisting of the isolated black point. In this case, by giving credibility to the arc of malignant detections, it is avoided to fall in a false-negative diagnosis.

The above considerations highlight the importance of applying the diagnostic criterion in order to provide high values of sensitivity and specificity, reaching for the cases here presented an accuracy of 100%, but also the possibility of correctly localizing the angular position of the detected tumor.

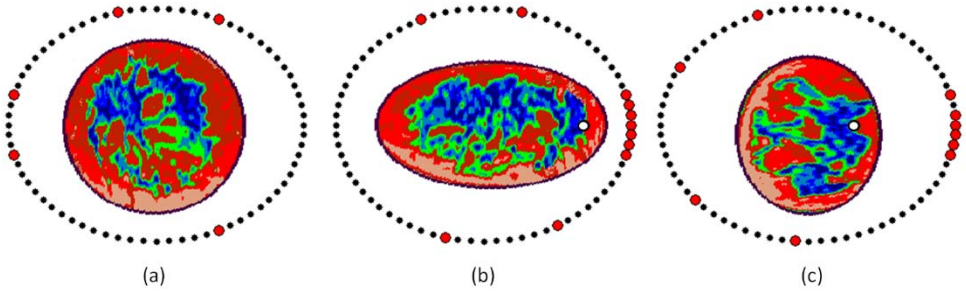

Figure 4.13. Three of breast geometries used to test the diagnostic criterion, where the red and black points represent respectively the malignant and non-malignant detections. (a) Healthy breast geometry for which the ANN wrongly detects a malignant tumor only on single isolated radar positions. (b) Cancerous breast geometry for which the ANN correctly identifies the malignant tumor under a 30° angle of 100% consecutive malignant detections. (c) Cancerous geometry for which there is one isolated wrong result inside the arc of correct malignant detections. In this situation the tumor is correctly identified under a 30° angle with 85% of malignant detections.

5. Conclusions

In the chapters of this Ph.D. thesis, a new breast cancer radar detection technique, based on the use of artificial neural networks (ANNs), was proposed and assessed. The final purpose is not the breast imaging, but to provide a Yes/No diagnostic tool able to detect the presence, or absence, of a tumor with the highest possible values of sensitivity, specificity, and overall accuracy.

The numerical analyses were conducted using realistic 2D and 3D healthy and cancerous breast geometries derived from the models provided by the UWCEM database. A mono-static radar system configuration was assumed to measure the simulated backscattered signals in different space locations situated at different distances from the chest and along a circular line around the breast.

The proposed approach is based on processing—through the use of ANNs—suitable data that are extracted from any single backscattered radar trace measured around the breast. In this way, for each single mono-static radar position, the ANN provides a Yes/No answer that determines the presence/absence of the tumor, then the final diagnosis response is achieved by applying a diagnostic criterion on the basis of a collective evaluation of all the ANN answers. According to such a criterion, the diagnostic outcomes will be either "Yes" and "No" only when such outputs are obtained consecutively for a given arc of radar positions, or for a given percentage of detections inside it. In this way, single and isolated malignant detections do not produce positive diagnoses—avoiding of falling into false-positive results—and in the same way single and isolated healthy detections do not produce negative diagnoses—avoiding false-negative results.

First, using an ideal skin-artifact removal technique and realistic 2D healthy and cancerous breast geometries, the cases of tumors located both outside and inside the fibro-glandular tissues were studied. During these firsts analyses, the use of two different UWB illuminating pulses was assessed. The best results were obtained when the differentiated Gaussian pulse with a central frequency 2 GHz is used. In

the case of tumors located outside the fibro-glandular tissues, an overall accuracy of 91% on 100 test data was obtained, whereas for tumors located inside the fibro-glandular tissues the overall accuracy was 68%. Despite the latter result seems to be not very satisfactory, it ranks in the range of accuracy values—63.6–75.6 %—that are reached combining the use of the actual main clinical diagnostic techniques.

Because of the highly satisfactory results obtained for tumors located outside the fibro-glandular tissues, this topic was more deeply investigated and a robustness assessment study was performed by considering a more generic and realistic scenario of test data.

First, the ANN was tested using a broader and more generic set of 2000 new 2D healthy and cancerous breast geometries. The obtained results showed that the tumor presence was detected with a sensitivity of 81%, a specificity of 79%, and an overall accuracy of 80%. Moreover, if the cases of tumors located at a depth from the outer skin surface greater than 2.5 cm are excluded from the analysis, the value of sensitivity increases to 83%.

Second, the performance of the proposed approach was assessed in the case where the cleaned radar signals are obtained by applying the realistic model-based skin-artifact removal technique proposed in Appendix B. In this realistic situation, the tumor was detected with a sensitivity of 74%, a specificity of 73%, and an overall accuracy of 74%. This last is a highly significant result because it means that a satisfactory value of accuracy, that is at the top of the range of values—from 63.6 % to 75.6 %—reached by the actual clinical diagnostic techniques, can be obtained also in the case where a cleaning technique is applied without assuming any a-priori information on the actual both geometric and dielectric characterizations of the breast.

Third, the proposed diagnostic technique was assessed using data measured on a realistic 3D breast model taken from the UWCEM database, and applying an ideal cleaning technique. In this realistic case, the designed network has correctly detected tumors positioned at different distances from the chest and at a depth of 1.5 cm from the outer surface of skin, and characterized by different dimensions with diameter values ranging between 2 mm and 10 mm.

Finally, the proposed diagnostic criterion—based on the collective evaluation of all the ANN answers—was assessed and applied to 10 realistic 2D geometries. The obtained results showed that its application reduces completely to zero the wrong diagnostic responses. Moreover, at the same time it provides information on the exact angular position of the tumor.

6. Appendix A — The Artificial Neural Networks

6.1. Introduction

The artificial neural network (ANN) is a computational model whose aim is simulate the behavior of the human brain. To such a purpose, the ANN combines the capabilities of single, and simple, computing elements—which represent the biological neurons—highly interconnected and organized in layered structures. Generally, the ANNs are implemented using actual electronic components, or simulated using suitable software [96].

Because to their generic nature—namely their ability in adapting to a wide variety of problems—the use of ANNs can offers several advantages. Indeed, the substantial difference with respect to other computing systems consists of the fact that the ANNs are not strictly dependent from the type of data to be analyzed. An ANN is suitably trained using examples furnished in the form of input-output pairs. In this way, the network learns to connect each input to its respective output and to generalize what it has learned in order to apply it to new input data that were not used during the forming phase.

The above characteristics make the ANNs suitable for all problems and activities that have to cope with the classification or the recognition of input data. The ANNs find application in several areas such as the recognition of texts in order to detect patterns of interest inside a wide amount of data, the recognition of images, remote sensing and robotic applications, and solving the problems of inverse electromagnetic scattering. This last application is particularly interesting because the ANNs are properly indicated to solve this typology of problems. Indeed, the use of ANNs allows to avoid the inversion of the direct analytical, or numerical,

mathematical operators that describe the relation between the characteristics of the studied objects to the backscattered electromagnetic fields.

In order to acquire the knowledge that is necessary to solve the problem, the ANN needs a period of forming that requires the definition of strict rules for the choice of both the algorithm used during the training phase and the data—namely the input-output pairs—that are provided as examples. It is worth noting that this choice plays a primary role. Although the generation of a significant set of examples and the subsequent network training phase can require long times, and also a rather high computational burden, when the obtained network is used in "on-field" applications, it can provide results approximatively in real-time and with low computational burden.

In the following sections of the present appendix, the principal architectural elements and operations that are fundamental in order to design an operating artificial neural network—namely the artificial neuron, the activation function, the principal ANN architectures, and both the training and test operations—are in detail described.

6.2. The Artificial Neurons

The basic processing element of an ANN is the artificial neuron, or simply node. As represented in Figure 6.1, such an element has different incoming connections through which it receives the information, that arrives from other artificial neurons, in the form of the input vector $\overline{X} = (X_1, X_2, ..., X_n)$.

In order to model the strength of the connections between the examined neuron and the others nodes of the network, each input data is multiplied by a weight w_i and a term of Bias w_0 can be introduced.

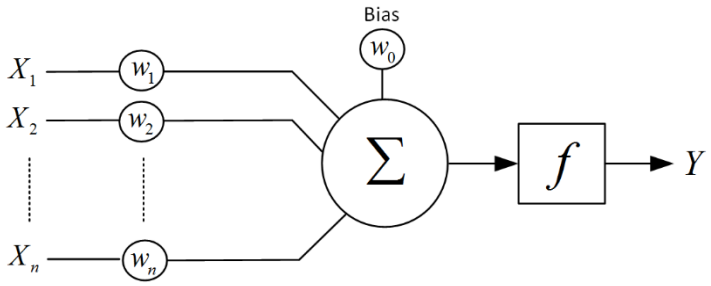

Figure 6.1. The artificial neuron, the basic processing element of the ANN.

The output consists of a single connection *Y* that provides the result of the processing, performed by the node, to the next artificial neurons. The output signal is transmitted only in the case where the sum of the bias and the weighted inputs overcomes the activation threshold of the neuron. The output is computed by applying, to the weighted sum, the activation function *f*. This last is applied in order to simulate the discharge mechanism of the neuron [97].

6.3. The Activation Functions

The activation function transmits the signal only if the sum of both the weighted inputs and bias exceeds the fixed threshold level. Moreover, in order to simulate the behavior of biological neurons, the activation function limits the output value and produces only signals of finite amplitude. Usually, the values of output range inside the closed interval [-1,1], or [0,1].

Several typologies of activation functions can be applied. Within the family that produces output values inside the range between 0 and 1, there are the so-called step, ramp, and sigmoid functions. The artificial neurons that use the step function have a binary behavior and are known as the McCulloch-Pitts models [96]. The ramp function has a linear behavior for the values of abscissa included between -1/2 and +1/2, and a binary behavior outside such an interval.

Differently, as described in Equation 6.1, the sigmoid function, can assume a continuous range of values inside the entire interval [0, 1]. Moreover, it has the characteristic of being differentiable.

$$f(x) = \frac{1}{1 + e^{-\sigma x}} \tag{6.1}$$

The term σ is used in order to control the variation steepness. As reported in Equation 6.2, this function can be also defined inside the range between -1 and 1. In this case, it has known with the name of bipolar sigmoid.

$$f(x) = \frac{1 - e^{-\sigma x}}{1 + e^{-\sigma x}} \tag{6.2}$$

Other functions used to produce output values inside the interval [-1,1], are the sign and ramp functions. The sign function is characterized by a binary behavior. The ramp function provides a linear behavior for the values of abscissa included in the range between -1/2 and +1/2, and a binary behavior outside it.

6.4. Artificial Neural Network Architectures

The choice of the ANN architecture—namely the number of layers, nodes for each layer, and the way in which the artificial neurons are each other connected—greatly affect the training algorithm used to form the network. In general, three principal families of architectures can be distinguished: the single-layer feed-forward networks, the multi-layer feed-forward networks, and the recurrent networks.

The single-layer feed-forward typology represent the simplest architecture of artificial neural network, and it consist of using one input layer whose nodes are directly connected to the nodes of the output layer.

The multi-layer feed-forward architectures use one or more hidden layers that are placed between the input and output layers. The presence of the hidden layers allows the network to treat data related to problems of higher-order. Moreover, because to the additional connections introduced, the network acquires a "global" view of the problem [98]. An architecture in which all the nodes of each layer are connected to every node of the adjacent layers is named fully-connected, whereas, if some connections are missed the network is defined partially-connected.

Finally, the recurrent typologies are ANN architectures that contain at least one feedback loop. The presence of feedback can greatly improve the learning capacity of the network and its performance [96].

6.5. The Multilayer Feed-Forward Artificial Neural Networks

In this section, the multi-layer feed-forward architecture is described in detail. A representation of such a type of network is shown in Figure 6.2. In particular, the figure shows an ANN composed by one input layer, one output layer, and two generic hidden layers. Usually, the elements of the first level perform solely the role of buffer layer between the external world and the ANN itself. The hidden nodes receive several input branches, namely the connections to all the outputs of the artificial neurons of the previous level. In addition, each single element provides an output that is passed to the nodes of the next layer, or directly to the external world in the case of nodes of the output level. Moreover, to each connection is associated a constant representing the weight of the connection, and to each artificial neuron is associated a term of bias. It worth noting that the actual processing of the information happens in the hidden and output layers of the network.

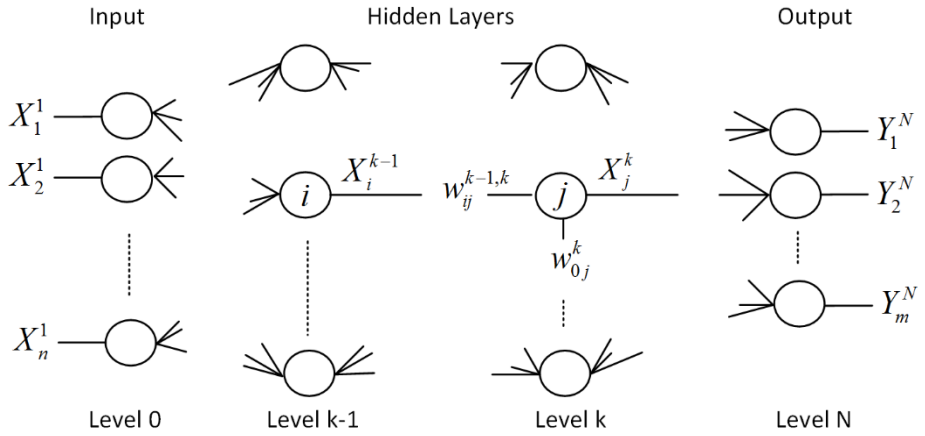

Figure 6.2. Representation of a multi-layer feed-forward ANN architecture composed by an input layer, an output layer, and (N-1) hidden layers.

In order to better understand how the signal propagates within the network, Figure 6.2 will be analyzed in more detail. Each node *j*, that belongs to the level *k*, receives a number N_j of inputs. Each input corresponds to the output X_i^{k-1} of a generic node *i* that belongs to the previous layer ($k - 1$). Moreover, each connection between the generic node *i* of the layer ($k - 1$) and the node *j* of the layer *k* is multiplied by the weight $w_{ij}^{k-1,k}$ that is uniquely associated to the connection. At last, the term of bias is identified by the constant w_{0j}^k. Therefore, when an input $\overline{X} = (X_1^1, X_2^1, ..., X_n^1)$ is applied, it crosses each layer of the network and changes the output of each artificial neuron in proportion to the strength of the connections between the nodes and the intensity of the input itself.

As reported in Equation 6.3, the output of the artificial neuron *j*, belonging to the level *k*, is computed by applying the activation function *f* to the weighted sum of the inputs.

$$X_j^k = f\left(\sum_{i=1}^{N_j} w_{ij}^{k-1,k} X_i^{k-1} + w_{0j}^k\right) \tag{6.3}$$

Generally, the number of degrees of freedom for designing an artificial neural network is relatively high. This allows to accurately choose the architecture that best satisfies the necessities of the problem to solve. Among the characteristics that can be varied there are the number of hidden layers, the number of nodes belonging to

each layer, the connections, and the activation functions. Of course, the number of nodes for characterize the input and output layers depends on the nature of the problem itself. Differently, the number of nodes for the hidden layers is not obvious. However, in literature there are analytical studies that provide indications in reference to such a problem [99].

6.6. Training and Test Operations

The training phase is necessary in order to form the network for solving a given problem. During such a process, the ANN modifies the weights and the bias of all its connections and artificial neurons with the aim to get closer to the desired behavior. Mainly, there are two different and distinct procedures of training: namely the supervised learning process and the unsupervised learning process.

In the supervised learning process, the ANN is trained using a set of examples—the so-called training-set—consisting of several input-output pairs. The examples must be significant in order to well characterize the problem for which the network is designed to cope with. During this forming phase, for all the input-output pairs the ANN iteratively adjusts the weights and bias with the aim to decrease the errors between the desired outputs—the targets—and the current ones—reconstructed by the network.

Differently, in the unsupervised learning process, also known as self-learning, only the inputs are provided to the ANN. In this way, the regulation of both the weights and bias is obtained by searching for any regularities on the input signals. Such a training process is based on the assumption that the network has the abilities of to organize and adapt itself to the inputs received. Of course, this process requires long times of signal processing.

Once completed the training phase, all the weights and bias are stored and the network is ready to be used in the next phases of test and operating mode. The test phase consists of assessing both the performance and capabilities of the network by testing it with several generic examples that were not used during the previous training phase. Al last, the phase of operating mode consists of testing the network in “on-field” applications by means of actual measurements obtained for the particular application that is considered.

7. Appendix B — Realistic Model-Based Skin-Artifact Removal Technique for UWB Radar Breast Cancer Detection Techniques

7.1. Introduction

As previously mentioned in the Chapters of this Ph.D. thesis, the desire of having new non-invasive detection techniques for diagnosis breast cancer during its early stage of development, and with high values of sensitivity and specificity, has motivated several groups of research around the world to investigate new diagnostic techniques. Among several proposals, the development of the microwave imaging techniques was driven by the existing contrast between the electromagnetic properties of the malignant and healthy breast tissues. Among the active approaches, the two most promising alternatives are the microwave tomography techniques, previously described in Section 3.3.2, and the UWB radar imaging techniques, described in Section 3.3.1.

The UWB radar imaging techniques are aimed at providing a qualitative image of the breast that describes the presence and location of the main dielectric scatterers. These techniques use a mono-static or multi-static radar system configuration to illuminate the breast—through UWB pulses with central frequencies in microwave band—and then measure the backscattered radar signals. The breast image is obtained by processing the recorded signals through a time-domain image-formation algorithm, the so-called beamforming algorithm.

A serious and challenging issue concerning the UWB radar imaging techniques is related to the fact that the received signals contain not only the reflections due to the presence of both the malignant and healthy internal breast tissues, but also those

backscattered from the interfaces air/skin and skin/adipose tissue, the so-called skin-artifact component [7]. This last is a predominant component because it is several orders of magnitude greater than the others and, since it overlaps with the reflections backscattered from the internal tissues, it can mask the presence of tumors because [7, 8, 9, 10]. For the UWB radar imaging techniques, one of the most critical aspects, representing a hard and fundamental challenge to overcome, is the implementation of a reliable and accurate skin-artifact removal algorithm that suppresses the strong skin reflections without introducing any distortion on the signal of interest.

Several skin-artifact removal algorithms were proposed in literature. Some approaches are based on the assumption that the skin-artifact can be estimated and removed by creating a suitable reference waveform. Typically, these reference cleaning signals are obtained by averaging the radar signals that are collected at other elements of the antenna array system. Then, the skin-artifact is removed by subtracting, from each recorded radar signal, the appropriate reference waveform. Some algorithms that were proposed following this approach are the average subtraction [94], and the rotation subtraction [60]. In the average subtraction algorithm, a unique reference cleaning signal is estimated, and used for all the channels, by averaging the radar signals measured at all the elements of the antenna array. Differently, with the rotation subtraction approach, a different skin-artifact waveform-consisting of the radar signal measured at another antenna that is distant a number of established positions from the considered channel-is estimated for each element of the array. However, an approach of this type suffers of problems and limitations because it does not take into account of the variations between artifacts that are perceived at different antenna positions, where these last are caused by local variations in the skin thickness, breast heterogeneity, and distance between the skin and the antenna.

To overcome these problems, some adaptive filtering algorithms—such as the Wiener filter [100] and the recursive least squares filter [101]—were proposed with the aim to improve the performance by limiting the effects caused by the artifact's variations. Using an approach of this type, the artifact component is estimated, for each channel, as a filtered and weighted combination of the radar signals measured in the others antennas. In this contest, the substantial difference, among the two approaches above mentioned, consists of the weights computation. In the Wiener filter the weights are obtained by minimizing a residual signal mean-squared error over a time window that corresponds to the portion of the signal where the artifact component is stronger. In this way, at each iteration, the obtained weight vector is shifted over the selected window. In contrast, using the recursive least squares filter method, the weight vector is computed and updated at each iteration.

Moreover, other proposals of skin-artifact removal techniques are the entropy based time window [8], the frequency domain pole splitting [9], and the singular value decomposition [102]. The entropy based time window approach is based on the assumption that, comparing the radar signals measured at different elements of the antenna array, the various artifact components are similar among them, whereas the tumor's signature is attenuated and delayed in a different way. Since the Entropy function is inversely proportional to the amount of variation, it can be used to measure the variation on the collected radar signals. In this way, higher values are obtained on the portion of the signal that contains the artifacts, whereas smaller values are provided where the tumor's signature is present. Using such an approach, a time window is built using the entropy values, then the cleaned signals are obtained by multiplying the window for each radar signal. In contrast, the frequency domain pole splitting approach is focused on describing the frequency response of each radar signal as a sum of complex exponentials. Assuming that each of the obtained exponentials corresponds to a specific scatterer viewed by the antenna, the artifact component is removed by suppressing the strongest pole, namely the one that corresponds to the strongest scatterers. At last, the singular value decomposition approach is aimed to subdivide the space of all the backscattered radar signals into two different subspaces, namely the artifact subspace and the tumor one. In conclusion, the suppressing operation is applied by selecting only the tumor subspace.

The performance of these skin-artifact suppression algorithms was studied and assessed in [103]. The obtained results show that the average subtraction and the rotation subtraction algorithms are not reliable to be used in realistic cases, namely where there are local variations in skin thickness, breast heterogeneity, and antenna-skin distances. On the other hand, the other proposed methods—consisting of the recursive least squares filter, the frequency domain pole splitting, and the singular value decomposition—tend to provide a non-accurate cleaning process, because too much distortions are introduced on the tumor response. According to [103], it seems to be that the best results are provided by Wiener filter and entropy based time window algorithms. However, even these approach is not able to completely suppress the skin-artifact component without introducing any distortion on the tumor's signature.

For these reasons, this appendix proposes and assesses a new skin-artifact removal technique able to face the problem of the artifact suppression without assuming any a-priori information on the structure of the examined breast. Since the tumor's signature is overlapped with the reflections of the other healthy breast tissues, where all these components are hidden by the strong skin reflections, the proposed approach is designed to work only with the aim of removing the skin artifact and, at the same

time, minimizing the changes and distortions that are introduced on the components backscattered from the breast internal tissues independently by their benign or malignant nature. To this end, the proposed approach is based on the use of a two-layered reference cleaning model characterized by suitable both geometric and dielectric parameters. For each channel, the reference cleaning signal is computed and then subtracted, from the total backscattered one, in order to obtain the cleaned signal.

In the following, this appendix presents a first section that describes the main differences between the cleaning techniques that are aimed to remove the artifacts components generated from both the skin and internal healthy tissues, and the cleaning techniques that are aimed to remove only the skin-artifact component. On the basis of these differences, some suitable characteristics of the cleaned radar signals will be observed and commented. These characteristics will be used in order to assess the performance of the proposed technique.

Furthermore, another section will be devoted on both the design and assessment of the best geometric and dielectric configurations of the reference cleaning model. Once found the suitable configurations, a further section will be focused on the validation of the proposed cleaning technique. To this aim it will be tested using the breast cancer radar detection method, that is based on the use of artificial neural networks, proposed and studied in the chapters of this Ph.D. thesis. In particular, in this section different configuration modalities of the reference cleaning model—obtained by using different parameter values for its dielectric characterization—will be considered and tested on the ANN-based diagnostic technique.

7.2. Breast Geometries and Simulation System

As described in Section 4.2.1, assuming the case where the patient is outstretched on the prone position, the measurement system consists of a mono-static radar system that collects the radar signals in different points of the space. The T_x/R_x antenna is designed free to move along a circumference around the breast and at different distances from the thoracic case.

In order to characterize different healthy breasts, two-dimensional (2D) realistic breast geometries were used. These last were derived from the realistic three-dimensional (3D) breast phantoms provided by the UWCEM database [6], and previously described in Section 3.3.1.1. Each model distinguishes and characterizes eight different healthy tissues: the skin, three typologies of adipose tissue, a transitional tissue, and three typologies of fibro-glandular tissue.

As described in Section 4.2.1, 2D healthy geometry was built in random manner by randomly choosing the UWCEM model, the cross-section, and the Debye parameters (ε_s, ε_∞, σ, τ) for each typology of healthy internal tissue.

The cancerous geometries were built starting by new 2D healthy geometries in which a tumor was inserted. This last was modeled as a circular dielectric anomaly characterized by different dimensions, namely different diameters randomly chosen between 0.2 cm and 1 cm. Even the position was defined in a random way by randomly choosing a depth between the outer surface of the skin and the center of the probing line. In order to dielectrically characterize the tumor, the values of the Debye parameters were obtained, from the Cole-Cole representation provided in [33], by minimizing the cost function proposed by [32]. In conclusion, the tumor has been dielectrically characterized with an ε_s of 61.6, ε_∞ of 14.5, σ of 0.7 S/m, and a τ of 13 ps

The measures of the backscattered radar signals are obtained through simulation using the finite-difference time-domain (FDTD)-based software GprMax. [93]. At last, for each mono-static radar antenna position, the breast geometry was illuminated using an UWB pulse, consisting of a differentiated Gaussian pulse (DGP) of central frequency 2 GHz and time duration 1 ns.

7.3. Ideal Skin Artifact Removal Techniques

As mentioned in the previous sections, a serious problem for all the UWB radar imaging techniques is related to the presence of the skin-artifact component inside the measures of the backscattered radar signals, namely the presence of the pulses backscattered from the interfaces air/skin and skin/adipose tissue. This issue rises from the natural and intrinsic predominance of such a component with respect to the pulses backscattered from both the healthy and malignant breast tissues. Moreover, the skin reflections are several orders of magnitude greater than the other components, and they overlap with them. Even if different skin-artifact suppression algorithms were proposed in literature, most of the radar signal processing and beamforming algorithms are preliminarily studied and assessed in the case where an ideal cleaning techniques is applied [7].

According with [7], the most common used ideal cleaning technique— hereafter called Ideal-1—is founded on a totally ideal approach, namely on the hypothesis of knowing the actual external shape of the skin, the actual structure of all the healthy breast tissues, and the actual dielectric characterization of both the skin and healthy internal breast tissues.

In fact, for each channel, the ideally cleaned signal is obtained by subtracting, from the total backscattered radar signal that is measured on a cancerous geometry, the radar signal measured on the same breast geometry but in absence of the tumor. Because it is focused on removing, besides the skin-artifact component, even all the components that derive from the heterogeneity of the internal breast tissues, such a totally ideal cleaning technique is aimed at providing the scattering that is related only to the presence of the tumor. Of course, a technique such as Ideal-1 is not realizable in the actual real-life, and it is used only with the aim to preliminarily validate the performance of the radar signal processing and beamforming algorithms.

In contrast, another way is using a partially ideal technique—hereafter called Ideal-2—based on the assumption of knowing only the real external shape of the skin, and the real dielectric characterization of both the skin and adipose tissues. Such an approach is based on the use of a two-layered cleaning model having the same shape of the corresponding actual breast model and characterized by the presence of only the skin and a homogeneous adipose tissue, where these last have the same dielectric characterization of the corresponding real model. For each channel, the ideally cleaned radar signal is obtained by subtracting, from the total backscattered one, the radar signal that is measured on the two-layered cleaning model. A technique like Ideal-2 is aimed to remove only the skin-artifact component independently by the degree of heterogeneity of the internal breast tissues.

As examples, Figures 7.1, 7.2, and 7.3 show a study on the differences obtained by applying the cleaning techniques Ideal-1 and Ideal-2. The radar signals were measured using a 2D geometry in which a dielectric anomaly was positioned at different depths from the outer skin surface. Hereafter, the signal cleaned using the technique Ideal-1 will be referred as Cleaned-1, whereas the signal cleaned using Ideal-2 will be called Cleaned-2.

In particular, for each figure, the signal (a) represents to the total backscattered signal measured on the 2D realistic cancerous geometry, the signal (b) corresponds to the signal Cleaned-1, and (c) represent the signal Cleaned-2. In Figure 7.1, the two cleaning techniques are assessed in the case where the dielectric anomaly is positioned outside the fibro-glandular tissue. In Figure 7.2 the two techniques are compared in the case where the outer surface of the anomaly is positioned on the outer surface of the fibro-glandular tissue. At last, Figure 7.3 represents the case where the dielectric anomaly is located deep inside the fibro-glandular tissue.

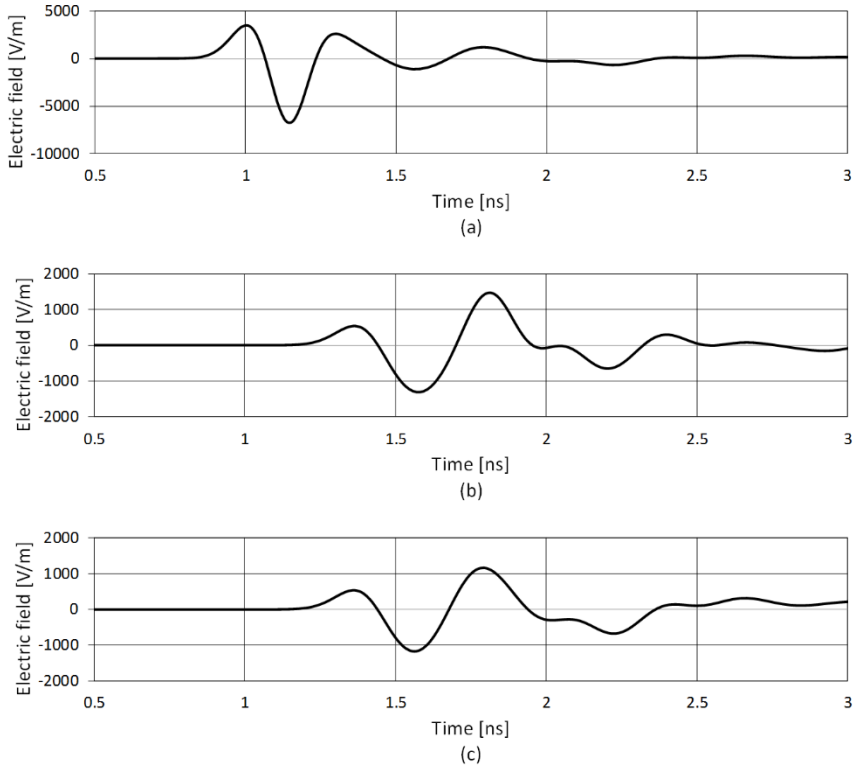

Figure 7.1. The cleaning techniques Ideal-1 and Ideal-2 compared in the case where the dielectric anomaly is positioned outside the fibro-glandular tissue. (a) Total backscattered radar signal; (b) signal Cleaned-1 obtained using the cleaning technique Ideal-1; (c) signal Cleaned-2 obtained using the cleaning technique Ideal-2.

Looking at Figure 7.1(b) and Figure 7.1(c), it is evident that in the case where the tumor is positioned outside the fibro-glandular tissues, the first peaks of the signals Cleaned-1 and Cleaned-2 are identical, whereas the tails show only negligible differences. From this first analysis, it is possible to conclude that both the first and second cleaning technique produces the same effects. In contrast, looking at Figure 7.2, the first peaks of the cleaned radar signals appear much different from each other respecting to the case reported in the previous Figure 7.1, and the diversities between the two cleaning techniques start to appear more evident. As matter of fact, since the technique Ideal-1 is aimed to remove all the artifacts that exist before, around, and then the tumor's signature, it affects all the radar signal. Differently, since the technique Ideal-2 is aimed to suppress only the reflections of the skin artifact component, it tends to operate only on the first part of the radar signal.

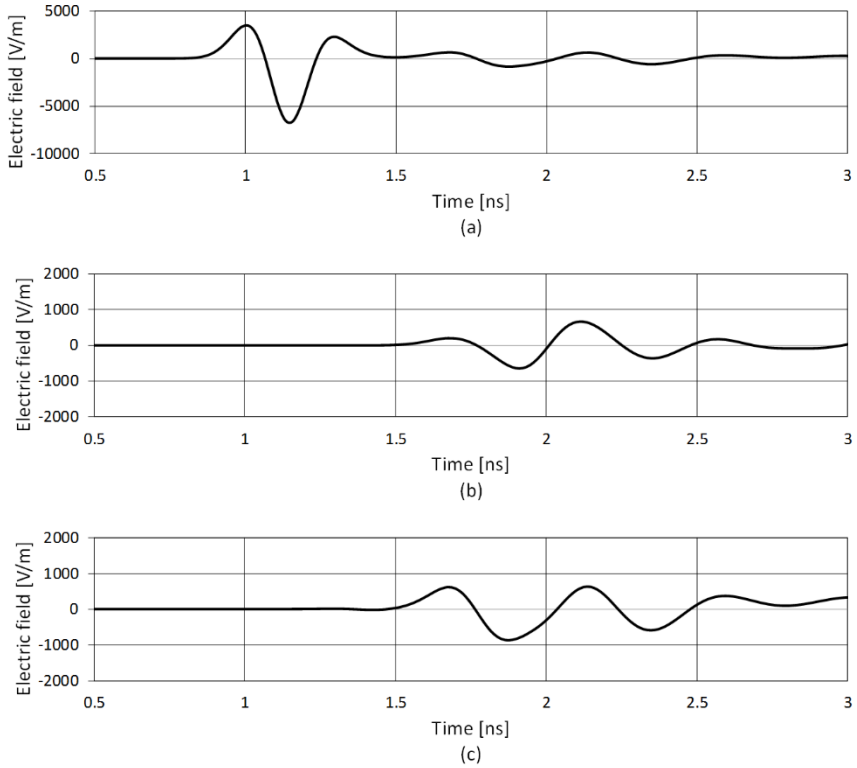

Figure 7.2. The cleaning techniques in the case where the dielectric anomaly is positioned inside the fibro-glandular tissue and closely near to its outer surface. (a) Total backscattered radar signal; (b) signal Cleaned-1; (c) signal Cleaned-2.

The previous considerations appear more evident in the case of deep internal tumors. Comparing Figure 7.3(b) with Figure 7.3(c), it is evident that the signals Cleaned-1 and Cleaned-2 They present diversities not only in terms of both waveform shapes and amplitudes, but also in terms of arrival times. The most obvious reasons are related to the fact that, since the signal Cleaned-1 contains only the tumor's signature together with all the contributions due only to the "history" of the electromagnetic interaction between the tumor and other internal tissues, the time of arrival mainly depends by the tumor position, where more the tumor is deep and more the arrival time is greater. Differently, since the cleaning technique Ideal-2 is aimed to suppress only the skin-artifact component, the reflections backscattered from the internal healthy tissues are present with greater effects inside the signal Cleaned-2. For these reasons, the time of arrival strongly depends by the shape and disposition of the fibro-glandular tissues.

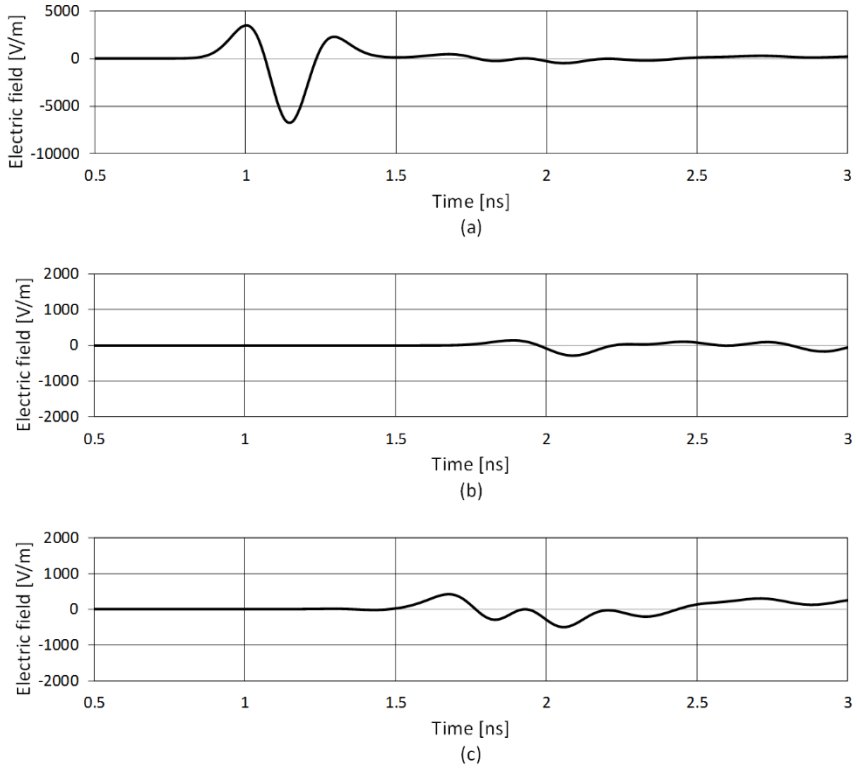

Figure 7.3. Case where the dielectric anomaly is positioned deep inside the fibro-glandular tissue. (a) Total backscattered radar signal; (b) signal Cleaned-1; (c) signal Cleaned-2.

However, looking at Figure 7.3, also inside the signal Cleaned-2 it is possible to identify a signature that identifies the tumor presence. Comparing Figure 7.3(b) with Figure 7.3(c), it is evident that, at the same time—equals to approximatively 1.9 ns—that corresponds to the arrival time of the tumor reflection detected in the signal Cleaned-1, the signal Cleaned-2 exposes a signature that is univocally connected with the tumor presence.

From these analyses some useful conclusions can be deduced. The cleaning technique Ideal-1 is a totally ideal technique aimed to remove the artifacts due to the presence of both the skin and internal healthy tissues in order to obtain a signal in which only the components due to the tumor and the history of its interactions with the internal tissues are present. On the other hand, the cleaning technique Ideal-2 is an ideal technique focused to suppress only the skin-artifact component.

For this reason, it goes to alter only the first part of the signal without modifying the reflections due to the internal tissues independently of their benign or malignant nature.

In the present appendix, the main aim is to develop a standard way to implement the technique Ideal-2 without the a-priori assumption of knowing the actual shape of the skin, and the real values of the dielectric parameters that characterize both the skin and the adipose tissues. Because, from the previous analyses, it was demonstrated that the technique Ideal-2 goes to modify only the first part of the radar signal, the present study—aimed to find a possible realistic implementation—will be based on comparing the first part of the radar signals cleaned respectively using the technique Ideal-2 and the proposed realistic one. To this aim, some error indexes—built on the firsts two maxima/minima of the cleaned radar signals—will be considered in order to quantify the differences that derive from the application of the two cleaning approaches.

7.4. Model-Based Skin Artifact Removal Technique

The main goal of this section is to develop a practical implementation method in order to suppress the skin-artifact component without assuming a-priori information on the actual structure of the breast geometries. To this end, the proposed approach consists of using a reference cleaning model composed by a two-layered cylinder, representing the skin and a homogeneous adipose tissue. This reference model is characterized by suitable dielectric Debye parameters that describe the two tissues. Moreover, other important parameters are: the skin thickness, the diameter dimension, and the distance between the outer skin surface and the radar antenna, namely the position where the reference model is placed with respect to the position of the antenna. In this way, the suitable configuration of the reference cleaning model is used to simulate the reference cleaning signal that is subtracted from the total real one in order to obtain the cleaned signal.

7.4.1. Error Indexes Used to Configure the Reference Cleaning Model

In the previous sections it has been showed that a cleaning technique like Ideal-2 affects only the first part of the radar signal because it is aimed to remove only the reflections backscattered from the skin, without modify the components due to the internal healthy tissues.

For this reason, in order to configure the proposed two-layered reference model, the analyses were based on comparing the first two maxima/minima measured on the same radar signals cleaned respectively using the ideal technique Ideal-2 and the proposed model-based one. To this end, the following four error indexes—built on the amplitudes and arrival times of the firsts two peaks—were considered.

$$\begin{cases} Ia_i = 100\left|\dfrac{A_{real}(i) - A_{ideal}(i)}{A_{ideal}(i)}\right| \\ \\ It_i = \left|t_{real}(i) - t_{ideal}(i)\right| \end{cases} \qquad i = 1,2; \tag{7.1}$$

Where $A_{real}(i)$ and $t_{real}(i)$ represent respectively the amplitude and the arrival time of the i^{th} maximum/minimum of the radar signal cleaned using the proposed reference cleaning model; $A_{ideal}(i)$ and $t_{ideal}(i)$ are the amplitude and the arrival time of the i^{th} peak measured on the radar signal cleaned with the technique Ideal-2.

In order to study the error indexes on a suitable and significant scenario, three different realistic 2D healthy breast models—hereafter called $Model_1$, $Model_2$, and $Model_3$—were considered. These models were chosen different each from other in terms of dimensions, heterogeneity, and dielectric characterization.

For each of these healthy breast geometries, the error indexes were studied in three different situations: in the case where a tumor is located deep inside the fibro-glandular tissues (T_{int}); when a tumor is located outside the fibro-glandular tissues (T_{ext}); in absence of the tumor (NT).

All the simulated healthy and cancerous breast geometries are reported in Figure 7.4, where: Figures 7.4(a), 7.4(b), and 7.4(c) show the cases where the tumor is positioned deep inside the fibro-glandular tissues; Figures 7.4(d), 7.4(e), and 7.4(f) show the same breast models but in the case where the tumor is inserted outside the fibro-glandular tissues; and Figures 7.4(g), 7.4(h), and 7.4(i) show the breast geometries in absence of the tumor.

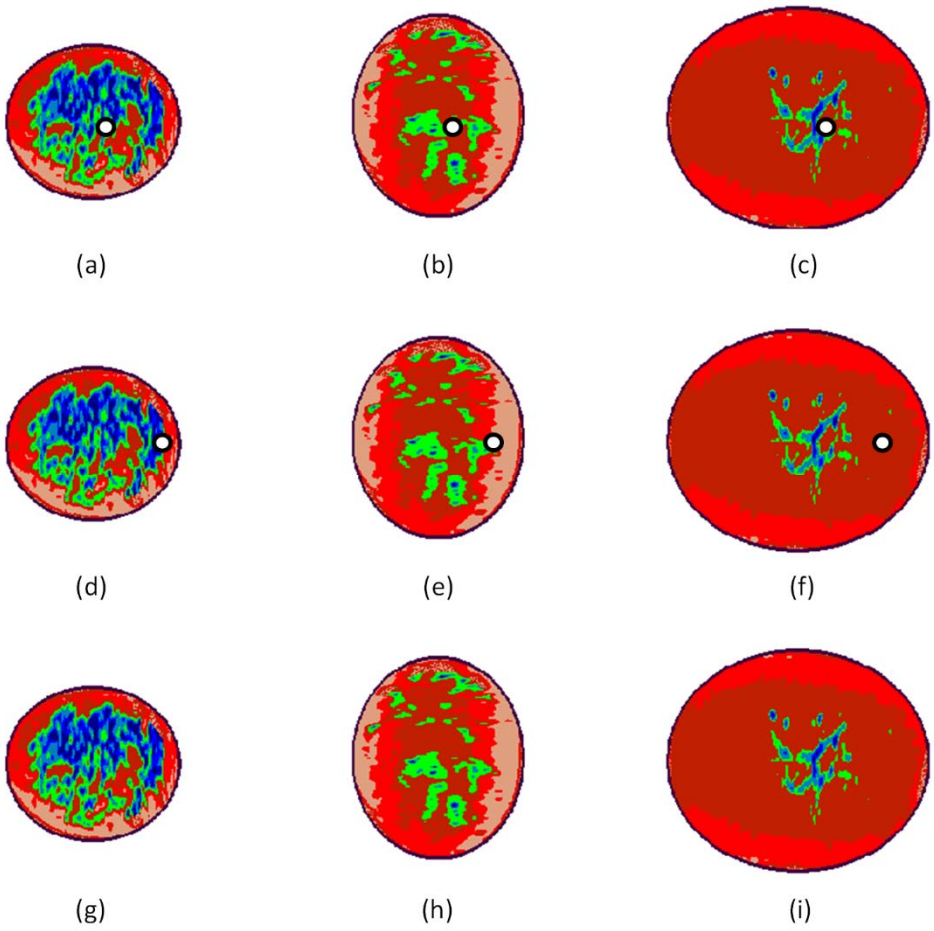

Figure 7.4. Breast geometries used to configure the reference cleaning model on the basis of the analyses of the error indexes. (a) $Model_1$-T_{int}; (b) $Model_2$-T_{int}; (c) $Model_3$-T_{int}; (d) $Model_1$-T_{ext}; (e) $Model_2$-T_{ext}; (f) $Model_3$-T_{ext}; (g) $Model_1$-NT; (h) $Model_2$-NT; (i) $Model_3$-NT.

7.4.2. Geometric Configuration

This section is focused on configuring the dimension and distance of the reference cleaning model by searching for the best compromise on the obtained values of the error indexes. In this context, for each of the nine realistic breast models previously described and showed in Figure 7.4, two-layered reference cleaning models—characterized by the same Debye dielectric parameters for both the skin and adipose tissue, and the same skin thickness of the corresponding real model—were considered.

First, considering the case where the reference cleaning model is positioned at the real distance—namely the same of the corresponding realistic breast model—an analysis at varying the model dimension was performed. In particular, the radius dimension was varied between the range of 5 cm and 40 cm with step of 1cm.

The obtained results showed that, for the six NT and T_{int} cases, the error indexes Ia_1, Ia_2, It_1, and It_2, were always lower or equal respectively than 2.01 %, 1.10 %, 2.25 ps, and 1.18 ps. In contrast, as shown in Figure 7.5, for the T_{ext} cases the variations were more significant. In particular, Figure 7.5 reports four graphics that show the variations of the four error indexes obtained for the T_{ext} cases. Indeed, each graph reports three curves that correspond to the three different models $Model_1$-T_{ext}, $Model_2$-T_{ext}, and $Model_3$-T_{ext}. Looking at the graphs shown in Figure 7.5, it is evident that even in this cases the error indexes Ia_2, It_1, and It_2 have negligible values. whereas significant error values—reaching the 30 %—are observed for the error index Ia_1.

According with the above considerations, searching for the radius dimension that minimizes the value of Ia_1, it is possible to conclude that an acceptable situation appears in the case where a radius of 11 cm is used. Using such a configuration of the reference cleaning model, the values obtained for all the four error indexes are reported in Table 7.1.

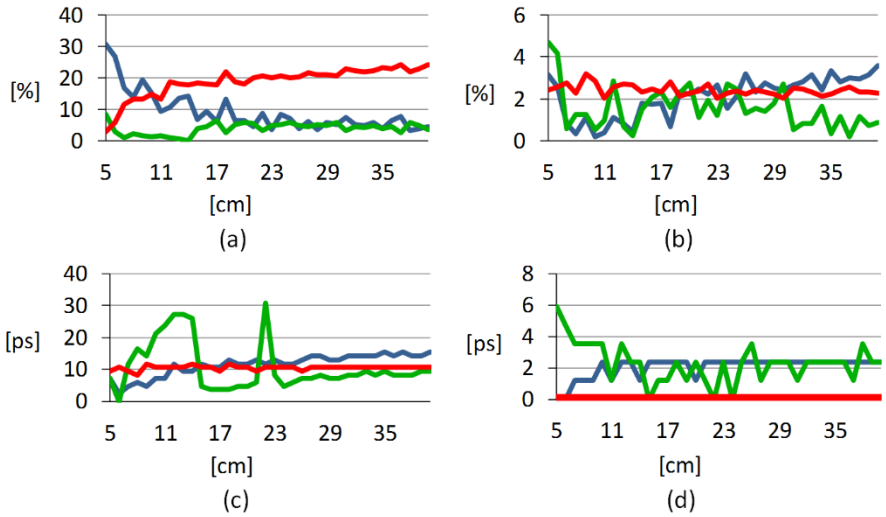

Figure 7.5. Error indexes obtained at varying of the radius dimension of the reference cleaning model, and computed using the realistic cancerous models $Model_1$-T_{ext} (blue lines), $Model_2$-T_{ext} (green lines), and $Model_3$-T_{ext} (red lines). (a) Ia_1; (b) Ia_2; (c) It_1; (d) It_2.

Table 7.1. Error indexes obtained in the case where the reference cleaning model of radius 11 cm is positioned at the same realistic distance as in the real breast models.

Breast Models	Error Indexes			
	Ia*$_1$ *(%)	***Ia*$_2$ *(%)***	***It*$_1$ *(ps)***	***It*$_2$ *(ps)***
Model$_1$-NT	0.60	0.01	0.00	0.01
Model$_2$-NT	0.27	0.24	8.26	1.18
Model$_3$-NT	0.46	0.59	1.18	0.00
Model$_1$-T$_{int}$	0.65	0.01	0.01	0.00
Model$_2$-T$_{int}$	0.25	0.26	8.24	1.19
Model$_3$-T$_{int}$	0.43	0.57	1.16	0.00
Model$_1$-T$_{ext}$	9,33	0.39	7.08	1.18
Model$_2$-T$_{ext}$	1.74	0.97	23.59	1.18
Model$_3$-T$_{ext}$	13.23	2.06	10.61	0.00

Once found the best compromise on the model dimension, using such a case, the error indexes were studied at varying of the distance between the reference cleaning model and the radar antenna. This analysis highlighted that, for all the cases here studied, the knowledge of the real distance is required. Indeed, if an error of only ±1cm is introduced on the distance, the average variations observed on the error indexes and computed on all the nine models, demonstrate error increments equal to: 8.70 % on Ia$_1$; 1.10 % on Ia$_2$; 2.70-ps It$_1$; 0.40-ps It$_2$.

In conclusion, on the basis of the assessment of the variations of the error indexes, the best results were obtained in the case where a reference cleaning model—with 11-cm radius—is used by placing it at the same real distance that exists between the skin and the antenna. It is worth noting that, since the proposed technique is based on the use of a mono-static radar system, the computation of the real distance does not represent a challenging task also in real-life.

7.4.3. Dielectric Characterization and Skin Thickness

In order to dielectrically configure the reference cleaning model, this section presents a study on how the skin thickness and each single Debye parameter (ε_s, ε_∞, and σ) for the dielectric characterization of both the skin and adipose tissues affect the value of the error indexes. As mentioned in the previous section, Table 7.1 shows the

values of Ia_1, Ia_2, It_1, and It_2 in the case where the total backscattered signals are cleaned using a reference cleaning model with the actual skin thickness and the actual Debye dielectric characteristics of the corresponding real breast models. In this context, the values reported in Table 7.1 were used as reference values, and the differences introduced by varying each single parameter one at time have been studied.

First, the importance of knowing the real values of all the parameters that dielectrically characterize both the skin and adipose tissue was studied. To this end, the three Debye parameters ε_s, ε_∞, and σ were varied, one at time, between the ±10% of their real values. Then, the averages on the maximum variations that were introduced on the error indexes were computed on the three real models. These values are reported in Table 7.2. Looking at this table, it is evident that the dielectric parameters of those the knowledge of the actual values is fundamental are the ε_s of the skin and the ε_s of the adipose tissue.

Table 7.2. Average values of the maximum increments introduced on the error indexes by varying, one at time, the Debye parameters of the skin and the adipose tissue.

Breast Tissues	**Debye Parameters**	**Error Indexes**			
		Ia_1 (%)	***Ia_2 (%)***	***It_1 (ps)***	***It_2 (ps)***
Adipose	ε_s	24.76	6.24	8.65	3.93
	ε_∞	2.53	0.81	5.07	0.01
	σ	6.58	1.87	6.52	0.08
Skin	ε_s	12.03	3.49	7.08	1.97
	ε_∞	1.33	0.35	2.75	0.00
	σ	5.68	0.56	3.15	0.39

At last, in order to assess the importance of knowing of the real value of the skin thickness, different cleaning models characterized by different skin thicknesses were studied. It is worth noting that, for the real models—$Model_1$, $Model_2$, and $Model_3$—the real actual of the skin thickness is 1.5 mm. For these reason, the skin thickness values of the reference cleaning model were varied between 1 mm and 2 mm.

The averages on the maximum variations introduced on the error indexes, and computed on the three real models, were: 28.85 % on Ia_1; 8.75 % on Ia_2; 16.12-ps It_1; and 0.00-ps It_2. Looking at these results, it is evident that it is particularly important to know the actual value of the skin thickness.

In conclusion, on the basis of the assessment studies conducted on the variations of the error indexes, the obtained results show that it is fundamental to assume the a-priori knowledge of at least the real values of the ε_s of the skin, the ε_s of the adipose tissue, and the skin thickness.

7.4.4. Validation of the Proposed Skin-Artifact Removal Technique

In this section, the proposed skin-artifact component suppression technique is tested in case where its cleaned data are processed using the ANN-based breast cancer radar detection technique previously designed and presented in Chapter 3 of the present Ph.D. thesis.

In the previous sections of this appendix, it was concluded that, on the basis of the analyses of the error indexes, the best results are obtained under the a-priori assumption of knowing the real values of the skin thickness and the ε_s of both the skin and adipose tissue. Nevertheless, in this section the proposed cleaning technique is tested using different configuration modalities of the reference cleaning model, consisting of the use of different dielectric characterizations.

In particular, the following cases were considered: when the real values of the skin thickness and all the Debye dielectric parameters of both the skin and adipose tissue are known; when only the real values of the skin thickness and the ε_s of both the skin and adipose tissue are assumed known; when only the skin thickness is known and all the Debye dielectric parameters are fixed at an average standard value. At last, with the aim to assess the results in a more comprehensive also, the case where the technique Ideal-2 is applied was considered.

Section 4.2.4 described the concept under which, if a tumor is located outside the fibro-glandular tissue—T_{ext}—then its signature is contained in the first part of the cleaned radar signal, whereas, if a tumor is located deep inside the fibro-glandular tissue—T_{int}—then its signature is contained in the second part of the cleaned signal.

Therefore, since the proposed cleaning technique is aimed on removing the skin-artifact component and it affects mainly the first part of the radar signal, in order to assess the performance of the different reference cleaning model configurations, the analyses were focused on cases of tumors located outside the fibro-glandular tissue, representing the situations where the tumor presence is mostly masked by the skin presence.

In this context, different networks were trained and tested using the ANN architecture 4-8-1 described and used in the previous Section 4.3.1.

As before described, this ANN architecture has an input layer of four nodes, a hidden layer of eight nodes, and an output layer of one node that provides an output of type Yes/No, depending on the presence or absence of the tumor. Moreover, such an architecture receives four input data, consisting of the amplitudes and the arrival times of the firsts two maxima/minima measured on the cleaned signals.

Following the random manner previously described in the Section 2, 100 realistic 2D cancerous geometries (T) and 100 realistic 2D healthy geometries (NT) were generated. For the purpose to train the networks, 50 T models and 50 NT models were used. The remaining 50 T and 50 NT geometries were used for test the networks. In particular, four different networks were formed using, for each of these, one of the four different cleaning model configuration previously described. Hereafter the four different ANN will be referred as ANN_1, ANN_2, ANN_3, and ANN_4, where:

a) ANN_1 is the network trained using the radar signals cleaned using the ideal cleaning technique Ideal-2;
b) ANN_2 is the network trained under the a-priori assumption of knowing all the real values of the skin thickness and all the Debye dielectric parameters that characterize both the skin and adipose tissue;
c) ANN_3 was trained under the assumption of knowing the real values of the skin thickness and the ε_s of both the skin and adipose tissue;
d) ANN_4 was trained in the case where only the skin thickness is known whereas all the Debye parameters that dielectric characterize the skin and the adipose tissue are fixed to average standard value.

Moreover, in the same way the four sets of test data $Test_1$, $Test_2$, $Test_3$, and $Test_4$ were generated.

Table 7.3 reports the values of accuracy obtained in the cases where the different ANNs were tested using the different sets of test data. As expected, the best results—reaching an accuracy of 91%—were obtained in the case where the network ANN_1 was tested using the set $Test_1$, namely the case where the ideal cleaning technique Ideal-2 is used during both the phases of training and test. Unfortunately, this ideal situation does not correspond to what truly happens in the real-life. However, Table 7.3 shows that very good results—achieving an accuracy of 87%—were obtained also under the a-priori assumption of knowing at least the real values of the skin thickness, the ε_s of the skin, and the ε_s of the adipose tissue, namely where the network ANN_1 is tested using the set $Test_3$.

This last result is important because, during the training phase, the assumption of knowing the real values of the parameters that characterize the breast models is acceptable also in the context of an "on-field" actual application. Nevertheless, the more significant result—reaching an accuracy of 84%—was obtained by testing the ANN_4 with the set of test data $Test_4$. Indeed, this means that good values of accuracy can be achieved also in the case where reference cleaning models—made up of standard values for both the geometric and dielectric characterizations—are used during both the training and test phases. It worth noting that the only parameter that was assumed as known is the skin thickness, however all the realistic 2D breast models used during the simulations present a skin thickness of 1.5 mm.

Table 7.3. Accuracy values obtained by testing the different ANNs 4-8-1 (ANN_1, ANN_2, ANN_3, and ANN_4) using different sets of test data ($Test_1$, $Test_2$, $Test_3$, and $Test_4$).

ANNs 4-8-1	**Performance for Different Test Data (%)**			
	Test₁	***Test₂***	***Test₃***	***Test₄***
ANN₁	91	79	87	76
ANN₂		84	86	87
ANN₃			83	79
ANN₄				84

8. Appendix C — EM-Source Through-the-Wall Localization by Using Artificial Neural Networks

8.1. Introduction

In the last decades, the problem of detecting and localizing electromagnetic (EM) sources has received a lot of interest for several applications such as radar systems, global positioning systems (GPS), sonar, radio astronomy, satellite navigation, military applications, and commercial purposes. In this context, indoor detection and localization of EM sources has become an interesting object of study in last years. As example, in [104] a method to locate an EM source, working in the very high-frequency (VHF) band and positioned inside an indoor location, is presented. In addition, in the case of emergency calls, essential information necessary to guide rescuers to the right place is knowing the location accurately. This has made necessary the development of devices and services to detect and locate survivors for their recovery and for the protection of human lives [105, 106].

To find the position of a pulsed EM source, most of the methods existing in the literature are based on the measurements of the time difference of arrival TDOAs or of the direction of arrival (DOA) in different points in space. Some methods are based on using the TDOAs in order to estimate the DOAs, then the source position is obtained through intersection of the DOAs estimated in different places [107, 108]. Differently, other methods only rely on the TDOAs to directly detect the source position [109, 110]. Even though the methods solely based on TDOA have a strong ability to locate single sources, they cannot deal with multiple sources, and they are weak in a multipath environment [111].

In this appendix, the capabilities of a new probing technique, based on use of artificial neural networks (ANNs) to detect and locate an EM source that is located in an indoor environment, are introduced and assessed. As mentioned in [104], for such a class of applications, an important aspect is how to ensure the line of sight between the transmitter antennas and the receiver antennas. In these cases, because of the strong attenuation introduced by the passage of the signal through walls and obstacles, maintaining visibility should be a problem. On one hand, the use of lower frequencies should reduce these attenuations, but on the other hand, it may reduce the resolution's accuracy on the reconstruction of the position. According to [104], the use of EM sources that operate in the VHF band can be a good compromise between lower attenuation and high resolution. In this context, the present appendix introduces a new probing technique based on ANNs to detect and localize a pulsed EM source that is placed behind a wall and radiates UWB pulses at regular time intervals with a central frequency in the VHF band. The main purpose is to study the performances of a method that allows to obtain a good compromise between two principal goals: accuracy in the reconstruction of the source position as high as possible and a probe dimension that is as small as possible.

Because the solution of such a problem is related to the solution of an inverse EM scattering problem, most of the methods that exist in the state of the art that are based on the inversion of the direct mathematical operators or on the minimization of suitable cost functions, require long computation times and a high computational burden. In the proposed method, the resolution of the inverse scattering problem is based on the use of ANNs. This approach provides several advantages, such as short computational times, low computational burden, and the opportunity to reformulate the problem by considering only the few unknowns of interest.

8.2. Localization of EM Source Behind a Wall

The main purpose of this section is to present a new technique, based on the use of a probe comprising a linear array of antennas and on a signal data processing technique developed using an ANN, to detect and locate an EM source positioned behind a wall. To this end, the model represented in Figure 8.1 is considered. On one side of the wall there is an EM source (T_x) and on the other side there is a probe.

The EM source can be located in any position within distances up to 3 meters from the wall, and it radiates UWB pulses at regular time intervals. The probe is formed by a linear array of receiving antennas (R_1, … R_n), each placed at a fixed distance. This sensor moves parallel to the wall and measures the differences on the times of arrival (t_1, …t_n) and on the amplitudes (A_1, … A_n) of the pulses arriving to the

different receivers. The probe should be as small as possible and formed by the smallest number of receiving antennas.

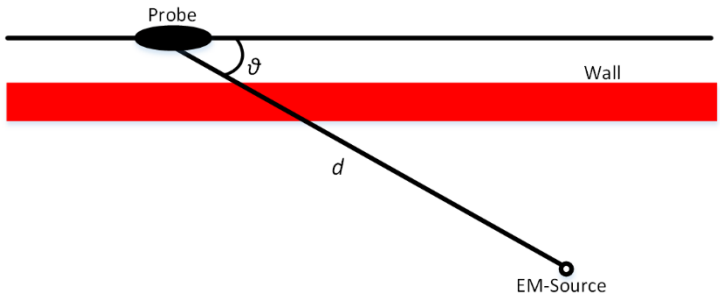

Figure 8.1. Schematic representation of the problem's geometry. There is a wall; on one side there is an EM source and on the other side, there is the probe. For each position of the sensor, the EM source is uniquely identified by the distance '*d*' and the angle '*ϑ*.'

The purpose is to detect the EM source position by providing its distance (d) and direction (ϑ) with respect to the position of the sensor. In order to do this, as it will be better explained in the next sections, once the various times of arrival (t_1, … t_n) and amplitudes (A_1, … A_n) are measured, appropriate data will be used to train an ANN to provide the distance and direction of the EM source.

First, a scenario without a wall is considered where there is an EM source that radiates UWB pulses and a probe formed by 'n' receiving antennas (R_1, … R_i, … R_n), measuring the incident signal. In Figure 8.2, a schematic representation of this situation is shown.

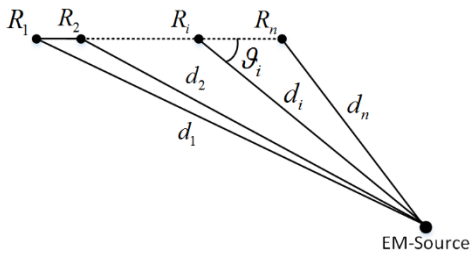

Figure 8.2. Schematic representation of the geometry of the problem with the EM source and the probe positioned in free space. The probe is formed by 'n' receiving antennas. Each i^{th} receiver is positioned at a different distance d_i from the EM source.

Looking at Figure 8.2, the coordinates of the EM source (*x, y, z*) are assumed to be the unknowns of the problem, and each i^{th} receiving antenna, labeled R_i, is positioned in the known coordinates (X_i, Y_i, Z_i).

According with [109], assuming a free space geometry and a spherical wave propagation model, the relations between the positions of each antenna (namely each distance di between the i^{th} receiver and the source) and the differences on the times of arrival (t_1, …t_n) of the pulses arriving to the different receivers can be expressed using Equation 8.1.

$$\begin{cases} d_1 - d_2 = \sqrt{x^2 + y^2 + z^2} - \sqrt{\left(x - \mathrm{X}_2\right)^2 + \left(y - \mathrm{Y}_2\right)^2 + \left(z - \mathrm{Z}_2\right)^2} = cT_{21} \\ \vdots \\ d_1 - d_i = \sqrt{x^2 + y^2 + z^2} - \sqrt{\left(x - \mathrm{X}_i\right)^2 + \left(y - \mathrm{Y}_i\right)^2 + \left(z - \mathrm{Z}_i\right)^2} = cT_{i1} \\ \vdots \\ d_1 - d_n = \sqrt{x^2 + y^2 + z^2} - \sqrt{\left(x - \mathrm{X}_n\right)^2 + \left(y - \mathrm{Y}_n\right)^2 + \left(z - \mathrm{Z}_n\right)^2} = cT_{n1} \end{cases} \quad (8.1)$$

Where: the first antenna R_1 is assumed to be the reference for the computation of the EM source location, and it is positioned in the center of the reference coordinates system; T_{ij} is the TDOA between the receiving receiver *i* and the receiver *j*; *c* is the speed of light (3×10^8 m/s); (X_i, Y_i, Z_i) are the spatial 3D coordinates of the i^{th} antenna; and d_i is the distance between the EM source and the i^{th} antenna.

Under the hypotheses of free space geometry and spherical wave propagation model, and according to Equation 8.1, the signal measured by the i^{th} receiving antenna can be represented by Equation 8.2.

$$S_i(t) = A_i U(t - t_i) = \frac{A_0}{d_i} U(t - t_i) \quad (8.2)$$

Where: $S_i(t)$ is the signal measured by the i^{th} receiver, A_i is its amplitude, $U(t)$ is the waveform of the pulse radiated by the EM source, A_0 is the amplitude of the radiated pulse, d_i is the distance of the i^{th} receiver from the source, and t_i is the arrival time of the pulse.

Moreover, according to Equations 8.1 and 8.2, it is possible to relate the signals measured between adjacent receivers through the following relations:

$$\begin{cases} \Delta t_{i+1,i} = t_{i+1} - t_i = \dfrac{d_{i+1} - d_i}{c} \\ \dfrac{A_i}{A_{i+1}} = \dfrac{d_{i+1}}{d_i} \end{cases} \tag{8.3}$$

By simply inverting Equation 8.3, it is easy to find the position of the EM source for a given position of the sensor. Indeed, in the case, for example, that the antenna R_1 is assumed as reference, the relative position between the source and the probe (namely the distance d and the angle ϑ), can be described as indicated in Equation 8.4.

$$\begin{cases} d = d_1 \\ \vartheta = \vartheta_1 \end{cases} \tag{8.4}$$

Where: d_1 and ϑ_1 are, respectively, the distance and the angle under which the EM source is seen by the receiving antenna R_1 (see Figure 8.2).

Under this hypothesis, it easy to obtain by means of the analytical inversion of Equation 8.3 that the distance and the angle can be written using Equation 8.5.

$$\begin{cases} d = d_1 = \Delta t_{i,1} \left(\dfrac{cA_i}{A_1 - A_i} \right) \\ \vartheta = \vartheta_1 = \dfrac{\left(d_1^2 + \overline{R_i R_1}^2 - d_i^2 \right)}{4 d_1 \overline{R_i R_1}} \end{cases} \tag{8.5}$$

Where: $\overline{R_i R_1}$ represents the distance of the i^{th} antenna R_i from the reference antenna R_1.

However, in presence of obstacles like a wall, the hypothesis of free space and spherical propagation is not satisfied and the equations are no longer valid. Even if, in the presence of the wall, the signal amplitude and time of arrival still depend on

the wave propagation path between the receivers and the EM source, in this real-life case, the propagation path is not the same as the simple Euclidean distance in free space. Moreover, when the wall has a thickness and an electric conductivity that is not negligible, strong attenuations affect the received signals. According to the Snell laws, the direction of propagation changes depending on the angle of incidence. Therefore, the longer the path within the wall, the higher the corruption of the propagation model in terms both of direction and amplitude. For these reasons, the real relations existing between both the amplitudes and times of arrival with the propagation paths are more complex than those reported in Equation 8.2 and consequently in Equation 8.3. Nevertheless, even if these relations are complex, they certainly depend on the relative position between the EM source and the probe, providing the wall characteristics are assumed to be known. In this context, Equation 8.3 can be rewritten as Equation 12.

$$\begin{cases} \Delta t_{i+1,i} = f_{i+1,i}\left(d, \vartheta\right) \\ \dfrac{A_i}{A_{i+1}} = g_{i+1,i}\left(d, \vartheta\right) \end{cases} \tag{8.6}$$

Where: as shown in Figure 8.1, d and ϑ describe the position of the EM source with respect to the position of the probe.

These equations show that the differences on the times of arrival ($\Delta t_{i+1,i}$) and on the amplitude ratios (A_i/A_{i+1}) are functions, respectively, f and g, of the distance d and of the angle ϑ under which the source is viewed by the probe.

Trying to solve the problem represented by Equation 8.6 means solving an inverse electromagnetic scattering problem. As mentioned in the introduction, most of the methods that exist in the literature require not only long computation times and high computational burden, but also knowing the mathematical operators that must be solved.

In the proposed approach, in order to avoid mathematically developing Equation 8.6 and to reduce the computation time to reach quasi real-time response, ANNs are used. In particular, as described in the following sections, an ANN has been built starting with the knowledge of a certain number of "examples" relating the relative position of the probe and source (d and ϑ) to the signal data $\Delta t_{i+1,i}$ and (A_i/A_{i+1}), measured by each receiving antenna constituting the probe.

8.3. Artificial Neural Network Application to the Source Localization

In this section, a new probing technique, based on the use of ANNs to detect and localize a pulsed EM source that is placed behind a wall, is designed and assessed. As mentioned in the previous sections, the main purpose is to study the performance of a method that allows to obtain a good compromise between two principal objectives: an accurate reconstruction of the source position that is as high as possible and a probe dimension that is as small as possible.

To this aim, the case of a probe formed by three receiving antennas (R_1, R_2, R_3) equally spaced 10 cm apart was initially considered. The total width of the sensor is 20 cm, and it moves parallel to the wall with a distance of 50 cm. The three receivers are linearly placed to avoid any geometric ambiguous localization, whereas the distance of 10 cm represents an initial guest to search for an acceptable minimum probe dimension respect to allow, for the given operating central frequency, useful differences on the signals received at the 3 antennas. The EM source has been modeled using a differentiated Gaussian pulse (DGP) of central frequency 300 MHz and time duration 5 ns. A graphic representation of the EM pulse is shown in Figure 8.3. The EM source can be arbitrarily located in any position within a square of area 3×3 m^2 behind the wall. The wall in question is a wet brick wall, with a thickness of 30 cm, a relative dielectric permittivity of 4.0, and a conductivity of 0.2 S/m [112].

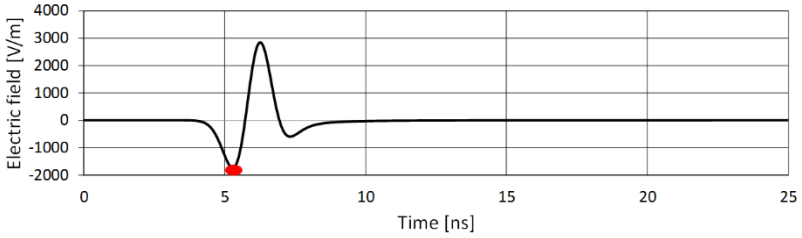

Figure 8.3. Graphic representation of the DGP of central frequency 300 MHz and time duration 5 ns. The position of the first peak at which each receiver antenna measures the amplitude and the time of arrival is marked in red.

Usually, the measurement of the TDOA is a critical operation that requires the implementation of specific techniques that measure the times of arrival (DOAs) at the different receivers or use a cross-correlation technique. In order to reduce these critical issues, in this section, instead to estimate the TDOA by computing the

signals' TOAs or any signal's cross-correlation, the measure of the arrival time of the first peak of the radiated UWB pulse is used. It is worth noting that the principal aim is to assess the performance of the diagnostic technique itself, independently of which technique for the TDOA estimation is implemented. Moreover, because the signal radiated by the EM source is a pulse, measuring the amplitude and the arrival time of this first peak is simpler than measuring the amplitude and the arrival time of the total signal. For these reasons, in this study, the arrival times and the signal amplitudes measured by each receiver are substituted by the arrival times and the amplitudes of the first peak of the UWB pulse measured by each receiver.

Another important aspect is that, to correctly measure the TDOA, synchronization between the transmitter and the receiving antennas is fundamental. In a practical sense, this is achieved simply by waiting for a preliminary time before starting the locating operations. Because the main purpose of this section is to assess the capabilities of the proposed source localization method based on the ANN technique, the synchronization process is assumed to be ideally applied.

As mentioned in the previous sections, the main purpose of the locating technique is to detect the EM source position by providing its distance (d) and direction (ϑ) with respect to the position of the sensor. In Equation 8.6 has been shown that the differences on the TOAs ($\Delta t_{i+1,i}$) and on the amplitude ratios (A_i/A_{i+1}), measured by different receivers, are functions, respectively, f and g, of the distance d and of the angle ϑ under which the EM source is viewed by the probe.

Therefore, because the probe is formed by three receiving antennas, Equation 8.6 furnishes four relations connecting the unknown quantities, d and ϑ, to four known pieces of data—namely, the two differences between the arrival times of the pulse's first peak measured by different receivers ($\Delta t_{2,1}$ and $\Delta t_{3,2}$) and the two ratios between the amplitudes of the pulse's first peak measured by different antennas ((A_1/A_2) and (A_2/A_3)).

Consequently, the ANN used receives four pieces of input data and provides two outputs—namely, the distance d and the angle ϑ referred to the probe position. If examined in more detail, $\Delta t_{2,1}$ is the difference between the arrival times of the first peak measured by the receivers R_2, R_1; $\Delta t_{3,2}$ is the difference between the arrival times of the first peak measured by the receivers R_3, R_2; (A_1/A_2) is the ratio between the amplitudes of the first peak measured, respectively, by the receivers R_1, R_2; and (A_2/A_3) is the ratio between the amplitudes of the first peak measured, respectively, by the receivers R_2, R_3.

As proposed by [99, 112] a good choice is to use a multilayer feed-forward ANN with only one hidden layer. This number of nodes should be twice the number of input data. Therefore, because for the problem considered, four inputs and two

outputs are considered, the ANN that has been developed and used—hereafter called ANN 4-8-2—is formed by an input layer with four nodes, a hidden layer with eight nodes, and an output layer with two nodes. The number of degrees of freedom of the network considered is 56, which is given by the number of unknown parameters, the weights, and the bias, characterizing the ANN (see Appendix A). Indeed, the ANN considered has 4×8 weights connecting the nodes of the input layer with those of the hidden one, 8 bias for each node of the hidden layer, and 8×2 weights connecting the nodes of the hidden layer with those of the output one.

In order to train the network, a grid of different fixed EM source positions inside the square domain of 3×3 m^2 was chosen. Differently, a set of 900 new test positions selected in totally random manner inside the same area were chosen as testing examples. For these examples, all the grid points used during the network training phase have been excluded.

8.3.1. Performance Analysis

The first assessment study has been focused on studying the variation of the accuracy of the EM source position reconstruction by varying the training set dimension—namely, the number of examples used during the training phase. For each different training-set dimension, a different network, using the same ANN architecture (ANN 4-8-2), has been trained and tested. Four different training-set dimensions were considered: four networks have been trained by using, respectively, 57, 76, 109, and 133 items of training data. For the performance assessment, the same set, formed by 900 totally random test examples, has been consistently used.

Figure 8.4 shows the errors on the distance d and on the angle ϑ reconstructed by varying the training set dimensions. Figure 8.4(a) shows the variations of the maximum, minimum, and average relative errors on the distances, whereas the variations of the maximum, minimum, and average absolute errors on the angles are reported in Figure 8.4(b).

Looking at the figure, it is possible to note that when the number of training data inputs increases, the errors tend to decrease. When the ANN is trained with 133 training data inputs, the average percentage error on the distance is 6.1% and the average absolute error on the angle is 0.6 degree(s). The maximum absolute error on the angle is 2.58 degree(s). The maximum percentage error on the distance is not very good, reaching 36.14%, but it is worth noting that the error value is over 30% for only five cases among the 900 random test examples and this seems to be a very valuable result.

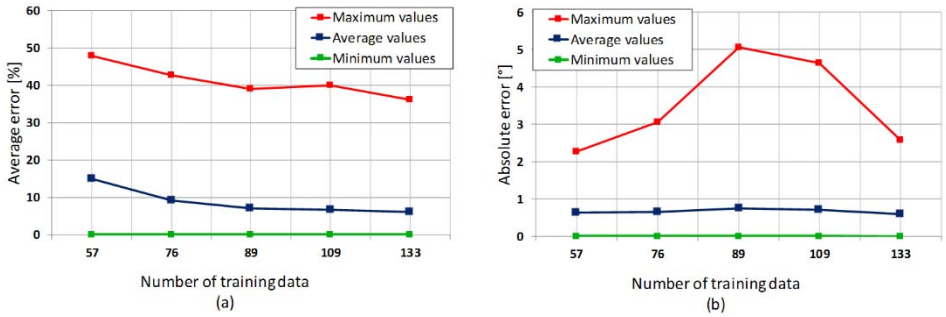

Figure 8.4. Errors by varying the dimensions of the training set. (a) Maximum, average, and minimum relative errors on the reconstruction of the distance *d*. (b) Maximum, average, and minimum absolute errors on the reconstruction of the angle ϑ.

Table 8.1. Maximum, average, and minimum errors on the distance and on the angle for the case of the ANN 4-8-2 trained with 133 training data. The errors are evaluated by using a set of 900 different test examples.

ANN trained with 133 examples	**Error values**		
	Maximum	***Average***	***Minimum***
Relative error on the distance (%)	36.14	6.10	0.005
Absolute error on the angle (°)	2.58	0.60	0.0004

Given these considerations, it seems reasonable to consider the case of the network trained with 133 examples as the better case. The numerical values of the maximum, minimum, and average errors on the distance and on the angle of this situation are reported in Table 8.1.

8.3.2. Optimization Analysis

For the second step, the optimum dimension of the probe was assessed. In order to do this, different sensors, formed by three receiving antennas, always equally spaced but with different distances, were considered and assessed. The distances were chosen in a range between 1 cm and 20 cm.

The goal was to find the "optimum" size that allows to find a good compromise between a highly accurate reconstruction of the location of the EM source and a small probe dimension.

In this context, four different new networks in which the ANN 4-8-2 is trained using four different sets of 133 new examples and tested with four different sets of 900 new totally random test examples have been assessed. Figure 8.5 shows the errors on the distance d and on the angle ϑ reconstructed by varying the probe's dimensions: the variations of the maximum, minimum, and average relative errors on the distances are shown in Figure 8.5(a), whereas the variations of the maximum, minimum, and average absolute errors on the angles are shown in Figure 8.5(b).

The results show that for small probe dimensions, the errors are high, but, as expected, they decrease as the probe size increases. It is worth noting that the errors both on distance and on angle are very high (greater than 100% for the distance and greater than 50 degree(s) for the angle) when the receiving antennas are spaced less than 10 cm apart. At 10 cm the average percentage error on the distance is 6.1% and the average absolute error on the angle is 0.6 degree(s). After that, the errors tend to slowly decrease, reaching, at 20 cm, the average percentage error on the distance of 4.1% and the average absolute error on the angle of 0.33 degree(s).

This suggests that using a probe with the receiving antennas equally spaced 10 cm apart could be an acceptable compromise. For such a case, the numerical values of the maximum, average, and minimum errors on the distance and on the angle are the same as the ones reported in Table 8.1.

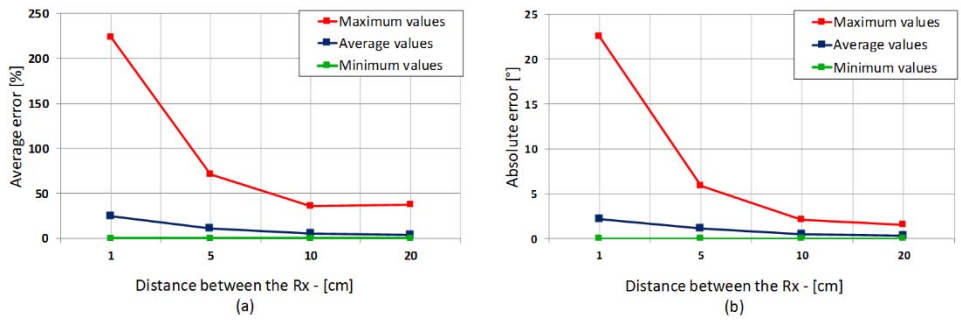

Figure 8.5. Errors by varying the dimensions of the probe. (a) Maximum, average, and minimum relative errors on the reconstruction of the distance d. (b) Maximum, average, and minimum absolute errors on the reconstruction of the angle ϑ.

Finally, the optimum dimension of the probe when moved 3 m from the wall has been assessed. To this end, the same four sizes of the previous case (1, 5, 10, and 20 cm) were considered. Four different new networks, in which the ANN 4-8-2 is trained, respectively, with four different sets of 133 new examples and tested with four different sets of 900 totally random new test examples, have been assessed. Figure 8.6 shows the errors on the distance d and on the angle ϑ reconstructed by varying the probe's dimensions and moving it 3 m from the wall.

The results show once again that the probe with the receiving antennas equally spaced 10 cm apart could be an acceptable compromise, giving an average percentage error on the distance of 9.79% and an average absolute error on the angle of 0.43 degree(s). Table 8.2 shows the numerical values of the maximum, minimum, and average errors on the distance and on the angle for the case of the probe that is moved 3 meters from the wall and formed by three receivers equally spaced 10 cm apart.

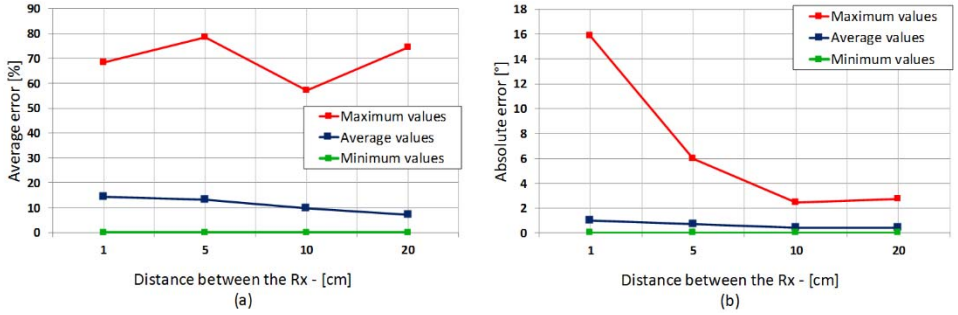

Figure 8.6. Errors by varying the dimensions of the training set. (a) Maximum, average, and minimum relative errors on the reconstruction of the distance d. (b) Maximum, average, and minimum absolute errors on the reconstruction of the angle ϑ.

Table 8.2. Maximum, average, and minimum errors on the distance and on the angle for the case of the probe that is moved 3 meters from the wall with the receivers equally spaced 10 cm apart. The errors are evaluated by using a set of 900 different test data.

ANN trained with 133 examples	**Error values**		
	Maximum	***Average***	***Minimum***
Relative error on the distance (%)	57.15	9.79	0.001
Absolute error on the angle (°)	2.45	0.43	0.0003

8.4. Conclusions

In this appendix, the problem of localizing an UWB pulsed EM source has been considered, and in particular a new probing technique, based on the use of ANNs, was proposed and assessed in order to localize an UWB pulsed EM source that is positioned behind a wall. The intent was to satisfy two main objectives: accurate reconstruction of the EM source position as high as possible and using a probe with dimensions that are as small as possible.

The source can be arbitrarily located in a square domain of 3×3 m^2 and it radiates, at regular time intervals, UWB pulses of central band frequency 300 MHz and time duration 5 ns. The probe, made up of three linearly placed and equally spaced receiving antennas (R_1, R_2, R_3), moves parallel to the other side of the wall, and it measures the differences on the times of arrival and on the amplitudes of the pulses measured by each receiver. Suitable data—namely the differences on the times of arrival ($\Delta t_{i+1,i}$) and on the amplitude ratios (A_i/A_{i+1}) of the first peak of each received pulse—were used to train and test an ANN able to provide the direction ϑ and the distance d of the EM source relative to the position of the probe.

An ANN was built that receives four data inputs: the two differences in the arrival times $\Delta t_{2,1}$, $\Delta t_{3,2}$ and the two ratios of amplitude (A_1/A_2), (A_2/A_3); and it provides two outputs: the distance d and the angle ϑ referring to the probe position.

First, the best training-set dimension has been studied by using a probe formed by three receiving antennas equally spaced 10 cm apart. It has been found that the optimal training set comprises 133 examples. Indeed, when the ANN is trained with 133 training data inputs, it is possible to find the source position with an average percentage error on the distance d equal to 6.1% and the average absolute error on the angle ϑ of 0.6 degree(s). The errors have been evaluated on a set of 900 totally random test examples.

Second, the optimum dimension of the probe has been assessed, by changing the distance among the equally spaced receiving antenna form 1 cm up to 20 cm. The obtained results confirmed that the use of a probe with the receiving antennas spaced 10 cm apart is a good compromise to achieve the two goals—namely, highly accurate source positioning and the use of a probe with the smallest dimensions.

Finally, the optimum dimension of the probe when moved 3 m from the wall has been studied. Also in this case, it was found that the probe with the receiving antennas equally spaced 10 cm apart could be an acceptable compromise, giving an

average percentage error on the distance of 9.79% and an average absolute error on the angle of 0.43 degree(s).

These encouraging results suggest to move on further studies. First of all by assessing the robustness of this probing technique against for example different types of wall, through their dielectric characteristics and thickness. Second, it will be important to assess the approach considering different distances of the probe from the wall, as well as its different orientations. The final optimum goal would be to try to detect and localize the EM source position by moving the probe along a totally random path and not only parallel to the wall.

References

1. American Cancer Society, *Cancer Facts & Figures 2015*, Atlanta, GA, USA, American Cancer Society, 2015.
2. L. Tabár, and P. B. Dean, "A new era in the diagnosis and treatment of breast cancer," *The Breast Journal*, vol. 16, S2–S4, 2010.
3. P. T. Huynh, A. M. Jarolimek, and S. Daye, "The false-negative mammogram," *RadioGraphics*, vol. 18, no. 5, pp. 1137–1154, 1998.
4. W. A. Berg, L. Gutierrez, M. S. NessAiver, W. B. Carter, M. Bhargavan, R. S. Lewis, and O. B. Ioffe, "Diagnostic accuracy of mammography, clinical examination, U.S., and MR imaging in preoperative assessment of breast cancer," *Radiology*, vol. 233, no. 3, pp. 830–849, 2004.
5. A. M. Hassan and M. El-Shenawee, "Review of electromagnetic techniques for breast cancer detection," *IEEE Reviews in Biomedical Engineering*, vol. 4, pp. 103–118, 2011.
6. E. Zastrow, S. K. Davis, M. Lazebnik, F. Kelcz, B. D. Van Veem, and S. C. Hagness, "Database of 3D Grid-Based Numerical Breast Phantoms for use in Computational Electromagnetics Simulations," Department of Electrical and Computer Engineering University of Wisconsin-Madison, http://uwcem.ece.wisc.edu/MRIdatabase/ InstructionManual.pdf.
7. T. Yin, F. H. Ali, and C. C. Reyes-Aldasoro, "A robust and artifact resistant algorithm of ultrawideband imaging system for breast cancer detection," *IEEE Transactions on Biomedical Engineering*, vol. 62, no. 6, pp. 1514–1525, 2015.
8. W. Zhi and F. Chin, "Entropy-based time window for artifact removal in UWB imaging of breast cancer detection," *IEEE Signal Processing Letters*, vol. 13, no. 10, pp. 585–588, 2006.
9. A. Maskooki, E. Gunawan, S. B. Soh, and K. S. Low, "Frequency domain skin artifact removal method for ultra-wideband breast cancer detection," *Progress In Electromagnetics Research*, vol. 98, pp. 299–314, 2009.

10. B. Maklad and E. C. Fear, "Reduction of skin reflections in radar-based microwave breast imaging," in proceedings of the *30th Annual International Conference of the IEEE Engineering in Medicine and Biology Society*, pp. 21–24, Vancouver, BC, 2008.
11. P. A. van Dam, M. L. Van Goethem, E. Kersschot, J. Vervliet, I. B. Van den Veyver, A. De Schepper, and P. Buytaert, "Palpable solid breast masses: retrospective single-and multimodality evaluation of 201 lesions," *Radiology*, vol. 166, no. 2, pp. 435–439, 1988.
12. American Cancer Society, *Cancer Facts & Figures 2011*, Atlanta, GA, USA, American Cancer Society, 2011.
13. R. C. Conceicao, M. O'Halloran, M. Glavin, and E. Jones, "Numerical modelling for ultra wideband radar breast cancer detection and classification," *Progress In Electromagnetics Research*, B, vol. 34, pp. 145–171, 2011.
14. J. M. Dixon, *ABC of Breast Diseases*, 3rd edition, Blackwell Publishing Ltd., 2006.
15. L. J. Layfield, K. H. Anders, B. J. Glasgow, and J. M. Mirra, "Fine-needle aspiration of primary soft-tissue lesions," *Archives of pathology & laboratory medicine*, vol. 110, no. 5, pp. 420–424, 1986.
16. F. A. Mettler Jr, W. Huda, T. T. Yoshizumi, and M. Mahesh, "Effective doses in radiology and diagnostic nuclear medicine: a catalog 1," *Radiology*, vol. 248, no. 1, pp. 254–263, 2008.
17. R. W. Brown, Y. C. N. Cheng, E. M. Haacke, M. R. Thompson, and R. Venkatesan, *Magnetic resonance imaging: physical principles and sequence design*, John Wiley & Sons, 2014.
18. J. T. Bushberg, and J. M. Boone, *The essential physics of medical imaging*, Lippincott Williams & Wilkins, 2011.
19. I. Khalkhali, I. Mena, and L. Diggles, "Review of imaging techniques for the diagnosis of breast cancer: a new role of prone scintimammography using technetium-99m sestamibi," *European journal of nuclear medicine*, vol. 21, no. 4, pp. 357–362, 1994.
20. A. Berrington de González, and S. Darby, "Risk of cancer from diagnostic X-rays: Estimates for the U.K. and 14 other countries," *The Lancet*, vol. 363, no. 9406, pp. 345–351, 2004.
21. L. L. Humphrey, and D. J. Ballard, "Early detection of breast cancer in women," *Primary care*, vol. 16, no. 1, pp. 115–132, 1989.
22. W. C. Amalu, "Nondestructive testing of the human breast: the validity of dynamic stress testing in medical infrared breast imaging," in proceedings of the *26th Annual International Conference of the IEEE Engineering in Medicine and Biology Society* (IEMBS), pp. 1174–1177, 2004.

23. D. Ikeda, D. Baker, and B. Daniel, "Magnetic resonance imaging of breast cancer: Clinical indications and breast MRI reporting system," *Journal of Magnetic Resonance Imaging*, vol. 12, no. 6, pp. 975–983, 2000.
24. S. Orel, and M. Schnall, "MR imaging of the breast for the detection, diagnosis, and staging of breast cancer," *Radiology*, vol. 220, no. 1, pp. 13–30, 2001.
25. J. Croll, J. Kotevich, and M. Tabrett, "The diagnosis of benign disease and the exclusion of malignancy in patients with breast symptoms," *Seminars in Ultrasound*, vol. 3, pp. 38–50, 1982.
26. J. Jellins, T. S. Reeve, J. Croll, and G. Kossoff, "Results of breast echography examination in Sydney," *Australia*, pp. 58–62, 1979.
27. R. L. Egan, and K. L. Egan, "Detection of breast carcinoma: comparison of automated water-path whole-breast sonography, mammography, and physical examination," *American journal of roentgenology*, vol. 143, no. 3, pp. 493–497, 1984.
28. G. M. Giuseppetti, G. Rizzatto, G. Gozzi, and P. Ercolani, "Ruolo dell'ectomografia nella diagnosi del carcinoma infraclinico della mammella," *Radiol Med*, vol. 78, pp. 339–342, 1989.
29. J. A. Smallwood, P. Guyer, K. Dewbury, K., Mengatti, S. A. N. D. R. A., A. Herbert, G. T. Royle, and I. Taylor, "The accuracy of ultrasound in the diagnosis of breast disease," *Annals of the Royal College of Surgeons of England*, vol. 68, no. 1, pp. 19–22, 1986.
30. V. P. Jackson, "The role of US in breast imaging," *Radiology*, vol. 177, no. 2, pp. 305–311, 1990.
31. S. C. Hagness, A. Taflove, and J. E. Bridges, "Two-dimensional FDTD analysis of a pulsed microwave confocal system for breast cancer detection: Fixed-focus and antenna-array sensors," *IEEE Transactions on Biomedical Engineering*, vol. 45, no. 12, pp. 1470–1479, 1998.
32. M. Lazebnik, M. Okoniewski, J. H. Booske, and S. C. Hagness, "Highly accurate Debye models for normal and malignant breast tissue dielectric properties at microwave frequencies," *IEEE Microwave and Wireless Components Letters*, vol. 17, no. 12, pp. 822–824, 2007.
33. M. Lazebnik, D. Popovic, L. McCartney, et al., "A large-scale study of the ultrawideband microwave dielectric properties of normal, benign, and malignant breast tissues obtained from cancer surgeries," *Physics in Medicine and Biology*, vol. 52, no. 20, pp. 6093–9115, 2007.
34. T. M. Grzegorczyk, P. M. Meaney, P. A. Kaufman, and K. D. Paulsen, Fast 3-D tomographic microwave imaging for breast cancer detection, *IEEE Transactions on Medical Imaging*, vol. 31, no. 8, pp. 1584–1592, 2012.

35. B. Bocquet, J. C. Van de Velde, A. Mamouni, Y. Leroy, G. Giaux, J. Delannoy, and D. Delvalee, "Microwave radiometric imaging at 3 GHz for the exploration of breast tumors," *IEEE Transactions on Microwave Theory and Techniques*, vol. 38, no. 6, pp. 791–793, 1990
36. F. Bardati and S. Iudicello, "Modeling the visibility of breast malignancy by a microwave radiometer," *IEEE Transactions on Biomedical Engineering*, vol. 55, no. 1, pp. 214–221, 2008.
37. J. D. Shea, B. D. Van Veen, and S. C. Hagness, "A TSVD analysis of microwave inverse scattering for breast imaging," *IEEE Transactions on Biomedical Engineering*, vol. 59, no. 4, pp. 936–945, 2011.
38. Q. Fang, P. M. Meaney, and K. D. Paulsen, "Viable three-dimensional medical microwave tomography: Theory and numerical experiments," *IEEE Transactions on Antennas and Propagation*, vol. 58, no. 2, pp. 449–458, 2010.
39. M. Klemm, I. J. Craddock, J. A. Leendertz, A. Preece and R. Benjamin, "Radar-based breast cancer detection using a hemispherical antenna array—experimental results," *IEEE Transactions on Antennas and Propagation*, vol. 57, no. 6, pp. 1692–1704, 2009.
40. M. Klemm, J. A. Leendertz, D. Gibbins, I. J. Craddock, A. Preece, and R. Benjamin, "Microwave radar-based differential breast cancer imaging: Imaging in homogeneous breast phantoms and low contrast scenarios," *IEEE Transactions on Antennas and Propagation*, vol. 58, no. 7, pp. 2337–2344, 2010.
41. E. C. Fear, J. Bourqui, C. Curtis, D. Mew, B. Docktor, and C. Romano, "Microwave breast imaging with a monostatic radar-based system: A study of application to patients," *IEEE Transactions on Microwave Theory and Techniques*, vol. 61, no. 5, pp. 2119–2128, 2013.
42. E. C. Fear, X. Li, S. C. Hagness and M. A. Stuchly, "Confocal microwave imaging for breast cancer detection: Localization of tumors in three dimensions," *IEEE Transactions on Biomedical Engineering*, vol. 49, no. 8, pp. 812–822, 2002.
43. A. Sabouni, D. Flores-Tapia, S. Noghanian, G. Thomas, and S. Pistorius, "Hybrid microwave tomography technique for breast cancer imaging," in proceedings of the *28th Annual International Conference in Engineering in Medicine and Biology Society* (EMBS), IEEE, pp. 4273–4276, 2006.
44. L. V. Wang, X. Zhao, H. Sun, and G. Ku, "Microwave induced acoustic imaging of biological tissues," *Review of Scientific Instruments*, vol. 70, no. 9, pp. 3744–3748, 1999.

45. K. L. Carr, "Microwave radiometry: Its importance to the detection of cancer," *IEEE Transactions on Microwave Theory and Techniques*, vol. 37, no. 12, pp. 1862–1869, 1989.
46. V. Zhurbenko, and T. Rubæk, *Microwave Breast Imaging Techniques*, EUSAR, 2010.
47. R. Tipa, and O. Baltag, "Microwave Thermography for Cancer Detection," *Romanian Journal of Physics*, vol. 51, nos. 3–4, pp. 371–377, 2006.
48. S. Jacobsen, Ø. Klemetsen, "Improved detect ability in medical microwave radio-thermometers as obtained by active antennas," *IEEE Transactions on Biomedical Engineering*, vol. 55, no. 12, pp. 2778–2785, 2008.
49. B. Stec, A. Dobrowolski, and W. Susek, "Estimation of deep-seated profile of temperature distribution inside biological tissues by means of multifrequency microwave thermograph," in proceedings of the *International Microwave Symposium Digest MTT-S*, vol. 3, pp. 2261–2264, 2002.
50. K. L. Carr, P. Cevasco, P. Dunlea, and J. Shaeffer, "Radiometric sensing: an adjuvant to mammography to determine breast biopsy," in proceedings of the *International Microwave Symposium Digest MTT-S*, vol. 2, pp. 929–932, 2000.
51. J. W. Lee, S. M. Lee, K. S. Kim, W. T. Han, G. Yoon, L. A. Pasmanik, ... and A. V. Troitsky, "Experimental investigation of the mammary gland tumour phantom for multifrequency microwave radio-thermometers," *Medical and Biological Engineering and Computing*, vol. 42, no. 5, pp. 581–590, 2004.
52. S. Iudicello, *Microwave radiometry for breast cancer detection*, Ph.D. Thesis, Università degli studi di Roma "Tor Vergata", 2009.
53. Y. Xie, B. Guo, L. Xu, J. Li, and P. Stoica, "Multi-static adaptive microwave imaging for early breast cancer detection," *IEEE Transactions on Biomedical Engineering*, vol. 53, no. 8, pp. 1647–1657, 2006.
54. T. Henriksson, M. Klemm, D. Gibbins, J. Leendertz, T. Horseman, A. W. Preece, ... and I. J. Craddock, "Clinical trials of a multistatic UWB radar for breast imaging," in proceedings of the *Antennas and Propagation Conference* (LAPC), IEEE, pp. 1–4, 2011.
55. D. Byrne, M. O'Halloran, M. Glavin, and E. Jones, "Data independent radar beamforming algorithms for breast cancer detection," *Progress In Electromagnetics Research*, vol. 107, pp. 331–348, 2010.
56. Y. Xie, B. Guo, L. Xu, J. Li, and P. Stoica, "Multistatic adaptive microwave imaging for early breast cancer detection," *IEEE Transactions on Biomedical Engineering*, vol. 53, no. 8, pp. 1647–1657, 2006.

57. Y. Chen, I. J. Craddock, P. Kosmas, M. Ghavami, and P. Rapajic, "Multiple-input multiple-output radar for lesion classification in ultrawideband breast imaging," *IEEE Journal of Selected Topics in Signal Processing*, vol. 4, no. 1, pp. 187–201, 2010.
58. E. A. Marengo, F. K. Gruber, and F. Simonetti, "Time-reversal MUSIC imaging of extended targets," *IEEE Transactions on Image Processing*, vol. 16, no. 8, pp. 1967–1984, 2007.
59. M. D. Hossain, A. S. Mohan, and M. J. Abedin, "Beamspace time-reversal microwave imaging for breast cancer detection," *IEEE Antennas and Wireless Propagation Letters*, vol. 12, pp. 241–244, 2013
60. M. Klemm, I. J. Craddock, J. A. Leendertz, A. Preece, and R. Benjamin, "Improved delay-and-sum beamforming algorithm for breast cancer detection," *International Journal of Antennas and Propagation*, 2008.
61. H. B. Lim, N. T. T. Nhung, E. P. Li, N. D. Thang, "Confocal microwave imaging for breast cancer detection: Delay-multiply and sum image reconstruction algorithm," *IEEE Transactions on Biomedical Engineering*, vol. 55, no. 6, pp. 1697–1704, 2008.
62. R. Nilavalan, A. Gbedemah, I. J. Craddock, X. Li, and S. C. Hagness, "Numerical investigation of breast tumour detection using multi-static radar," *IET Electronic Letters*, vol. 39, pp. 1787–1789, 2003.
63. N. A. Simonov, S. I. Jeon, S. H. Son, J. M. Lee, and H. J. Kim, "3D Microwave Breast Imaging Based on Multistatic Radar Concept System," *Journal of electromagnetic engineering and science*, vol. 12, no. 1, pp. 107–114, 2012.
64. P. M. Meaney, M. W. Fanning, D. Li, S. P. Poplack, and K. D. Paulsen, "A clinical prototype for active microwave imaging of the breast," *IEEE Transactions on Microwave Theory and Techniques*, vol. 48, no. 11, pp. 1841–1853, 2000.
65. S. P. Poplack, K. D. Paulsen, A. Hartov, P. M. Meaney, B. W. Pogue, B. W., T. D. Tosteson, ... and W. A. Wells, "Electromagnetic breast imaging: Average tissue property values in women with negative clinical findings," *Radiology*, vol. 231, no. 2, pp. 571–580, 2004.
66. S. P. Poplack, T. D. Tosteson, W. A. Wells, B. W. Pogue, P. M. Meaney, A. Hartov, ... and K. D. Paulsen, "Electromagnetic breast imaging: Pilot results in women with abnormal mammography," Radiology, vol. 243, no. 2, pp. 350–359, 2007.
67. S. Y. Semenov, A. E. Bulyshev, A. Abubakar, V. G. Posukh, Y. E. Sizov, A. E. Souvorov, P. Van den Berg, and T. Williams, "Microwave tomographic imaging of the high dielectric-contrast objects using different

image reconstruction approaches," *IEEE Transactions on Microwave Theory and Techniques*, vol. 53, no. 7, pp. 2284–2294, 2005.

68. S. Semenov, J. Kellam, Y. Sizov, A. Nazarov, Th. Williams, B. Nair, A. Pavlovsky, V. Posukh, and M. Quinn, "Microwave tomography of extremities: 1. Dedicated 2D system and physiological signatures," *Physics in medicine and biology*, vol. 56, no. 7, pp. 2005–2017, 2011.
69. S. Semenov, J. Kellam, Y. Sizov, A. Nazarov, Th. Williams, B. Nair, A. Pavlovsky, V. Posukh, and M. Quinn, "Microwave tomography of extremities: 2. Functional fused imaging of flow reduction and simulated compartment syndrome," *Physics in medicine and biology*, vol. 56, no. 7, pp. 2019–2030, 2011.
70. C. Gilmore, P. Mojabi, A. Zakaria, M. Ostadrahimi, C. Kaye, S. Noghanian, L. Shafai, S. Pistorius, and J. LoVetri, "A wideband microwave tomography system with a novel frequency selection procedure," *IEEE Transactions on Biomedical Engineering*, vol. 57, no. 4, pp. 894–904, 2010.
71. M. Ostadrahimi, P. Mojabi, S. Noghanian, L. Shafai, S. Pistorius, and Joe LoVetri, "A novel microwave tomography system based on the scattering probe technique," *IEEE Transactions on instrumentation and measurement*, vol. 61, no. 2, pp. 894–904, 2012.
72. A. Fhager, M. Gustaffson, and S. Nordebo, "Image reconstruction in microwave tomography using a dielectric debye model," *IEEE Transactions on Biomedical Engineering*, vol. 59, no. 1, pp. 156–166, 2012.
73. T. Rubæk, and J. J. Mohr, "Microwave Tomography," in *An Introduction to Microwave Imaging for Breast Cancer Detection*, pp. 17–45, Springer International Publishing, 2016.
74. M. Born, Principles of optics: electromagnetic theory of propagation, interference and diffraction of light, 7th ed. Cambridge University Press, Cambridge, New York, 1999.
75. J. B. Keller, "Accuracy and Validity of the Born and Rytov Approximations," *JOSA*, vol. 59, no. 8, pp. 1003–1004, 1969.
76. M. Slaney, A. C. Kak, and L. E. Larsen, "Limitations of imaging with first-order diffraction tomography," *IEEE Transactions on Microwave Theory and Techniques*, vol. 32, no. 8, pp. 860–874, 1984.
77. R. S. Dembo, S. C. Eisenstat, and T. Steihaug, "Inexact newton methods," *SIAM Journal on Numerical analysis*, vol. 19, no. 2, pp. 400–408, 1982.
78. S. C. Eisenstat, and H. F. Walker, "Globally convergent inexact Newton methods," *SIAM Journal on Optimization*, vol. 4, no. 2, pp. 393–422, 1994.
79. S. C. Eisenstat, and H. F. Walker, "Choosing the forcing terms in an inexact Newton method," *SIAM Journal on Scientific Computing*, vol. 17, no. 1, pp. 16–32, 1996.

80. M. R. Hestenes, and E. Stiefel, "Methods of conjugate gradients for solving linear systems," *Journal of Research National Bureau of Standards*, vol. 49, pp. 409–436, 1952.
81. L. Landweber, "An Iteration Formula for Fredholm Integral Equations of the First Kind," *American Journal of Mathematics*, vol. 73, no. 3, pp. 615–624, 1951.
82. F. Gao, B. D. Van Veen, and S. C. Hagness, "Sensitivity of the distorted born iterative method to the initial guess in microwave breast imaging," *IEEE Transactions on Antennas and Propagation*, vol. 63, no. 8, pp. 3540–3547, 2015.
83. J. H. Holland, "Genetic Algorithms and Adaptation," in O. G. Selfridge, E. L. Rissland, M. A. Arbib (eds.), *Adaptive Control of III-Defined Systems*, Springer US, Boston, pp 317–333, 1984.
84. J. D. Schaffer, "Some experiments in machine learning using vector evaluated genetic algorithms," Ph.D. Thesis, Vanderbilt University, Nashville, TN (USA), 1985.
85. M. Donelli, A. Massa, G. Oliveri, M. Pastorino, and A. Randazzo, "A differential evolution-based iterative multi-scaling algorithm for microwave imaging of dielectric structures," in proceedings of the *IEEE International Conference on Imaging Systems and Techniques*, pp. 90–95, 2010.
86. M. Brignone, G. Bozza, A. Randazzo, M. Piana, and M. Pastorino, "A Hybrid Approach to 3d Microwave Imaging by Using Linear Sampling and ACO," *IEEE Transactions on Antennas and Propagation*, vol. 56, no. 10, pp. 3224–3232, 2008.
87. J. Kennedy, "Particle swarm optimization," in *Encyclopedia of machine learning*, pp. 760–766, Springer, US, 2011.
88. S. Caorsi, G. L. Gragnani, S. Medicina, M. Pastorino, and G. Zunino, "Microwave imaging method using a simulated annealing approach," *IEEE microwave and guided wave letters*, vol. 1, no. 11, pp. 331–333, 1991.
89. L. Garnero, A. Franchois, J. P. Hugonin, C. Pichot, and N. Joachimowicz, "Microwave imaging-complex permittivity reconstruction-by simulated annealing," *IEEE Transactions on microwave theory and techniques*, vol. 39, no. 11, pp. 1801–1807, 1991.
90. A. Sabouni, S. Noghanian, and S. Pistorius, "A global optimization technique for microwave imaging of the inhomogeneous and dispersive breast," *Canadian Journal of Electrical and Computer Engineering*, vol. 35, no. 1, pp. 15–24, 2010.
91. V. Tereshko, and A. Loengarov, "Collective decision-making in honey bee foraging dynamics," *Computing and Information Systems Journal*, vol. 9, no. 3, 2005.

92. M. Donelli, I. Craddock, D. Gibbins, and M. Sarafianou, "A three-dimensional time domain mocrowave imaging method for breast cancer detection based on an evolutionary algorithm," *Progress In Electromagnetics Research*, M, vol. 18, pp. 179–195, 2011.
93. A. Giannopoulos, "Modelling ground penetrating radar by GprMax," *Construction and Building Materials*, vol. 19, no. 10, pp. 755–762, 2005
94. X. Li and S. C. Hagness, "A confocal microwave imaging algorithm for breast cancer detection," *IEEE Microwave and Wireless Components letters*, vol. 11, no. 3, pp. 130–132, 2001
95. D. Uduwawala, "Gaussian vs differentiated gaussian as the input pulse for ground penetrating radar applications," in proceedings of the *International Conference on Industrial and Information Systems* (ICIIS), pp. 199–202, Penadeniya, Sri Lanka, 2007.
96. S. Haykin, *Neural Networks: A Comprehensive Foundation*, New York, NY: Prentice Hall, 1999.
97. M. McCord Nelson, and W. T. Illingworth, *A Practical Guide to Neural Nets*, Boston, MA: Addison-Wesley, 1991.
98. P. S. Churchland, and T. J. Sejnowski, *The Computational Brain*, Cambridge, UK: MIT Press, 1992.
99. S. Caorsi, and P. Gamba, "Electromagnetic detection of dielectric cylinders by a neural network approach," *IEEE Transactions on Geoscience and Remote Sensing*, vol. 37, no. 2, pp. 820–827, 1999.
100. E. J. Bond, X. Li, S. C. Hagness, and B. D. Van Veen, "Microwave imaging via space-time beamforming for early detection of breast cancer," *IEEE Transactions on Antennas and Propagation*, vol. 51, no. 8, pp. 1690–1705, 2003.
101. J. M. Sill, and E. C. Fear, "Tissue sensing adaptive radar for breast cancer detection-experimental investigation of simple tumor models," *IEEE Transactions on Microwave Theory and Techniques*, vol. 53, no. 11, pp. 3312–3319, 2005.
102. P. K. Verma, A. N. Gaikwad, D. Singh, and M. J. Nigam, "Analysis of clutter reduction techniques for through wall imaging in UWB range," *Progress In Electromagnetics Research*, B, vol. 17, pp. 29–48, 2009.
103. M. A. Elahi, M. Glavin, E. Jones, and M. O'Halloran, "Artifact removal algorithms for microwave imaging of the breast," *Progress In Electromagnetics Research*, vol. 141, pp. 185–200, 2013.
104. Y. Alvarez, F. Las-Heras, and M. R. Pino, "Full-wave method for RF sources location," in proceedings of the *Second European Conference on Antennas and Propagation* (EuCAP), Edinburgh, UK: IET, 2007.

105. N. Patwari, and J. Wilson, "RF sensor networks for device-free localization: measurements, models, and algorithms," in proceedings of the IEEE, vol. 98, no. 11, pp. 1961–1973, 2010.
106. A. Ko, and H. Y. K. Lau, "Robot assisted emergency search and rescue system with a wireless sensor network," *International Journal of Advanced Science and Technology*, vol. 3, pp. 69–78, 2009.
107. C. H. Peck, and P. J. Moore, "A direction-finding technique for wide-band impulsive noise source," *IEEE Transactions on Electromagnetic Compatibility*, vol. 43, no. (2), pp. 149–154, 2001.
108. I. E. Portugues, P. J. Moore, I. A. Glover, C. Johnstone, R. H. McKosky, M. B. Goff, and L. van der Zel, "RF-based partial discharge early warning system for air-insulated substations," *IEEE Transactions on Power Delivery*, vol. 24, no. 1, pp. 20–29, 2009.
109. A. Tungkanawanich, Z. I. Kawasaki, J. Abe, and K. Matsuura, "Location of partial discharge source on distribution line by measuring emitted pulse-train electromagnetic waves," in proceedings of the *Power Engineering Society Winter Meeting*, Singapore, SG: IEEE, 2000.
110. A. Hirata, T. Morimoto, and Z. I. Kawasaki, "3-D localization of ultrawideband impulsive noise sources," in proceeding of the *International Symposium on Electromagnetic Compatibility* (EMC), Istanbul, TR: IEEE, 2003.
111. Y. Tian, A. Tatematsu, K. Tanabe, and K. Miyajima, "Development of locating system of pulsed electromagnetic interference source based on advanced TDOA estimation method," *IEEE Transactions on Electromagnetic Compatibility*, vol. 56, no. 6, pp. 1326–1334, 2014.
112. S. Caorsi, and M. Stasolla, "Characterization of lossy layers through monostatic radar measurements," in proceedings of the *13th International Conference Mediterranean Microwave Symposium* (MMS). Saida, LBN: IEEE, 2013.